Anton Hörl

DOCTORAL THESIS

For obtaining the academic degree of
Doktor der Naturwissenschaften

Tomography of Particle Plasmon Fields using Electron Energy Loss Spectroscopy

Supervisor: Ao.Univ.-Prof. Mag. Dr. Ulrich Hohenester

Institute of Physics
Department of Theoretical Physics

Graz, March 2016

Abstract

Surface plasmons - coherent electron oscillations at the surface of metallic nanoparticles - allow to bridge between micrometer and nanometer length scales of optics and nanodevices, and are subject to various applications and experiments, the most prominent being sensors.

This thesis is devoted to image the near-fields accompanied with coherent electron oscillations with nanometer resolution. In more detail, we investigate the interaction of a swift electron with surface plasmons, as it occurs in electron energy loss spectroscopy (EELS), and examine the electron energy loss probability of plasmonic nanostructures. Further, we develop a tomography scheme for EEL maps in the quasi-static approximation and extend it by regularization with compressed sensing to the full vectorial case.

We find that the interaction of swift electrons and surface plasmons leads to nanometer spatial resolution of the electron energy loss probability of surface plasmons, and gives detailed insight into the near-field of plasmonic structures. Further, the juxtaposition between experiment and theory is improved by utilizing the full three dimensional particle geometry in the simulations. By introducing a modal decomposition of the Green function, we reformulate EELS as a tomography scheme and thereby connect it with local optical properties - the photonic local density of states - of plasmonic nanostructures. For particles small compared to the resonance wavelength these can be found under some restrictions by an inverse Radon transformation. The more general full vectorial case is treated by using additional knowledge of the particle geometry and compressed sensing.

Zusammenfassung

Oberflächenplasmonen - kohärente Elektronenoszillationen an metallischen Oberflächen - erlauben es, die Mikrometer- und Nanometer-Längenskalen von Optik und Nanobausteinen zu verbinden. Sie werden für verschiedene Applikationen und Experimente, wie zum Beispiel Sensoren, benutzt.

Im Rahmen dieser Dissertation werden die mit den Oberflächenplasmonen einhergehenden Nahfelder untersucht und dargestellt. Im Detail betrachten wir die Wechselwirkung eines schnellen Elektrons mit Oberflächenplasmonen, wie es in der Elektronenverlustspektroskopie (EELS) passiert, und berechnen die Energieverlustwahrscheinlichkeit des Elektrons für verschiedene metallische Nanostrukturen. Weiters entwickeln wir ein Tomographie Schema für EEL Projektionen in der quasi-statischen Näherung sowie für den vektoriellen Fall mit Retardierungseffekten.

Die Resultate für verschiedene metallische Nanostrukturen zeigen, dass Nanometerauflösung von plasmonischen Strukturen mit EELS zu tieferer Erkenntnis des Nahfeldes führt und durch die Benutzung der vollen dreidimensionalen Oberflächenstruktur der Vergleich von Experiment und Simulation profitiert. Wenn man EELS als Tomographieproblem formuliert, ist es zusätzlich möglich, Informationen über die optischen Eigenschaften von metallischen Nanostrukturen - genauer die lokale optische Zustandsdichte - zu finden. Für Teilchen die klein gegenüber der Resonanzwellenlänge sind, ist dies unter bestimmten Einschränkungen mit einer inversen Radon Transformation möglich. Für eine generelle Rekonstruktion der optischen Eigenschaften benötigt man die zusätzliche Information der Oberflächenstruktur.

Contents

1 Introduction

1.1 Scope and structure of this work

Investigations of the interaction between electromagnetic waves and metallic nanoparticles has led to a fast growing research field called plasmonics, which is the topic of this thesis. Hybrid light-matter excitations, termed surface plasmons, allow to bridge between the length scale of visible light and the nanometer-regime. This is achieved by binding light to coherent electron oscillations at the surface of metallic nanoparticles. Surface plasmons are accompanied by large field enhancements and evanescent fields nearby the particle surface [1]. The progress of the field aroused by a good deal from developments in the fabrication process of nano sized objects, such as chemical synthesis or electron beam lithography, which allow to prepare metallic nanoparticles of various size and geometry with nanometer accuracy, which in turn permits tailoring the resonance frequencies of surface plasmons [2] and leads to high field enhancements at certain hot-spots [3]. This thesis is devoted to the theoretical and experimental investigations of the near-fields with nanometer spatial and sub eV spectral resolution.

In more detail, we study the interaction of swift electrons with metallic nanoparticles. The excitation of surface plasmons by a relativistically moving electron and the energy loss of the electron produced by the induced plasmonic field is theoretically well established, but for complex plasmonic nanoparticle shapes numerical simulation tools are needed in order to strengthen and interpret experimental findings. One goal of this thesis is to use and improve simulation tools, which compute the energy loss of fast electrons by plasmonic nanoparticles.

Electron energy loss spectroscopy projects the induced plasmon fields along the electron trajectory for certain impact parameters, and there is some controversy about the interpretation of the measurement signal. Here we challenge the interpretation problem and reformulate EELS as a tomography problem. We first employ the idea and formulate the tomography problem with a number of assumptions and restrictions, especially the small particle approximation. In a second step we lift some of these restrictions and generalize the idea to particle dimensions in the order of the resonance wavelength.

The thesis is structured as follows: The first chapter provides a general introduction into the field of this thesis - plasmonics, and derives some basic properties of surface plasmons. The second one deals with imaging of surface plasmons and gives a detailed introduction into the theory of electron energy loss spectroscopy, one of the main techniques used for surface plasmon imaging. In the third chapter we provide a general introduction into the field of computed tomography and give detailed insight into the techniques used for tomography of surface plasmons with electron energy loss spectroscopy. Chapter four to eight are reprints of papers originated from this thesis in

chronological order of appearance. Finally in chapter nine we conclude the thesis by giving an overview of the obtained results.

1.2 The world of plasmonics

Surface plasmons (or surface plasmon polaritons) are surface charge oscillations on the surface of metallic nanoparticles which are excited by electromagnetic fields (e.g. light, oscillating dipole, fast electron beam). Surface plasmons come along with strongly localized evanescent fields confined on a nanometer scale and evolve at certain resonance energies, which depend on geometry and material of the nanoparticles. The field associated with surface plasmons is decaying exponentially away from the particle surface and is enhanced at certain geometry dependent hot spots, like particle corners or edges. Because of the robustness of the effect - surface plasmons can be studied under air and quite dirty conditions - plasmonics holds promise for numerous applications in different fields.

Probably the first observation of surface plasmons appearing in literature dates back to 1902 and is nowadays termed as Woods anomalies [4]: Polarized light was shone on a metal coated diffraction grating, leading to anomalies in the reflected light. The first theoretical description of this effect is referred to Lord Rayleigh [5]. The first sound theory of particle plasmons is attributed to Gustav Mie [6] in 1908. He considered nano sized spherical metallic particles that give rise to spectral modifications of the scattered field. In 1957 the pioneering work of Ritchie proposed a theoretical description of electron energy losses due to interaction of a swift electron with a metal foil [7] coming from the excitation of surface plasmons. This effect was observed two years later [8] and marked the beginning of electron energy loss spectroscopy for surface plasmons. The excitation of surface plasmons with light was simultaneously developed by Kretschmann [9] and Otto [10]. Both configurations use the evanescent fields of totally internally reflected light from glass prisms in order to excite surface plasmons at thin metal films. Since then plasmonics has emerged as a fast growing research field, with strong inputs from the development of chemical synthesis and electron beam lithography, which lead to a whole bunch of new geometries for investigation. Further, the hype in plasmonics arouse from foreseen and already working applications [1, 11].

Possible applications include, but are not limited to, (bio-) sensors, medical applications (cancer therapy) and plasmonic circuits [1, 11]. Sensors rely on the effect that the surface plasmon resonances are slightly shifted if another dielectric medium is brought into the vicinity of a plasmonic particle, see e.g. [12]. Medical applications include cancer therapy, where the heating of plasmonic nanoparticles is used to destroy cancer cells, which is termed plasmonic phototermal therapy and has already been applied in vivo studies on mice [13]. Plasmonic circuitry deals with the implementation of plasmons into photonic circuits, in order to shrink their size to the nanometer regime. The optimal design of the building blocks of such circuits - plasmonic waveguides - is currently under heavy development [14].

Theoretical description

The theoretical description of surface plasmons usually considers the optical response of a metal due to some exciting electromagnetic field. The question arises, whether this should be done in a quantum mechanical way or in a classical way, since the involved metallic structures usually have dimensions at the nanometer scale, close to the quantum mechanical regime, but for most structures considered for surface plasmons, the dimensions are large enough to use a classical description[1], i.e. Maxwell's theory of light, and incorporate quantum mechanical material effects in a phenomenological frequency-dependent response function, the so called dielectric function $\epsilon(\omega)$.

A simple model for the dielectric function of a metal is the so called Drude or Drude-Sommerfeld model, see e.g. [15], which treats a metal as a free electron gas with negative charge and a fixed positively charged ionic background. When an oscillating external electric field is applied, the electron gas begins to oscillate around the positive ionic background, leading to a polarization which is strongest in the volume at a certain material dependent volume or bulk plasma frequency ω_p. By comparing with the macroscopic polarization of Maxwell's equations, one finds a response function $\chi(\omega)$ and, accordingly, a dielectric function $\epsilon = 1 + \epsilon_0\chi(\omega)$, which reads

$$\epsilon_{Drude}(\omega) = 1 - \frac{\omega_p^2}{\omega^2 + i\gamma\omega}. \tag{1.1}$$

Here $\gamma = v_F/l$ is a damping term with v_F the Fermi velocity and l the electron free mean path. Although this model already gives quite good results for the optical response of metals - especially for gold and silver for wavelengths above 700 nm - it does not account for interband transitions of bound electrons, which can be supplemented by using a similar ansatz as in the Drude model, but for bound electrons, see e.g. [15]. A comparison between the dielectric functions obtained from optical experiment [16] and the Drude model with and without interband transitions in an energy range between 1 and 3.5 eV is given in Fig. 1.1 for gold. As can be seen, below 2 eV the Drude model is in good agreement with experiment, but for higher energies interband transitions need to be accounted for.

Having a function for the material parameters, we are seeking for a solution of Maxwell's equations that are evanescent (decaying away) from the surface and traveling along the surface of the metal. In other words, we are searching either for the eigenmodes of closed dielectric bodies or for electromagnetic waves that have an imaginary wave vector in the direction normal to the surface and only propagate along the surface.

Planar interface between two media We look at a planar interface between two media and search for a homogeneous solution of the electric field wave equation - i.e. a solution of the electric field that exists without external excitation, which is localized at the interface (see e.g. [15]). One finds a dispersion relation for the excitation of surface

[1] Quantum mechanical effects typically set in when the Fermi wavelength of the electrons in the metal is comparable to the particle dimension, which is for noble metals at the order of Angstroms.

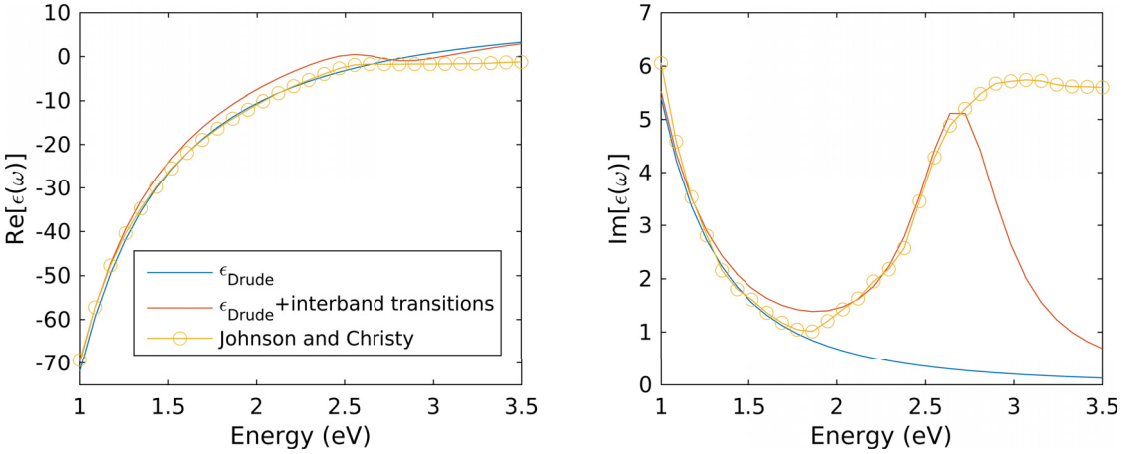

Figure 1.1: Dielectric function of gold for Drude model without and with interband transitions, and comparison with experimental data from [16]. Left and right figure show the real and imaginary part of dielectric function, respectively. Plateau in experimental data of imaginary part above 2.5 eV is attributed to d-band transitions of electrons in gold. For silver (not shown here) such high damping due to interband transitions sets in above 3.5 eV.

plasmons propagating along the interface. By denoting k_x the wavenumber into the plasmon propagation direction, and ϵ_1 and ϵ_2 the dielectric functions of the two half spaces, respectively, one arrives at a dispersion relation and a relation for the wave vector component normal to the interface plane [15]

$$k_x^2 = \frac{1}{c^2}\frac{\epsilon_1\epsilon_2}{\epsilon_1+\epsilon_2}\omega^2, \; k_{j,z}^2 = \frac{\epsilon_j^2}{\epsilon_1+\epsilon_2}k^2, \tag{1.2}$$

where j is the index to medium j. Let us for simplicity assume that the imaginary parts of the dielectric functions can be neglected. In order to get a solution traveling in x-direction we need a real k_x. Further, to be bound to the interface, we demand purely imaginary $k_{j,z}$. Then, from inspection of Eq. (1.2) we find that the dielectric functions of the two media have to fulfill

$$\epsilon_1(\omega)\cdot\epsilon_2(\omega) < 0 \tag{1.3}$$

$$\epsilon_1(\omega)+\epsilon_2(\omega) < 0 \tag{1.4}$$

in order to get a solution decaying exponentially away from the surface and traveling along the interface. In other words, this means that one of the dielectric functions has to be positive, while the other one needs to be negative. Further, the absolute value of the negative dielectric function has to exceed the value of the positive one. Therefore metals - as they have a large negative real part and a small positive imaginary part of the dielectric function in the energy range of visible light - are a good choice as materials

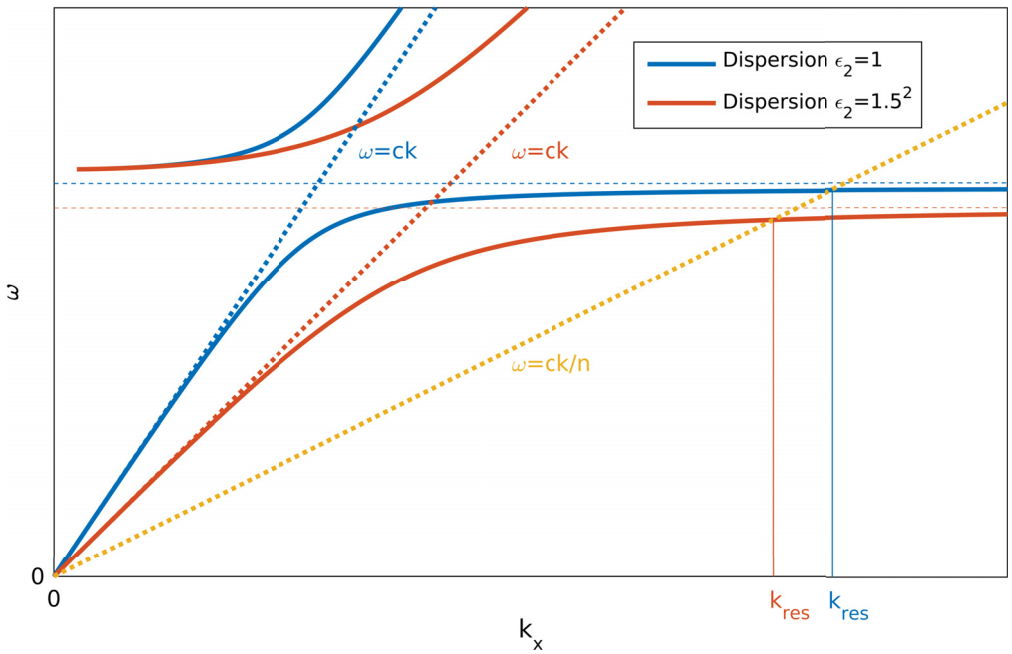

Figure 1.2: Surface plasmon dispersion relation for interface between gold (Drude model) and dielectric with $\epsilon_2 = 1$ and 2.25. Below the dashed line surface plasmons are excited, above the dispersion for bulk plasmons is shown. Bulk plasmons can not be excited by transversal electromagnetic fields because they are longitudinal waves. Dotted lines show light dispersion in medium with dielectric constant ϵ_2 and yellow dotted line shows dispersion of light tilted by medium with refractive index $n = 2$. k_{res} is the wave vector component in x-direction where a surface plasmon can be excited due to yellow light line.

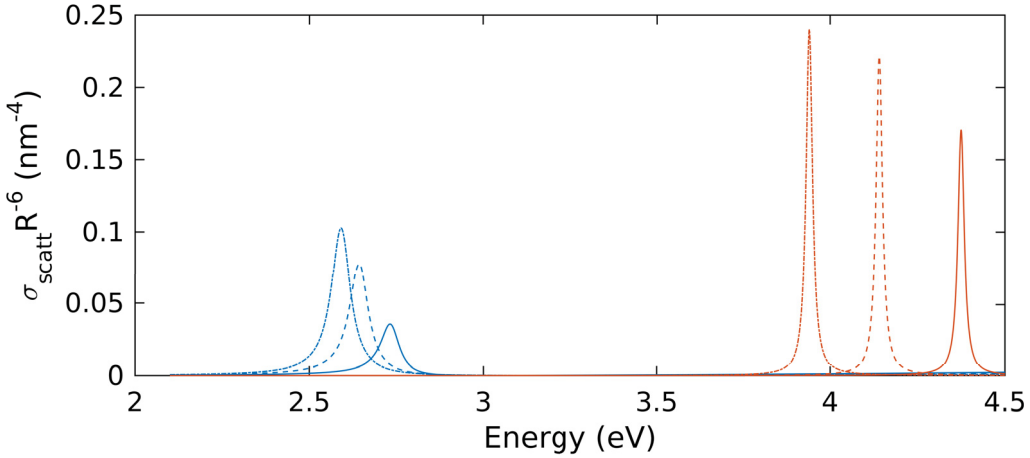

Figure 1.3: Surface plasmon resonances of metallic nanospheres. Blue lines correspond to gold nanospheres (values are multiplied with a factor of 200), red lines to silver nanospheres. For the dielectric functions we used the Drude model with material parameters as in [18]. The data are normalized with R^{-6}, where R is the radius of the sphere. Solid, dashed and dashed-dotted lines correspond to a refractive index of the embedding medium $n = 1,\ 1.33,$ and 1.5, respectively.

for the excitation of surface plasmons. Especially gold and silver show good behavior due to very low losses in the visible frequency spectrum. Usually the second material is then a dielectric with small positive real dielectric constant, like air or glass. When one looks at a glass/metal interface and does not neglect the imaginary part of the dielectric function of the metal, one arrives at a k_x with imaginary part, accounting for ohmic losses in the metal. In Fig. 1.2 we look at the dispersion relation of Eq. (1.2) and find that for the excitation of surface plasmons on films with light an additional restriction comes up, namely energy and momentum conservation. Light excitations of surface plasmons can only be achieved when the wave vector of light is diminished by a dielectric with dielectric constant greater than one. Otherwise the wave number of light in the dielectric medium is too small to cross the dispersion curve of surface plasmons. Naively, one would think that by setting ϵ_2 to a higher value than one, a crossing of the light line and the surface plasmon dispersion relation is possible. But then the surface plasmon dispersion relation is also tilted by the same factor. Therefore one has to find a way to slow down light and bring it to the interface region where surface plasmons propagate. Experimental realizations of tilting the light line in order to excite surface plasmons at films are the Otto [10] and Kretschmann [9] configuration, respectively. Here the evanescent fields of total internal reflection of prisms are used. The dispersion relation can also be probed by swift electrons as is done in [17]. In addition, the authors show that for the resonances of metallic nanoparticles a similar dispersion relation holds.

Surface plasmons in metallic nanoparticles Resonances of metallic nanoparticles are found by solving Maxwell's equations for a homogeneous medium embedded in another homogeneous medium. For a sphere [6], and some other special geometries, the equations can be worked out analytically and yield equations for important physical quantities such as scattering or extinction, which show the resonance energies of particle plasmons. In the quasi-static case, the scattering cross section $\sigma_{scatt}(\omega)$ for a sphere is

$$\sigma_{scatt}(\omega) = \frac{8\pi}{3} R^6 k^4 \left| \frac{\epsilon_1(\omega) - \epsilon_2}{\epsilon_1(\omega) + 2\epsilon_2} \right|^2 , \tag{1.5}$$

where ϵ_1 and ϵ_2 are in- and outside dielectric functions of metal and surrounding, respectively, k is the vacuum wave number and R corresponds to the radius of the metallic sphere. So, for particles small compared to the wavelength of the exciting electric field, only the material properties allow for surface plasmon excitations. If we use the Drude dielectric function of gold and silver, respectively as $\epsilon_1(\omega)$ and $\epsilon_2 = 1$ for vacuum we get the resonances shown in Fig. 1.3 in the visible energy spectrum. Only the dipolar mode shows up in the spectrum. The width of the resonances is attributed to radiation and ohmic losses of the surface plasmon. For gold these losses are much stronger than for silver and the position of the resonances is also dependent on the chosen material. Further, the resonances can be shifted to higher energies, by using an embedding medium with a higher refractive index $n = \sqrt{\epsilon}$.

More modes can be excited, when the excitation wavelength is of the order of the sphere diameter. Then the resonance position is dependent on R and one has to refrain from the quasi-static approximation and use the full Maxwell equations for the evaluation of the optical properties. For spheres one can resort to Mie theory [6].

If the particle shape is altered, also modifications in the plasmon energy arise. When two particles are in close distance to each other the surface plasmons of each mode begin to interact via their electromagnetic fields and a mode hybridization leads to bonding and anti-bonding modes, see e.g. [19].

2 Imaging plasmons with EELS

Surface plasmons are confined to the surface of metallic nanonstructures and therefore their electromagnetic fields are also confined to the nanoregime. Furthermore, the fields are decaying exponentially away from the surface, and for moderate particle sizes only the dipole radiation is transfered to the far-field. Thus, in order to image the spatial and spectral profile of particle plasmons, a microscopy technique which probes electromagnetic fields with nanometer resolution and sub-eV spectral resolution is needed. There exist mainly three approaches to interact with surface plasmons: excitation with light, quantum emitters, and fast electron beams.

When plasmons are excited by optical far-field microscopy one usually gets a resonance peak in the scattering or extinction spectra at the plasmon resonances, but no spatial information. That is, because the resolution of optical microscopy is restricted by the diffraction limit of light to about $\lambda/2$ (Fig. 2.1).

It is possible to overcome the far-field resolution limit by scanning near-field optical microscopy (SNOM). Here the specimen is excited by light and the evanescent fields are probed by placing a detector - usually a sharp tip of glass or silicon - in close proximity (much smaller than the exciting wavelength) of the specimen. It is also possible to invert the scheme and to use the tip to illuminate the sample at a certain spot and measure the induced near- or far-fields of the sample. This technique achieves a lateral resolution of about 20 nm [20].

In contrast to that, in electron energy loss spectroscopy (EELS) an electron beam is used as the excitation and probe source. This gives loss spectra with nanometer resolution due to the short electron wavelength at typical resonance energies (Fig. 2.1), therefore establishing a great tool to extract information about the near field of surface plasmons. By raster scanning the specimen with the electron beam, one achieves detailed spatial information with nanometer resolution [21, 22].

2.1 EELS in experiment

The experimental technique was already developed in the 1940s by Hillier and Baker [24], but not widely used for plasmon imaging until advances in microscope instrumentation (monochromated electron beam and aberration correction) led to better spatial and energy resolution. While the spectra at a fixed beam position have been measured for decades [25], the spatial electron energy loss map of surface plasmons at a certain resonance energy has been measured only recently [22, 21]. Currently, nanometer resolution for various particle shapes and sizes has been achieved and new plasmon modes have been observed [26, 27, 28]. A comprehensive review of EELS in experiment is given in [29].

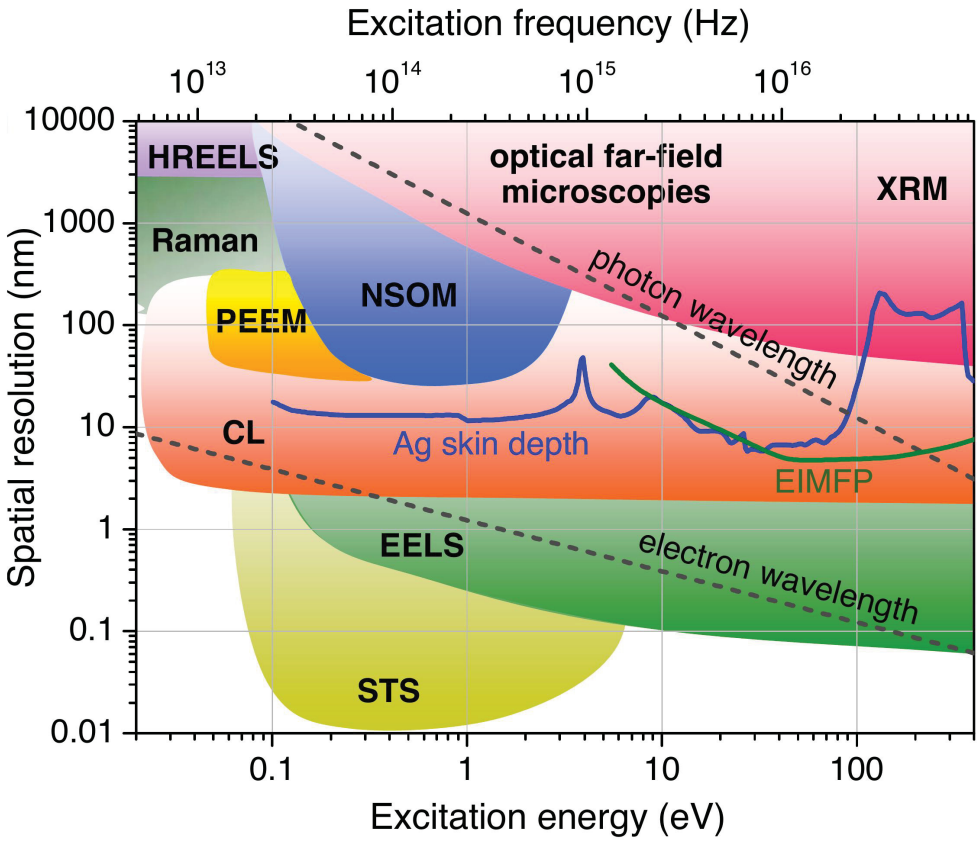

Figure 2.1: Lateral and spectral resolution of different microscopy techniques: Resolution is limited to fractions of the wavelength of the probe. The photon wavelength is much larger than the electron wavelength at typical excitation energies of plasmons, leading to higher spatial resolution. Image taken from [23].

There are two main types of setups: Scanning transmission electron microscope (STEM), where the electron probe is raster scanned over the specimen and at each position a spectrum is recorded, and electron filtered transmission electron microscopy (EFTEM), where an electron beam interacts with the sample and spatial information at a fixed energy is obtained. While the STEM approach gives excellent energy resolution, the EFTEM setup measures large areas with high spatial resolution in comparable short acquisition time [30].

The main principle of transmission electron microscopy is depicted in Fig. 2.2: Swift monochromated electrons with kinetic energies of 80 to 200 keV are passing by or penetrating the specimen. The information from elastically scattered electrons is used to get high angle annular dark-field images, while the inelastically scattered electrons are spectrally fanned out and recorded by a CCD camera. The recorded data show the kinetic energy of the electron and therefore the spectral information at an electron beam position.

The resulting spectral information, which can be resolved with about 0.1-0.3 eV, usually has to be post-processed to show the desired resonance peaks, e.g. the zero-loss peak (no interaction of electron with specimen) has to be subtracted from the spectra because it superimposes the plasmon resonances, which are usually found at energies of only a few eV at the tail of the zero-loss peak. Further, non negative matrix factorization is sometimes used to resolve the contributions of single plasmon resonances [31] and the zero-loss peak.

Altogether performing the experiments is very tough: one needs a highly monochromated, focused electron beam for energy and spatial resolution. Furthermore, the preparation of samples is complicated and contamination before and during the measurement has to be suppressed.

2.2 EELS theory

The theoretical framework of EELS is well established and can be found in various articles and reviews, e.g. [23, 32]. Here we follow more or less [23]. We use Gaussian units throughout and only consider non-magnetic materials, i.e. we set the permeability $\mu = 1$, which is for the typical metals in use for plasmon measurements a good approximation.

The theoretical description takes into account two key ingredients of electron energy loss which are formulated in a semi-classical framework: First, the electric field of a swift electron excites a surface plasmon. Second, the induced field of the surface plasmon acts back on the electron, leading to the energy loss of the electron.

2.2.1 Loss probability

The work done by a charge at position $\mathbf{r}(t)$ against an electric field is described conveniently as

$$dW = -q\mathbf{E}(\mathbf{r}(t), t) \cdot \mathbf{v}, \tag{2.1}$$

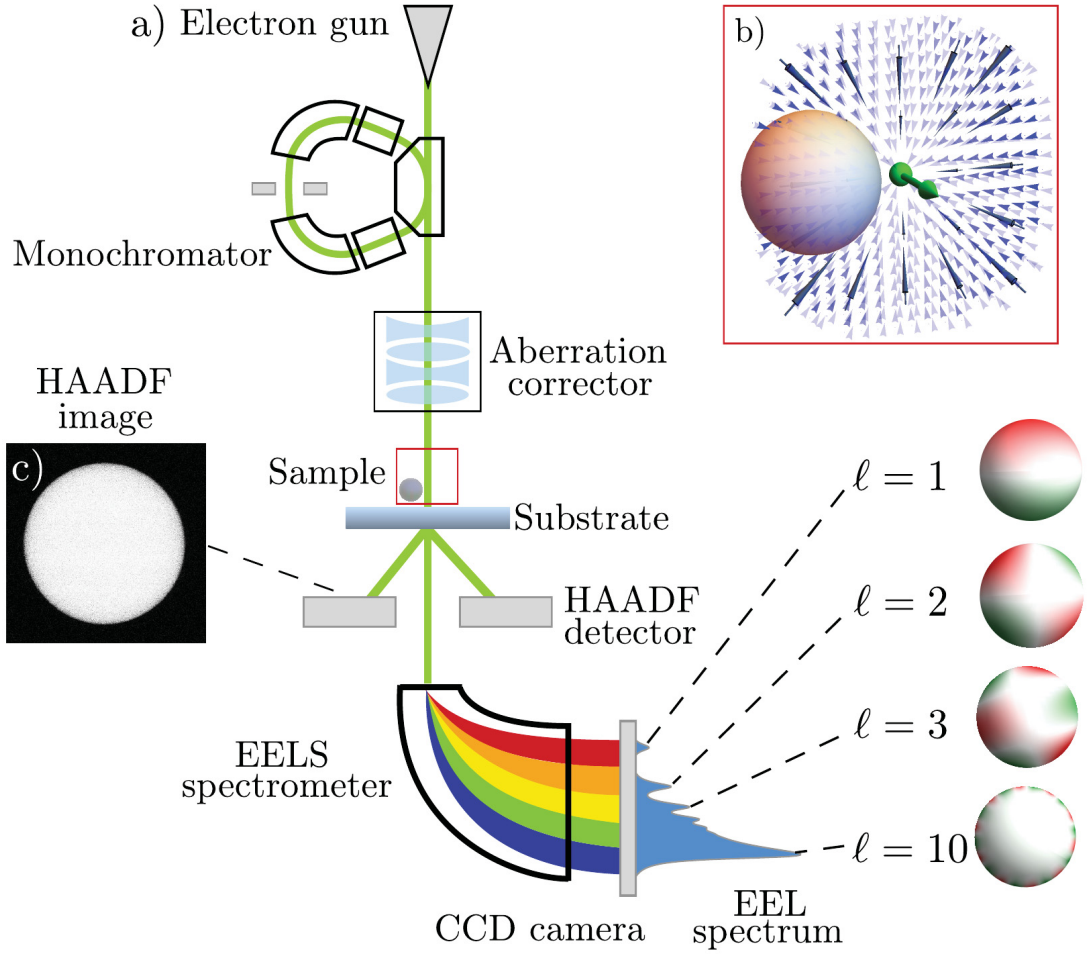

Figure 2.2: Scheme of experimental setup for electron energy loss spectroscopy. a) An electron gun shoots fast electrons with velocities of 0.1 to 0.8 times the velocity of light. A monochromator narrows the energy distribution of electrons and an aberration corrector minimizes the electron probe size. After the corrector the probe interacts with the sample which is placed on a substrate. Then the electron energy is spectrally fanned out with a spectrometer and measured with a CCD camera. b) Scheme of the electric field of an electron in close vicinity of a specimen. c) Electrons scattered from nuclei are collected by high-angle annular dark-field detector, producing an image of the specimen. Image taken from [25].

where we have omitted the magnetic contribution of the Lorentz force because it vanishes for the inner product with $\mathbf{v}$. For the total work of a fast moving electron against an electric field we integrate over the whole electron path:

$$\Delta E = e \int_{-\infty}^{\infty} dt \mathbf{v} \cdot \mathbf{E}^{ind}(\mathbf{r}_e(t), t). \tag{2.2}$$

Here we assume that the electron path goes from $-\infty$ to ∞, which is a good estimate for EELS with plasmonic particles, because of the evanescent character of the involved fields and the small specimen compared to the electron path. The electron path can be estimated as a straight line which is not modified by the induced plasmon field. This is simply because the high kinetic energies of the electron in an electron microscope (several tens to hundreds of keV not far away from the speed of light) are not changed noticeably by the energy loss of a plasmon (eVs), and therefore the velocity vector stays practically the same. So we safely write for the electron trajectory

$$\mathbf{r}_e(t) = \mathbf{R}_0 + \hat{\mathbf{z}} v t, \tag{2.3}$$

where without loss of generality, we assume the electron trajectory to propagate along the positive z-direction and we define the impact parameter $\mathbf{R}_0 = (x_0, y_0, 0)$.

The induced electric field can be decomposed into different frequency contributions by a Fourier transform. Then it reads

$$\mathbf{E}^{\mathrm{ind}}(\mathbf{r}(t), t) = \frac{1}{2\pi} \int_{-\infty}^{\infty} d\omega e^{-i\omega t} \mathbf{E}^{\mathrm{ind}}(\mathbf{r}(t), \omega), \tag{2.4}$$

and we use the definition $\Delta E = \int_0^{\infty} d\omega \hbar\omega \Gamma_{EELS}(\mathbf{R}_0, \omega)$ for the loss probability per energy $\hbar\omega$ to finally arrive at

$$\Gamma_{EELS}(\mathbf{R}_0, \omega) = \frac{e}{\pi\hbar\omega} \int_{-\infty}^{\infty} dt \ \mathrm{Re}[e^{-i\omega t} \mathbf{v} \cdot \mathbf{E}^{\mathrm{ind}}(\mathbf{r}(t), \omega)]. \tag{2.5}$$

Here, we used the property, that for real fields the Fourier transform $\mathbf{E}^{\mathrm{ind}}(\mathbf{r}, \omega) = \mathbf{E}^{\mathrm{ind}}(\mathbf{r}, -\omega)^*$. Then the antisymmetric part of the ω-integral (imaginary part) vanishes and the integral limits can be changed from $\omega \in (-\infty, \infty)$ to $\omega \in (0, \infty)$. If we set $z = vt$ and $\mathbf{v} = \hat{\mathbf{z}} v$ we arrive at

$$\Gamma_{EELS}(\mathbf{R}_0, \omega) = \frac{e}{\pi\hbar\omega} \int_{-\infty}^{\infty} dz \ \mathrm{Re}[e^{-i\omega z/v} E_z^{\mathrm{ind}}(\mathbf{R}_0, z, \omega)]. \tag{2.6}$$

Eqs. (2.5) and (2.6) show that if we know the induced electric field we immediately are in position to compute the electron loss probability $\Gamma_{EELS}(\mathbf{R}_0, \omega)$. Further, we detect that EELS only probes the z-component of the induced electric field.

Having derived this final form for $\Gamma_{EELS}(\mathbf{R}_0, \omega)$ we want to evaluate the last unknown, the induced electric field and for that we need the electric field of a swift electron.

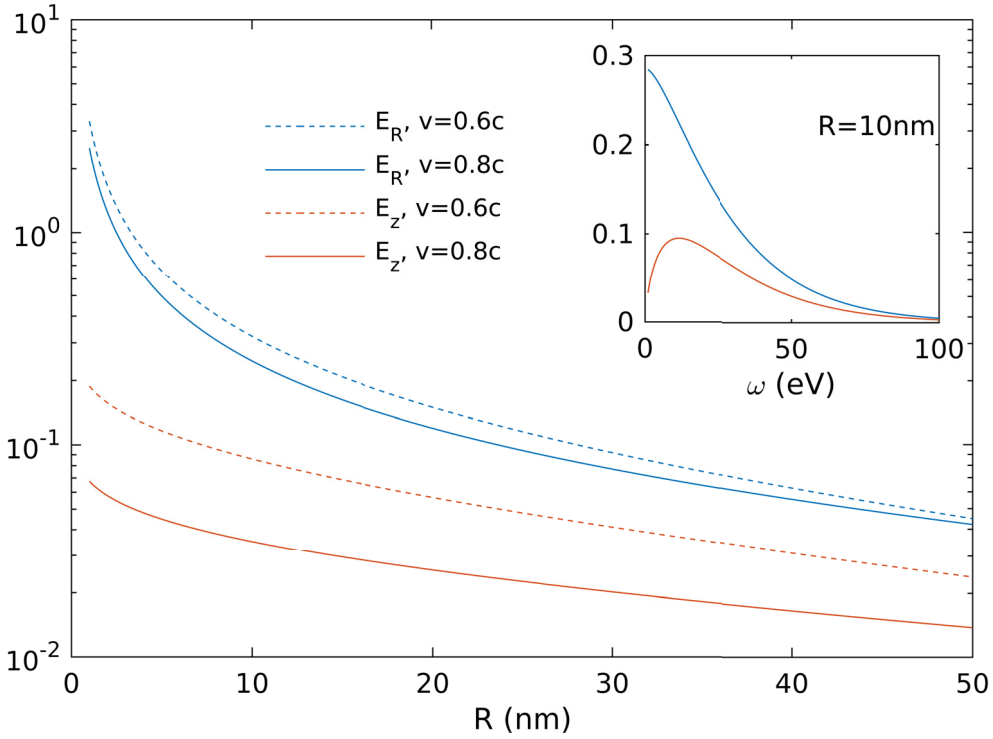

Figure 2.3: Radial and z part of electric field for electron traveling with velocity v along z-direction. Velocities in units of speed of light c are reported in the figure. Inset displays the dependency of the electric field on energy for an observation point with R=10 nm.

2.2.2 Field of swift electron

A swift electron, as it occurs in an electron microscope can be described as a moving point charge

$$\rho(\mathbf{r},t) = -e\delta(\mathbf{R}-\mathbf{R}_0)\delta(z-vt), \tag{2.7}$$

with in plane coordinates $\mathbf{R} = (x, y, 0)$ and velocity v, which is typically at the order of speed of light c. To work out the equations for the electric field of of a swift electron it is favorable to switch to frequency space. Therefore we Fourier transform the charge distribution and get

$$\rho(\mathbf{r},\omega) = \int dt e^{i\omega t}\rho(\mathbf{r},t) = -\frac{e}{v}\delta(\mathbf{R}-\mathbf{R}_0)e^{iqz}. \tag{2.8}$$

Here we introduced the wavenumber $q = \omega/v$. For a homogeneous dielectric environment with dielectric function $\epsilon(\omega)$, the electric field for this charge distribution can be determined by the so called Liénard-Wiechert potentials, see e.g. [33]. The derivation yields [23]

$$\mathbf{E}(\mathbf{r},\omega) = \frac{2e\omega}{v^2\gamma_\epsilon\epsilon}e^{iqz}\left[\frac{i}{\gamma_\epsilon}\mathrm{K}_0\left(\frac{\omega\rho}{v\gamma_\epsilon}\right)\hat{\mathbf{z}} - \mathrm{K}_1\left(\frac{\omega\rho}{v\gamma_\epsilon}\right)\hat{\boldsymbol{\rho}}\right], \tag{2.9}$$

where we have introduced the radial vector is $\boldsymbol{\rho} = \mathbf{R} - \mathbf{R}_0$ together with the Lorentz contraction factor $\gamma_\epsilon = 1/\sqrt{1-\epsilon v^2/c^2}$, and K_n are the modified Bessel functions (or sometimes also called hyperbolic Bessel functions) of the second kind of order n. The electric field decays with increasing radial distance due to the behavior of the modified Bessel functions at large distances, as can be seen in Fig. 2.3, and the electric field pointing in direction of the electron velocity vector is smaller than the radial part of the electric field. If we look at the energy spectrum (see inset Fig. 2.3), we discover a more intricate behavior. Interestingly the electron field decreases with increasing velocity, because of the implicit dependence in γ_ϵ.

Sometimes it is easier to work with the vector potential, rather than with the electromagnetic fields (especially for the boundary element approach discussed later), and therefore we state for the potentials of a swift electron within the Lorentz gauge

$$\phi(\mathbf{r},\omega) = -\frac{2e}{v\epsilon}e^{iqz}\mathrm{K}_0\left(\frac{\omega\rho}{v\gamma_\epsilon}\right),\ \mathbf{A}(\mathbf{r},\omega) = \epsilon\frac{\mathbf{v}}{c}\phi(\mathbf{r},\omega). \tag{2.10}$$

2.2.3 Induced electric field of an electron beam

Quite generally by solving the electric wave equation for a given current distribution and dielectric function $\epsilon(\mathbf{r},\omega)$ we find the electric field everywhere. When we deal with linear dielectric media, i.e. $\mathbf{D} = \epsilon(\omega)\mathbf{E}$, we can obtain the solution of the wave equation for a general current distribution from a linear superposition of point-like current sources. To incorporate all possible orientations of current sources we seek for solutions of point-like current distributions defined for x-, y- and z-direction: $\mathbf{j}_i(\mathbf{r}) = \delta(\mathbf{r}-\mathbf{r}')\hat{e}_i$, where $i = x, y, z$. The solution of the wave equation for each orientation can be written as a vector $\mathbf{g}_i(\mathbf{r},\mathbf{r}')$. We use tensors to include all three orientations in compact form and

write for the delta-like sources $\mathbf{j}(\mathbf{r}) = \delta(\mathbf{r} - \mathbf{r}')\mathbb{1}$ and for the Green function solutions $\mathbf{G}(\mathbf{r}, \mathbf{r}') = [\mathbf{g}_x, \mathbf{g}_y, \mathbf{g}_\mathbf{z}]$, respectively. Then the wave equation reads

$$\nabla \times \nabla \times \mathbf{G}(\mathbf{r}, \mathbf{r}', \omega) - k_0^2 \epsilon(\mathbf{r}, \omega)\mathbf{G}(\mathbf{r}, \mathbf{r}', \omega) = -\frac{1}{c^2}\delta(\mathbf{r} - \mathbf{r}')\mathbb{1}, \tag{2.11}$$

where $\mathbf{G}(\mathbf{r}, \mathbf{r}', \omega)$ is the dyadic Green function and $k_0 = \omega/c$ is the wavenumber in vacuum. We only take into account a local dielectric function $\epsilon(\mathbf{r}, \omega)$ which does not depend on $\mathbf{r}'$ and we demand for $\mathbf{G}$ outgoing boundary conditions, i.e. solutions vanishing at infinity. Then

$$\mathbf{E}(\mathbf{r}, \omega) = -4\pi i\omega \mathbf{G}(\mathbf{r}, \mathbf{r}'\omega) \cdot \mathbf{j}(\mathbf{r}'), \tag{2.12}$$

or in other words, for a point-like current distribution $\mathbf{j}(\mathbf{r}')$ the dyadic Green function computes the electric field at $\mathbf{r}$ for a given dielectric environment and at frequency ω. $\mathbf{G}$ is also called the electric Green tensor of Maxwell's equations, and the first, second and third column correspond to the x-, y- and z-direction, respectively.

Armed with the solution for a point-like current distribution it is now an easy task to formally solve the electric field for an arbitrary current distribution $\mathbf{J}(\mathbf{r}, \omega)$ by integrating over the whole volume:

$$\mathbf{E}(\mathbf{r}, \omega) = -4\pi i\omega \int d\mathbf{r}' \mathbf{G}(\mathbf{r}, \mathbf{r}', \omega) \cdot \mathbf{J}(\mathbf{r}', \omega). \tag{2.13}$$

So, if we find the dyadic Green function for a dielectric environment with dielectric function $\epsilon(\mathbf{r}, \omega)$, we immediately are in position to obtain the electric field at $\mathbf{r}$ produced by an arbitrary current distribution.

Analytic forms of the dyadic Green function can only be found for a very restricted number of geometries, such as layer structures, spheres, prolate sphere or infinitely long cylinders (see e.g. [34] for a textbook or [35, 36, 37] for multi-layered spheres and cylinders). Nonetheless these analytic expressions can be very useful as a check for numerical simulation techniques. For more involved geometries numerical simulation techniques are inevitable.

2.2.4 EELS in terms of dyadic Green function

By inserting Eq. (2.13) in Eq. (2.6) and knowing that the current produced by a swift electron is $\mathbf{J}_e(\mathbf{r}, \omega) = \mathbf{v}\rho(\mathbf{r}, \omega)$ we find for the electron energy loss probability

$$\Gamma_{EELS}(\mathbf{R}_0, \omega) = -\frac{4ev^2}{\hbar} \int_{-\infty}^{\infty} dr dr' \ \mathrm{Im}\left[\mathbf{J}^*(\mathbf{r}, \omega) \cdot \mathbf{G}(\mathbf{r}, \mathbf{r}', \omega) \cdot \mathbf{J}(\mathbf{r}', \omega)\right]. \tag{2.14}$$

From inspection of Eq. (2.14) we find that the electron energy loss occurs in a two step process: First the current distribution of the electron interacts with the dielectric environment by means of the dyadic Green tensor, leading to the induced electric field, which in turn acts back on the current distribution, leading to the energy loss.

Assuming a straight line trajectory in the z-direction $\mathbf{r}_e(t) = \mathbf{R}_0 + \hat{\mathbf{z}}vt$ and making the abbreviation $\mathrm{G}_{\mathrm{zz}} = \hat{\mathbf{z}} \cdot \mathbf{G} \cdot \hat{\mathbf{z}}$, we arrive at

$$\Gamma_{EELS}(\mathbf{R}_0, \omega) = -\frac{4e}{\hbar} \int_{-\infty}^{\infty} dz dz' \ \mathrm{Im}\left[e^{iq(z-z')}\mathrm{G}_{\mathrm{zz}}(\mathbf{R}_0, z, \mathbf{R}_0, z', \omega)\right]. \tag{2.15}$$

This connection between EELS and the dyadic Green function was first stated in [38] and it can be shown that the loss is independent on whether the electron is traveling in the positive or negative z-direction.[1]

For electron trajectories passing through a dielectric body, e.g. a metallic sphere, it is appropriate to decompose the loss signal into a surface and a bulk contribution. The surface contribution appears from induced charges and currents on the surface between adjacent media, and the bulk contribution from electron energy loss inside a material. The bulk contribution is roughly proportional to $\mathrm{Im}[-1/\epsilon]$ [23]. Thus, we split the dyadic Green function into $\mathbf{G} = \mathbf{G}_{\mathrm{ind}} + \mathbf{G}_{\mathrm{bulk}}$ and insert the splitted Green function into Eq. (2.15) to obtain

$$\Gamma_{EELS}(\mathbf{R}_0, \omega) = -\frac{4e}{\hbar} \int_{-\infty}^{\infty} dz dz' \ \mathrm{Im}\left[e^{iq(z-z')} \mathbf{G}_{\mathrm{ind,zz}}(\mathbf{R}_0, z, \mathbf{R}_0, z', \omega)\right] + \Gamma_{\mathrm{bulk}}(\omega), \quad (2.16)$$

where

$$\Gamma_{\mathrm{bulk}}(\omega) = -\frac{4e}{\hbar} \int_{z_1}^{z_2} dz dz' \ \mathrm{Im}\left[e^{iq(z-z')} \mathbf{G}_{\mathrm{bulk,zz}}(\mathbf{R}_0, z, \mathbf{R}_0, z', \omega)\right], \quad (2.17)$$

where z_1 and z_2 are the z-values where the electron enters and exits the dielectric body, respectively.

For selected geometries, like a planar interface [23], sphere [39] (in the framework of Mie theory), or cylindrical hole [40], there exist analytical expressions, both for quasi-static and retarded case, for the electron energy loss. More involved curved geometries are usually subject to numerical techniques.

2.2.5 EELS in terms of eigenmode expansion

As we are dealing with plasmonic resonances, a decomposition of the loss signal into different mode contributions would be beneficial and give more inside into the physical mechanisms involved.

Such a decomposition can be done in a mathematical sound way for the quasi-static case (when the resonance wavelength is much smaller than the particle dimension, e.g. a sphere when the diameter d is much smaller than the exciting wavelength, i.e. $d \ll \lambda$). For practical implementation also a retarded eigenmode expansion is feasible.

Quasi-static eigenmode expansion

In the quasi-static regime, the wave equation reduces to the scalar Poisson equation. Here we can find - in a similar manner as in the retarded case - a Green function, now a scalar quantity which mediates the action between two positions in space. The electron energy loss probability reduces here to [41, 23]

$$\Gamma_{EELS}(\mathbf{R}_0, \omega) = -\frac{1}{\pi\hbar} \int dz dz' \ \mathrm{Im}\left[\rho^*(\mathbf{r}, \omega) \mathrm{G}_{\mathrm{ind}}(\mathbf{r}, \mathbf{r}', \omega) \rho(\mathbf{r}', \omega)\right], \quad (2.18)$$

[1] By using the reciprocity theorem the exponential factor can be recast into a cosine function outside Im[..] and one finds that the electron energy loss is independent on whether the electron is traveling in the positive or negative z-direction.

where G_{ind} is the induced Green function of the Poisson equation and ρ is again the swift electron charge distribution. Eq. (2.18) is very similar to Eq. (2.14): the two step process is apparent. The main difference lies in the scalar character of the involved quantities. A decomposition of the induced scalar Green function into eigenmodes [42, 43] is possible if only two different media are involved. The defining equation for this quasi-static eigenmodes can be derived from a boundary element method approach (see Appendix or e.g. [18]) and reads

$$\oint_{\partial\Omega} \frac{\partial G(\mathbf{s},\mathbf{s}')}{\partial n}\sigma_k(\mathbf{s}')ds' = \lambda_k\sigma_k(\mathbf{s}),\ \oint_{\partial\Omega} \tilde{\sigma}_k(\mathbf{s}')\frac{\partial G(\mathbf{s}',\mathbf{s})}{\partial n}ds' = \lambda_k\tilde{\sigma}_k(\mathbf{s}), \tag{2.19}$$

where σ_k and $\tilde{\sigma_k}$ are the right and left eigenmodes, respectively and $\partial G/\partial n$ is the derivative of the free Green function with respect to the outer surface normal on the boundary. The eigenmodes are defined solely from the geometry of the particle (through the surface derivative of the Green function) and are therefore also called geometric eigenmodes [44]. This scale and energy independence holds because of the quasi-static approximation. Usually the mode with lowest eigenvalue shows up as the monopole mode (see Fig. 2.4) and must be excluded from the eigenmode expansion, because it is forbidden by charge conservation (sum of charge density of eigenvector unequal to zero). Degenerate modes share the same eigenvalue, but the corresponding charge density is different (Fig. 2.4). At the resonance energies of dipolar and quadrupolar modes, usually a small number of modes shows up, but for higher energies (lower eigenvalues) the modes evolve into a continuum.

The eigenmodes form a complete bi-orthogonal basis set and have a proper orthogonality condition[2]

$$\oint_{\partial\Omega} \sigma_k(\mathbf{s})\tilde{\sigma}_{k'}(\mathbf{s})d\mathbf{s} = \delta_{kk'}. \tag{2.20}$$

The potential of an eigenmode - which is given by the charge density at the particle boundary - can be computed by using the free Green function

$$\phi(\mathbf{r}) = \oint_{\partial\Omega} G(\mathbf{r},\mathbf{s})\sigma_k(\mathbf{s})d\mathbf{s}. \tag{2.21}$$

By assuming that both $\mathbf{r}$ and $\mathbf{r}'$ are located outside the dielectric medium[3] (nanoparticle), one can decompose G_{ind} through the above defined modes - as shown in [44] and in detail in the Appendix - into

$$G_{ind}(\mathbf{r},\omega) = -\frac{1}{\epsilon}\sum_k c_k(\omega)\phi_k(\mathbf{r})\phi_k(\mathbf{r}'),\ c_k(\omega) = \frac{\lambda_k + 2\pi}{\Lambda(\omega) + \lambda_k}, \tag{2.22}$$

where $\Lambda(\omega) = 2\pi(\epsilon_{out} + \epsilon_{in})/(\epsilon_{out} - \epsilon_{in})$ is a material parameter depending on the dielectric functions of surrounding and dielectric medium (e.g. gold or silver). By

[2] An orthogonality condition can also be defined for the right eigenvectors only and then reads $\oint_{\partial\Omega} \sigma_k(\mathbf{s})G(\mathbf{s},\mathbf{s}')\sigma_{k'}(\mathbf{s}')d\mathbf{s}d\mathbf{s}' = \delta_{kk'}$, but when non-smooth boundaries are involved [44] it is favorable to use right and left eigenvectors.

[3] The formulas also work for $\mathbf{r}$ or/and $\mathbf{r}'$ inside the dielectric medium, as can be seen in [44], but here we restrict ourself to the most simple case.

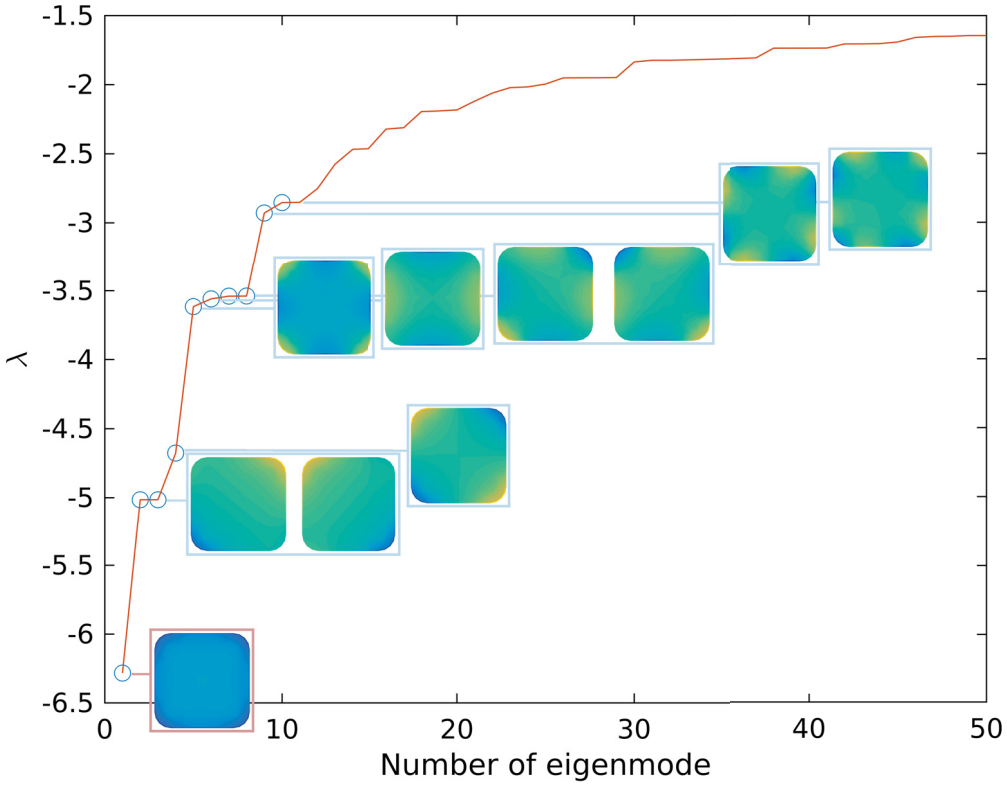

Figure 2.4: First 50 eigenvalues of a rectangle nanoparticle with aspect ratio 5:5:1 (x:y:z), which are independent of material parameters. Insets show eigenmodes associated with eigenvalues on particle surface (charge density of eigenmodes). Red box shows forbidden monopole mode with integrated surface charge density unequal to zero. Degenerate modes with same eigenvalue are displayed within one box.

inspecting Eq. (2.22) we find, that G_{ind} separates into parts depending on energy ω and on geometry, where the energy dependent part gives the weights of the eigenmodes with respect to energy, and the geometry dependent part accounts for the spatial dependence of G_{ind} and therefore also the spatial dependence of the derived quantities (like electric field or EELS). So, if the modes are well separated in energy, the spatial profile of the modes only depends on the geometry of the nanoparticle.

By inserting Eq. (2.22) into (2.18) and some simple algebra one finally arrives at a modal decomposition of the loss probability for electron trajectories passing by a nanoparticle

$$\Gamma_{EELS}(\mathbf{R}_0,\omega) = -\frac{-e^2}{\pi\hbar v^2\epsilon}\sum_k \mathrm{Im}\left[c_k(\omega)\right]\left|\int_{-\infty}^{\infty} e^{iqz}\phi_k(\mathbf{R}_0,z)dz\right|^2. \tag{2.23}$$

At the resonance energy of a mode $\mathrm{Im}[c_k(\omega)]$ results in a Lorentzian line shape function dependent on ω, and the absolute value of the integral corresponds to a coupling strength $F(\omega)$, which leads to a similar behavior as a harmonic oscillator.

As an instructive example we employ a simple model of a harmonic oscillator driven by a fast moving electron coupled with the harmonic oscillator by a dipole (see Fig. 2.5) and compare it with the more complex case of electron energy loss from a metallic nanodisk. As starting point, we write down the equations for the harmonic oscillator coupled to the electric field of a moving electron:

$$\ddot{x} + 2\beta\dot{x} + \omega_0^2 x = (\mathbf{d}\cdot\nabla)\mathbf{E}(\mathbf{r}(t)) = F(\mathbf{r}(t)), \tag{2.24}$$

where β is the damping constant, $\mathbf{d}$ is the dipole moment and ω_0 corresponds to the resonance frequency of the oscillator. The electric field $\mathbf{E}(\mathbf{r}(t))$ of a moving electron can be written as [33]

$$\mathbf{E}(\mathbf{r}(t)) = \frac{\mathbf{r}}{r^3\gamma^2(1-\sin^2\theta)^{3/2}}. \tag{2.25}$$

Here, $\gamma = \sqrt{1-v^2/c^2}$ is the Lorentz contraction factor and θ is the actual angle between the velocity vector $\mathbf{v}$ and $\mathbf{r}$. The energy lost by the electron is equal to the power delivered to the oscillator, which is $F\dot{x}$. The dissipated power can be written as $\beta\dot{x}^2$. The integral over time starting with t_0 gives the work and the dissipated work of the harmonic oscillator

$$W(t) = \int_{t0}^{t} F(r(t))\dot{x}(t)dt,\ W_{diss}(t) = -2\int_{t0}^{t}\beta\dot{x}^2 dt. \tag{2.26}$$

For a simple comparison to the oscillator model above we use Eq. (2.23) and restrict ourself to one contributing mode. Then we can write the displacement of the surface charge as $x(t) \propto \int d\omega e^{i\omega t}c_k(\omega)F(\omega)$, and immediately are in position to compute the work done by the electron $W(t)$ and the dissipative work $W_{diss}(t)$ in the time domain.

A qualitative picture of the time dependency of a metallic nanodisk, driven by a swift electron, and a comparison with a dipole, driven by a swift electron, is given in Fig. 2.5. Clearly, the electron energy loss happens in a short period compared to the exciting frequency resulting in a almost kick-like excitation of the plasmon. The transferred energy then dissipates through ohmic and radiative loss channels of the plasmon.

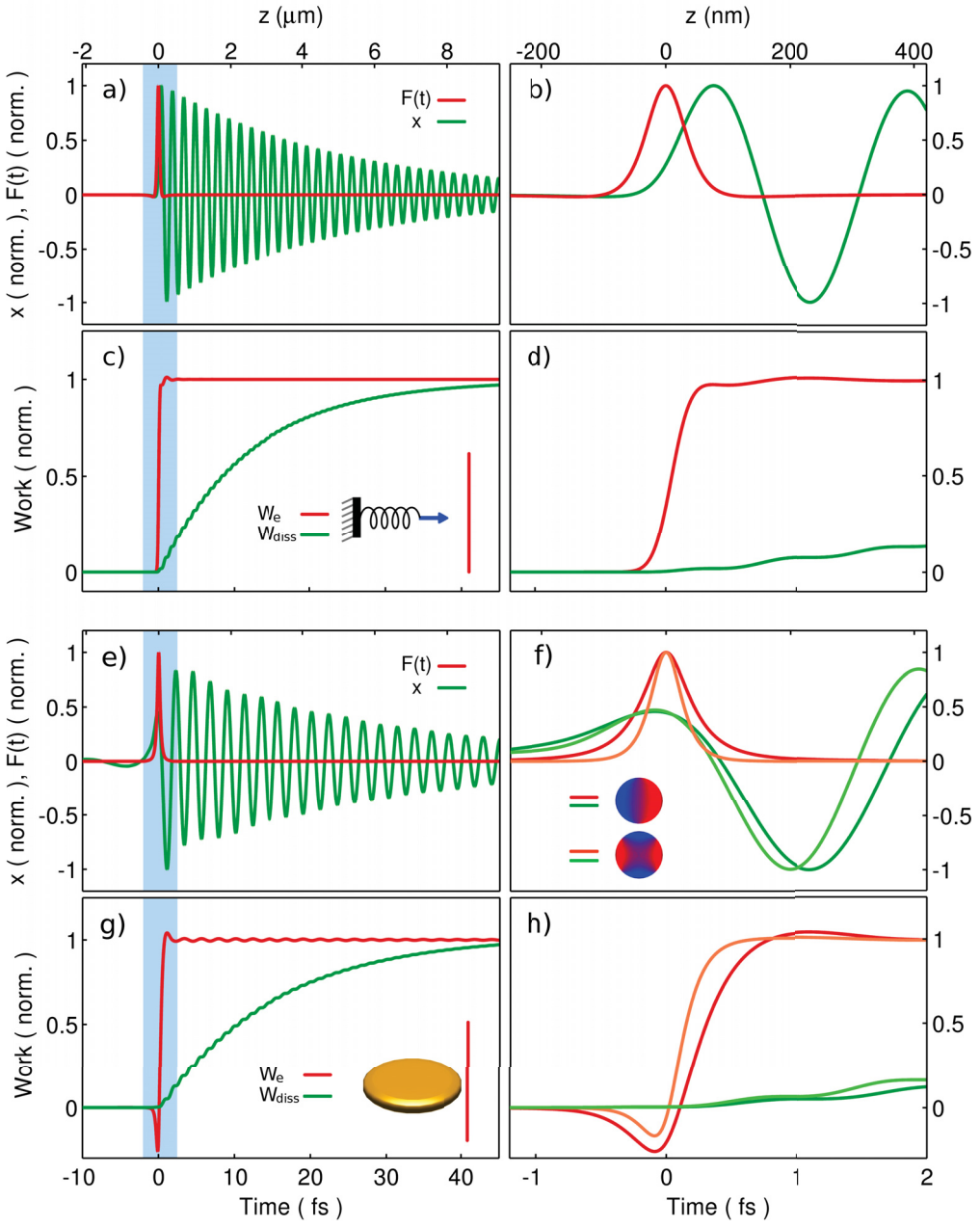

Figure 2.5: e) Force of electron beam (red) acting on nanodisk with diameter 60 nm, height 10 nm, and dielectric function for silver from drude model, and displacement (green) of surface charges. f) Close up of the blue shaded region in e). g) Energy transport from electron to plasmon (red) and dissipated energy (green). h) Close up of the blue shaded region in g). a-d) Same as e-h), but for dipole oscillator pushed by fast electron. Values for harmonic oscillator are $\omega_0 = 2.85$ eV, $\gamma = \omega_0/100$. Electron velocity is 0.7 times the velocity of light and impact parameter is 60 nm away from dipole and the center of disk, respectively.

Retarded eigenmode expansion

In the retarded regime a proper description of modes is more challenging. We will present two slightly different approaches: The first one relies on a central result of Leung et al. [45], the second one is in the spirit of so called constant flux states [46] (see also [47], for a description with boundary integral operators). Although at first glance both approaches look very similar, there are subtle differences.

Quasinormal modes are eigenmodes $f(\mathbf{r},\omega)$ of Eq. (2.11). So we search for non-vanishing solutions with outgoing wave boundary conditions [48]

$$\nabla \times \nabla \times \mathbf{f}(\mathbf{r}) - \frac{\omega^2}{c^2}\epsilon(\mathbf{r},\omega)\mathbf{f}(\mathbf{r}) = 0. \tag{2.27}$$

For non-lossy materials, i.e. real $\epsilon(\mathbf{r},\omega)$, and particles small compared to the resonance wavelength the eigenvalues are real and the quasinormal modes reduce to normal modes. Otherwise we get complex eigenfrequencys ω with a negative imaginary part $i\gamma$. The normalization of these modes is not trivial and can be done with different approaches, see [49, 50]. Techniques for the calculation and normalization of quasinormal modes are e.g. given in [51, 52, 53]. Usually an iterative search algorithm is used to find the complex poles of the eigenmodes. One peculiarity of quasinormal modes is that because of the complex eigenvalues the solutions diverge at the complex resonance frequencies for $\mathbf{r} \to \infty$. Depending on the formalism, this non-physical behavior can be regularized by perfectly matched layers [49].

One can find an approximate modal decomposition of the Green function with quasinormal modes [54]

$$\mathbf{G}(\mathbf{r},\mathbf{r}',\omega) \approx -\frac{c^2}{2\omega}\sum_k \frac{\mathbf{f}_k(\mathbf{r})\mathbf{f}_k(\mathbf{r}')}{\omega-\omega_k}, \tag{2.28}$$

where ω_k is the complex eigenfrequency of mode k. Until now, it has been shown for 1D structures that this decomposition is complete inside the cavity or plasmonic resonator [45]. For 3D structures and outside of a cavity or resonator this is not granted, but approximately correct as has been shown by various studies [55, 48, 56, 54]. Once the relevant modes are calculated - for plasmonic systems usually only a few modes - the approximated Green function describes well the response of the nanoparticle at the considered energy range. By inserting Eq. (2.28) into Eq. (2.14) one obtains a formula for the electron energy loss probability (see [57, 55]).

In a different manner, if we allow a term on the right hand side of Eq. (2.27) unequal to zero, i.e. a $\lambda \neq 0$, we can find eigenmodes close to the complex poles defined at real frequencies ω [46, 47, 53]

$$\nabla \times \nabla \times \mathbf{f}(\mathbf{r},\omega) - \frac{\omega^2}{c^2}\epsilon(\mathbf{r},\omega)\mathbf{f}(\mathbf{r},\omega) = \lambda\mathbf{f}(\mathbf{r},\omega). \tag{2.29}$$

These so called constant flux states depend on energy and thus have to be found for each fixed frequency ω separately. As they are not orthogonal, one has to derive adjoint states $\tilde{\mathbf{f}}(\mathbf{r},\omega)$ from the adjoint equation $\nabla \times \nabla \times \tilde{\mathbf{f}}(\mathbf{r},\omega) - \frac{\omega^2}{c^2}\epsilon^*(\mathbf{r},\omega)\tilde{\mathbf{f}}(\mathbf{r},\omega) = \lambda^*\tilde{\mathbf{f}}(\mathbf{r},\omega)$,

which are bi-orthogonal, i.e. $\int \tilde{\mathbf{f}}_k^*(\mathbf{r},\omega)\mathbf{f}_{k'}(\mathbf{r},\omega)d\mathbf{r} = \delta_{kk'}$. The Green function associated with the solution of Eq. (2.29) can be decomposed into these states inside the resonant structure as [46]

$$\mathbf{G}(\mathbf{r},\mathbf{r}',\omega) \approx -\frac{c^2}{2\omega}\sum_k \frac{\mathbf{f}_k(\mathbf{r},\omega)\tilde{\mathbf{f}}_k^*(\mathbf{r}',\omega)}{\omega-\omega_k}. \tag{2.30}$$

The solutions in the constant flux sense are not diverging for $\mathbf{r} \to \infty$ and are close to the resonance frequency of a quasinormal mode approximately the same as the resonant quasinormal modes, and are therefore suitable for practical implementations. For a comparison of these approaches in the Fredholm integral sense see [47].

2.2.6 Quantum effects

When the size of a plasmonic nanoparticle or the distance between two nanoparticles comes into the order of atomistic length scales, quantum effects have to be taken into account for the theoretical description of plasmons [58]. In [27] it was shown that the resonances of single plasmonic nanoparticles shift to higher energies (up to 0.5 eV) than expected by classical results, when the particle diameter is reduced from 20 to 2 nm. For sufficiently narrow gaps between two nanoparticles, charge tunneling in the gap occurs [28] and charge transfer plasmons appear. This effect shows up for very small gaps only, i.e. gap distance smaller than 0.5 nm. Therefore, molecular tunneling junctions might be beneficial [59] as they enable larger separation between the particles.

The theoretical description of charge transfer plasmons is either done by full quantum mechanical simulations [60], or by extending classical models [61, 62, 63]. Here, usually the dielectric function in a gap region is altered to account for gap tunneling. There has been controversy which dielectric function is suitable to account for gap tunneling, but most approaches use a constant tunneling conductivity [64] with respect to ω for large distances, which in turn yields a constant dielectric function. When the gap is very small, i.e. almost touching particles, one often uses a Drude type dielectric function, similar to the particle material. For intermediate values an interpolation between those two regimes can be done [63].

2.2.7 Connection between EELS and LDOS

Although electron energy loss spectroscopy shows features of the plasmon resonances with nanometer resolution, there is some dubiety about the interpretation of the maps. In other words, it is not completely clear to which physical quantity of the plasmons the measured data are connected.

It was shown, that there exists a direct link between electron energy loss spectroscopy and the photonic local density of states for special geometries [38]. For general particle shapes a direct link is not applicable [65], rather there can be large discrepancies, e.g. in the gap region between coupled plasmonic particles, where there is a high local density of states at certain energies, while electron energy loss is almost blind to such hot spots. This blindness can be attributed to the fact, that electron energy loss spectroscopy only probes the z-component of the induced electric field, averaged over the electron

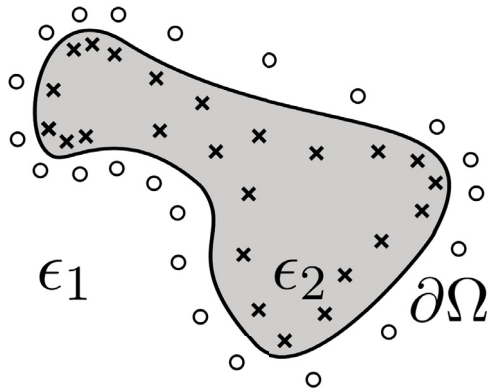

Figure 2.6: Multiple multipole expansion for two adjacent media with dielectric function ϵ_1 and ϵ_2 and boundary $\partial\Omega$. Multipole positions for the expansions of the electromagnetic fields in domain 2 and 1 are delineated as circles and crosses, respectively.

trajectory. By tilting the specimen, this blindness can be often reduced [66]. Further, by using a tomography scheme for rotated energy loss maps, it is possible by solving an inverse problem to reconstruct the photonic local density of states [57].

2.3 Simulation approaches

In this section we will give a short overview of numerical techniques to solve the electromagnetic field problem in presence of dielectric materials. We will go a little bit more into detail for the boundary element method, because it was used as primary simulation tool within this thesis.

2.3.1 Multiple multipole method

For materials with linear and piecewise homogeneous dielectric function and sharp boundaries between adjacent materials one can use a semi-analytic method called multiple multipole method [67, 15] or generalized multipole method. Here the induced electromagnetic fields are described at multiple source points by known analytic solutions $\boldsymbol{\phi_j}$ of the free wave equation such as vector spherical harmonics or plane waves, for arbitrary curved structures (see Fig. 2.6). The field inside individual media with dielectric function ϵ_i can be written as

$$\mathbf{E}^{(i)} = \mathbf{E}_{inc} + \sum_j c_j \boldsymbol{\phi}_j(\mathbf{r}). \tag{2.31}$$

Maxwell's boundary conditions are used to match the series expansions of different domains at the boundary and to numerically find the parameters c_j. This is done usually by

linear least square methods. The delicate part of this approach is to correctly place the multipoles in each domain so that there are not too many multipoles (the computational cost is proportional to the number of multipoles squared) and to find the best suited analytic functions for the studied geometry. An automatic multipole setting scheme was reported in [68]. Once the expansion coefficients are found the electromagnetic field can be computed everywhere else analytically.

This technique has been used for the computation of electron energy loss spectroscopy in [69] for spheroids and for different materials and in [70] for a gold dimer and plasmonic filter applications.

2.3.2 Discrete dipole approximation

This technique was first used in astrophysics [71] and is probably conceptually the most easiest way to derive the response of a dielectric medium to an external field. Here the particle volume is discretized with a number of dipoles located on a three dimensional equidistant grid, and the dipole moment $\mathbf{p}_j(\mathbf{r}_j)$ at position $\mathbf{r}_j$ due to an external electric field and the other dipoles is proportional to the field $\mathbf{E}_j$ at $\mathbf{r}_j$. It reads [72]

$$\mathbf{p}_j(\mathbf{r}_j) = \alpha_j \mathbf{E}_j(\mathbf{r}_j) = \alpha_j \left[\mathbf{E}_{ext}(\mathbf{r}_j) + \sum_{k \neq j}^{N} T_{jk} \mathbf{p}_k(\mathbf{r}_k) \right], \tag{2.32}$$

where T is a dipole-dipole interaction matrix. Eq. (2.32) can be brought in the form of a complex linear system of equations and solved with standard iterative techniques or matrix inversion for the unknown polarizations $\mathbf{p}_j$. Simulations of electron energy loss spectroscopy with a discrete dipole approximation lead to very good results when compared with experiment as shown e.g. in [73] or [74] for electrons not penetrating the plasmonic nano-object.

2.3.3 Finite difference time domain method

In contrast to most other methods used in electromagnetic field calculations, finite difference time domain methods are working in time- and not in frequency-domain. It is the most widely used numerical approach to derive electromagnetic fields and is based on discretization of space and time on a staggered grid [75] and uses second-order central differences to compute the derivatives of Maxwell's equations. Starting with some initial condition the fields are propagated in the time domain. To restrict the computational domain to a finite region so called perfectly matched layers are incorporated, which damp the field solutions away from the simulated structures.

Finite difference time domain implementations for electron energy loss spectroscopy work best for non penetrating electron trajectories and have been introduced recently in [76].

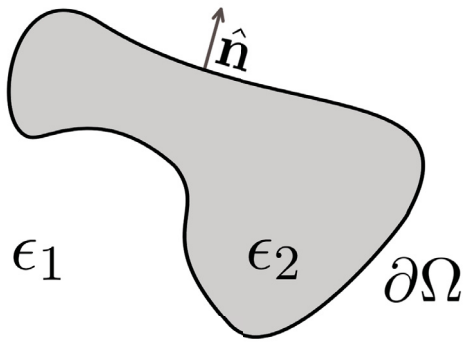

Figure 2.7: Typical arrangement for boundary element method. Two homogeneous media with dielectric function ϵ_1 and ϵ_2 are separated by a sharp boundary $\partial\Omega$. The outwards pointing normal surface vector $\hat{\mathbf{n}}$ is needed for the orientation of the surface.

2.3.4 Boundary element method

In contrast to finite element and DDA methods, boundary element methods do not need to discretize the volume of the specimen, but only the boundaries between different homogeneous media, therefore leading to less discretization elements.

There exist mainly two branches of boundary element methods: The first one uses the Stratton Chu formalism [77] to solve the electric and magnetic fields, while the second one is based on the evaluation of the vector potentials [78]. Both methods work in frequency space and have their pros and cons. The discretization of the boundary can be done either by Galerkin [79] or collocation methods [18, 78].

In the field of plasmonics and especially electron energy loss spectroscopy the first boundary element method based on evaluation of the potentials and a collocation method was done in [78]. Here a solution of the Helmholtz equation in terms of the retarded Green function is given by

$$(\boldsymbol{\nabla}^2 + k_j^2)\mathrm{G}_j(\mathbf{r},\mathbf{r}',\omega) = -4\pi\delta(\mathbf{r}-\mathbf{r}'),\ \mathrm{G}(\mathbf{r},\mathbf{r}',\omega) = \frac{e^{ik_j|\mathbf{r}-\mathbf{r}'|}}{|\mathbf{r}-\mathbf{r}'|}, \tag{2.33}$$

where $k_j = k_0\sqrt{\epsilon_j(\omega)}$ is the wavenumber in medium j. For the vector potentials the partial differential equations with source terms ρ and $\mathbf{J}$ read

$$(\boldsymbol{\nabla}^2 + k_j^2)\Phi_j(\mathbf{r},\omega) = -4\pi\rho(\mathbf{r},\omega), \tag{2.34a}$$

$$(\boldsymbol{\nabla}^2 + k_j^2)\mathbf{A}_j(\mathbf{r},\omega) = -4\pi\mathbf{J}(\mathbf{r},\omega). \tag{2.34b}$$

The external sources can be evaluated by means of the retarded Green function as $\Phi_j^{ext}(\mathbf{r},\omega) = \int dr'\mathrm{G}(\mathbf{r},\mathbf{r}',\omega)\rho_j^{ext}(\mathbf{r}',\omega)$ and $\mathbf{A}_j^{ext}(\mathbf{r},\omega) = \int dr'\mathrm{G}(\mathbf{r},\mathbf{r}',\omega)\mathbf{J}_j^{ext}(\mathbf{r}',\omega)$ and

the solution of the Helmholtz equation for the vector potentials in each medium j can then be written in the ad hoc form as

$$\Phi_j(\mathbf{r},\omega) = \Phi_j^{ext}(\mathbf{r},\omega) + \oint_{\partial\Omega} d\mathbf{s}\mathrm{G}(\mathbf{r},\mathbf{r}',\omega)\rho_j(\mathbf{s},\omega), \tag{2.35a}$$

$$\mathbf{A}_j(\mathbf{r},\omega) = \mathbf{A}_j^{ext}(\mathbf{r},\omega) + \oint_{\partial\Omega} d\mathbf{s}\mathrm{G}(\mathbf{r},\mathbf{r}',\omega)\cdot\mathbf{h}_j(\mathbf{s},\omega), \tag{2.35b}$$

where the integral goes over the boundary between two adjacent materials (see Fig. 2.7) and $\rho(\mathbf{s},\omega)$ and $\mathbf{h}(\mathbf{s},\omega)$ are surface charges and currents, respectively. To link the solutions inside different media the boundary conditions - i.e. continuous tangential electric field and continuous normal electric displacement across the boundary, as well as continuous tangential magnetic field strength and continuous normal magnetic field across the boundary - are applied and one obtains a set of eight integral equations [78].

For the numerical implementation one discretizes the boundary charge and current distribution on a surface mesh and obtains from the integral equations and the boundary conditions a matrix representation [78, 18], which can be solved through matrix inversion for the surface charges and currents, and with Eq. (2.35a) and (2.35b) for the scalar and vector potentials everywhere else.

There exist several implementations of boundary element methods, e.g. see [79] for a Galerkin method implementation or [18] for a collocation method. A comparison for spheres with varying diameter between the implementation in [18] and a Galerkin method based on [79] is shown in Fig. 2.8. Both methods agree well with the analytic Mie solution over a broad energy range. Substrate effects can also be incorporated by a redefinition of the retarded Green function as was done in [80]. The energy loss suffered by a swift electron in vicinity of a dielectric medium was implemented in [81]. This approach works for non penetrating and penetrating electron trajectories as well as for substrates. Excellent agreement between simulations and experiment has been demonstrated, see e.g. [17, 82], or for a comparison with the analytic solution of a sphere and the collocation approach, Fig. 2.9.

Computation of eigenmodes via boundary element method

In the quasi-static case the computation of eigenmodes within the boundary element method is straight forward. One uses the discretized form of Eq. (2.19) at the boundary, which leads to a $n \times n$ matrix, with n being the number of discretized surface elements. For the computation of the eigenmodes one searches for the left and right eigenvectors of this matrix with a standard eigenvalue solver and then othogonalizes them with Eq. (2.20), i.e one redefines the left eigenmodes as $\hat{\boldsymbol{\sigma}} = (\boldsymbol{\sigma}\tilde{\boldsymbol{\sigma}})^{-1}\boldsymbol{\sigma}$. The orthogonalization is needed for degenerate eigenmodes. An implementation of this procedure can be found in [18].

The retarded eigenmodes are evaluated in the boundary element formalism by use of the Sigma matrix Σ, which is defined in [78]. Either one searches for the complex poles of the matrix with an iterative technique, i.e. one searches for $\det[\Sigma(\omega)] = 0$ and obtains the quasinormal modes, or one computes the eigenvectors at a fixed real frequency,

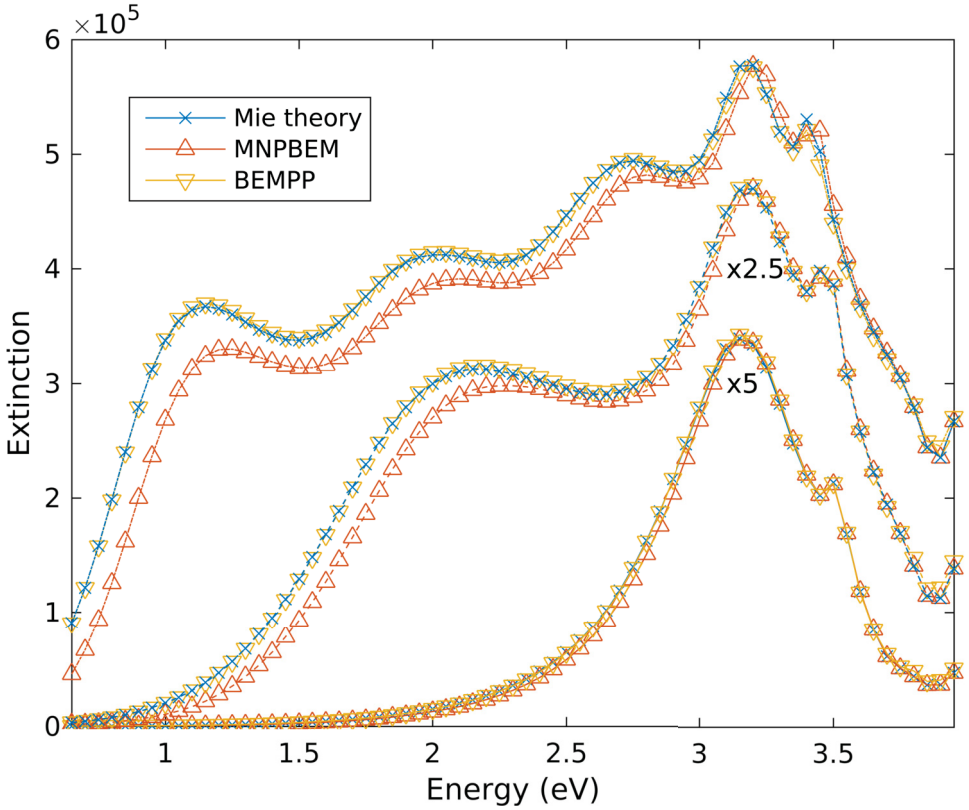

Figure 2.8: Comparison of analytic Mie theory, MNPBEM toolbox [81] and a Galerkin discretization based on Stratton-Chu formalism [79] for sphere with varying diameter: solid line 100 nm, dashed line 200 nm, dot-dashed 400 nm. Both methods agree well with the analytic result. For lower energies and larger diameter, the Galerkin method is more accurate.

obtaining constant flux states. An iterative procedure of the evaluation of quasinormal modes by a boundary element method can be found in [52], where also a normalization procedure is given (this approach works best for a single mode approximation).

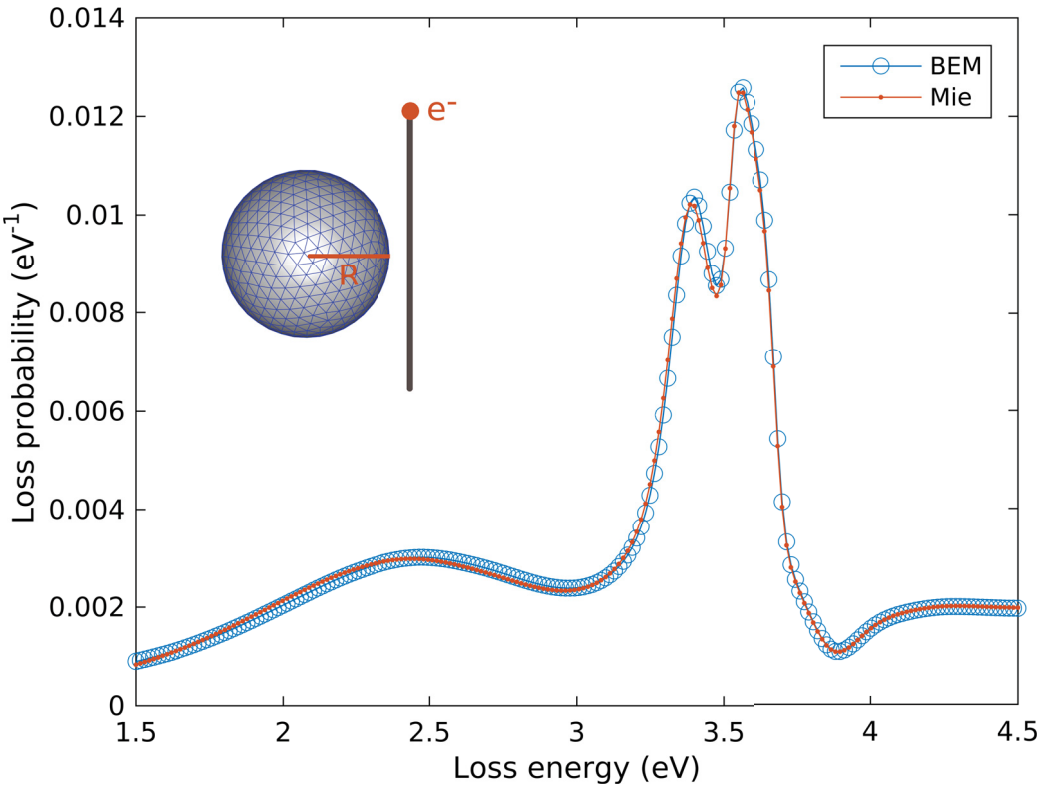

Figure 2.9: Comparison of analytic Mie theory with MNPBEM toolbox [81] for sphere with R=75 nm, a discretization of approximately 500 boundary elements and dielectric function of silver taken from experimental values [16]. The electron beam is situated 10 nm away from the particle boundary.

3 Tomography of plasmons

In tomography one usually tries to recover a two or three-dimensional function (e.g. image, density distribution) from a series of selected projections. The projections are usually some kind of indirect measurements of the desired function, e.g. an integration of a function along a trajectory.

The seminal paper is by Radon and dates back to 1917 [83], although its breakthrough came with the invention of x-ray computed tomography by Hounsfield, who received a Nobel prize for it in 1972.

The field of tomography has its largest application in the disciplines of medicine, for imaging purposes - by creating visual representations of inner parts of the body. Techniques such as x-ray tomography, magnetic resonance imaging, or optical coherence tomography are used. There exist also numerous non-medical applications inspired by tomography, e.g. geophysical applications or electron tomography for volume imaging of different materials with nanometer resolution.

In a less strict sense tomography deals with the problem of how to obtain information of an object or a function from a collection of indirect measurements. In a mathematical sense this can be brought into the form

$$Af = y, \tag{3.1}$$

where A is a measurement operator, f is the desired function and y is the measurement or projection. Usually the desired information f is obtained by solving an inverse problem, that is in the best case - if the problem is well posed and when it is computationally affordable - by inverting A and applying it to y. Unfortunately a lot of inverse problems are ill-posed - i.e. no solution, no unique solution or no linear dependence on initial conditions of the solution exists - in nature and/or demand a lot of computational power.

There are two main solution procedures in the field of tomography: algebraic reconstruction and filtered back projection. In algebraic reconstruction essentially a matrix inversion is performed or - if the size of the matrix is too large - iterative techniques are used to solve the discretized matrix form of Eq. (3.1) and find f. Filtered back projection can be applied when A is a Radon transformation. Then a Fourier transform of the projections y can be associated with a Fourier transform of f and one can solve f essentially by Fourier and inverse Fourier transforms.

To achieve better convergence or a solution for ill-posed inverse problems at all (because of the nature of the problem, measurement errors, linear dependent measurements, nonlinear problems,...), one can use additional assumptions like sparsity in a given basis (compressed sensing) or smoothness of the solution. Applying additional assumptions is also referred to as regularization.

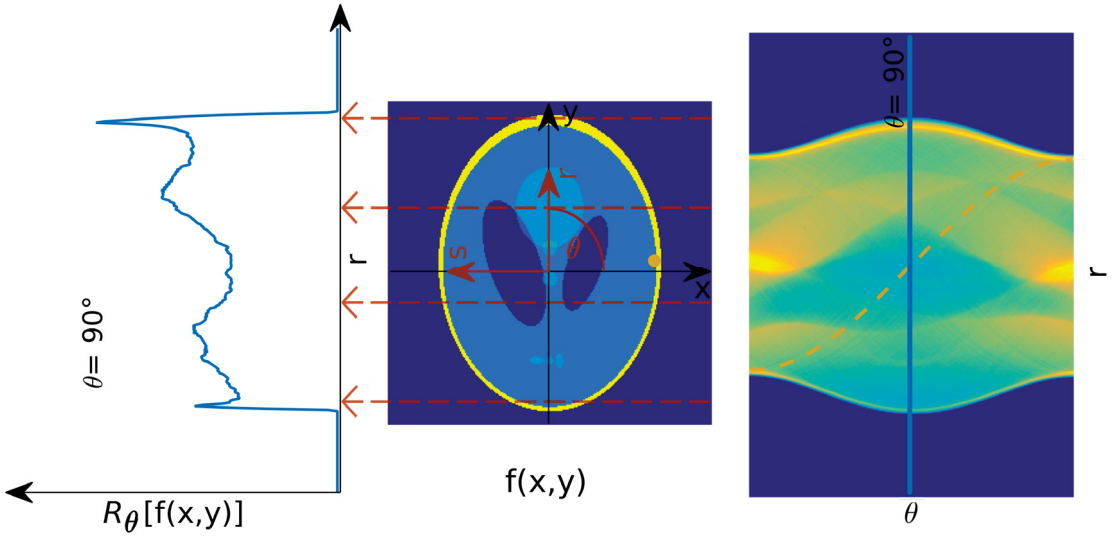

Figure 3.1: Concept of Radon transformation. (Middle figure) The famous Shepp-Logan phantom [84] is used as function $f(x, y)$ to show the basic principle. Dashed lines correspond to integration trajectories along the s-direction (e..g parallel light beams) for some values of r. (Left figure) Corresponding Radon transformation for $\theta = 90°$. (Right figure) Sinogram of phantom for $\theta = 0 : 0.5 : 179.5$. Orange dashed line corresponds to sinogram of orange dot in phantom. Blue line is associated with Radon transformation at 90° (same as left figure).

3.1 Radon transformation

The most common form of tomography deals with the projections obtained from a Radon transformation [83]. It is at heart of modern medical imaging techniques, such as x-ray tomography or positron emission tomography and other parallel and fan beam tomography schemes. The mutual basis of all of them is that the probe penetrates the specimen via a straight line for varying angles and accumulates the desired information (density, magnetic field...). More precisely, a function is projected by an integral over a straight trajectory on a line for different angles, see Fig. 3.1. The transformation can be written as

$$R_\theta(r) = \int_{-\infty}^{\infty} f(r, s)ds, \tag{3.2}$$

where r, s are given in Fig. 3.1 and are obtained by a rotation of the principal axis x and y by an angle θ

$$\begin{bmatrix} r \\ s \end{bmatrix} = \begin{bmatrix} \cos\theta & \sin\theta \\ -\sin\theta & \cos\theta \end{bmatrix} \begin{bmatrix} x \\ y \end{bmatrix}. \tag{3.3}$$

In other words, the Radon transformation projects a two dimensional function $f(x, y)$ onto a line r for a certain direction defined by θ. E.g. a Radon transformation for $\theta = 90°$

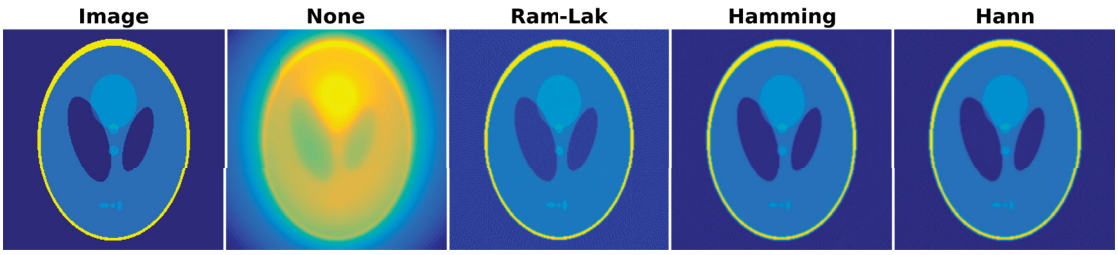

Figure 3.2: Reconstruction of phantom image (same as Fig. 3.1) by an inverse Radon transform R^{-1} from sinogram with $\theta = 0 : 1 : 179$ and different filter methods. the worst results are obtained by unfiltered back-projection, while Hann and Hanning are a little bit better than Ram-Lak. Images are computed with Matlab routines for inverse Radon transforms.

is a projection of $f(x, y)$ onto the y-axis (Fig.3.1). By applying the Radon transformation to a point for angles from 0 to π as in Fig. 3.1 (see orange point and orange dashed line) one obtains a sine function. Therefore a dataset with projections of a function for different angles is called a sinogram. To obtain the largest possible information content, it usually suffices because of symmetry reasons to vary θ from 0 to π. For generalizations of the Radon transform, such as involving non straight trajectories, see e.g. [85].

The Radon transformation can be linked to the Fourier transformation of $f(x, y)$ by a Fourier transform of $R_\theta(r)$ and using the variable transformation of Eq. (3.3), as [86]

$$\tilde{R}_\theta(k) = \int_{-\infty}^{\infty} e^{-ikr} R_\theta(r) dr = \int_{-\infty}^{\infty} e^{-i(k\cos\theta x + k\sin\theta y)} f(x, y) dx dy = F(k\cos\theta, k\sin\theta), \tag{3.4}$$

which is also called Fourier-slice theorem and states that the Fourier transformed projections of f are the polar form of the Fourier transformed function f, which can be used for reconstruction of f.

3.1.1 Inverse Solution

As already stated the field of tomography deals with inverse solutions. In contrast to forward solutions, where one usually knows an initial state and wants to derive a final state, in inverse problems one attempts to find the initial state or initial function from final data, like projections.

The nice thing about a Radon transformation is that an inverse solution exists and various methods are developed to gather it. There are two main groups: Inverse Fourier transforms and algebraic reconstruction techniques.

Filtered back projection

The most simple approach to acquire an image from projections is to back project at each angle. One then obtains a blurred image (see Fig. 3.2). For an accurate inversion

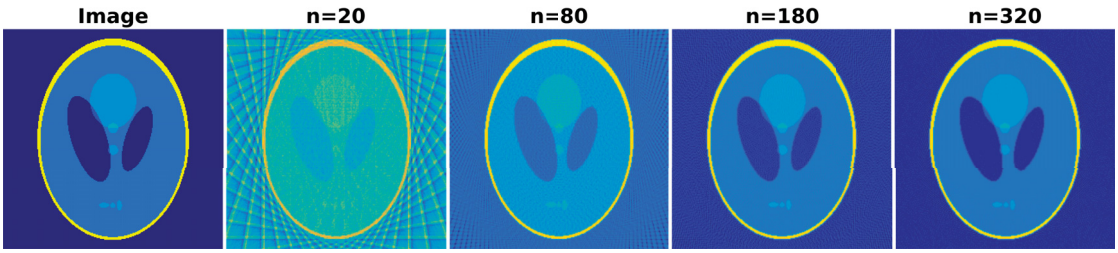

Figure 3.3: Reconstruction of phantom image (same as Fig. 3.1) by an inverse Radon transformation R^{-1} from sinogram using different numbers n of angles between 0:180 degrees. As a filter function a conventional Ram-Lak filter is used (see also Fig. 3.2).

one has to account for the blurring through use of filter functions in the back projection process. The filtered back projection method is computationally fast, because it only involves Fourier transformations, and it is therefore the standard algorithm in computed tomography.

Filtered back projection uses the fact that a Radon transformation is linked to a Fourier transformation. The inverse Fourier transformation of $f(x, y)$ can be written as

$$f(x,y) = \frac{1}{(2\pi)^2} \int_{-\infty}^{\infty} e^{i(k_x x + k_y y)} F(k_x, k_y) dk_x dk_y. \tag{3.5}$$

By switching to polar coordinates and changing the integral limits from $\theta = (0, 2\pi)$ and $k = (0, \infty)$ to $\theta = (0, \pi)$ and $k = (-\infty, \infty)$ one obtains a formula for filtered back-projection

$$f(x,y) = \frac{1}{(2\pi)^2} \int_{0}^{\pi} \int_{-\infty}^{\infty} e^{ik(x\cos\theta + y\sin\theta)} |k| F(k,\theta) dk d\theta, \tag{3.6}$$

where $F(k, \theta) = \tilde{R}_\theta(k)$ and $|k|$ is working as a filter function to account for the effect of blurring in unfiltered back-projection. One can use better filter functions, e.g. one can limit the bandwidth, and there are existing plenty of different filter functions, each with its advantages and disadvantages. For more on filters see e.g. [87, 88]. In Fig. 3.2, we show the inverse Radon transformation for different popular filter functions. One finds that using a filter function is a crucial point in obtaining accurate results. A second possibility to get better results is shown in Fig. 3.3, where the inverse Radon transformation is shown for a varying number of projections.

Algebraic reconstruction technique

To solve the inverse problem one can discretize the image into a number of pixels and for each projection or measurement one gets a linear equation where the pixels are the unknown as depicted in Fig. 3.4. In principle then one only needs to solve the linear system of equations by matrix inversion. For very small problems this method is feasible, but as images and therefore the number of pixels grow, iterative techniques are used.

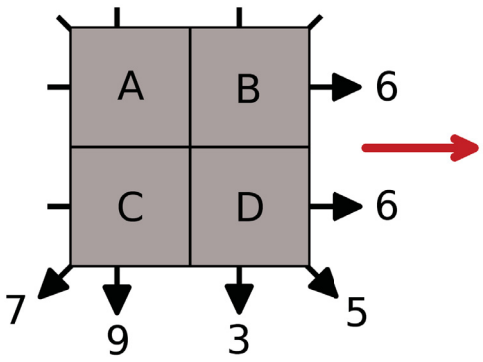

$$\begin{pmatrix} 1 & 1 & 0 & 0 \\ 1 & 0 & 1 & 0 \\ 1 & 0 & 0 & 1 \\ 0 & 1 & 1 & 0 \\ 0 & 1 & 0 & 1 \\ 0 & 0 & 1 & 1 \end{pmatrix} \begin{pmatrix} A \\ B \\ C \\ D \end{pmatrix} = \begin{pmatrix} 6 \\ 9 \\ 5 \\ 7 \\ 3 \\ 6 \end{pmatrix}$$

Figure 3.4: The projection values (arrows) of pixels (A, B, C, D) are solutions of a matrix equation formed by the coefficients (pixels) and a measurement matrix, accounting for each projection. Here, the solution can be found by simple matrix inversion and gives A=4, B=2, C=5 and D=1.

There are several variants: Algebraic reconstruction technique (ART), simultaneous iterative reconstruction technique (SIRT) and iterative total least squares technique (ITLS) [88].

The first reconstruction algorithm used in computed tomography was algebraic reconstruction and therefore we will shortly introduce it here. It consist of three steps [86, 89]:

1. Make an initial guess of the image
2. Compute projections based on that guess
3. Refine the guess based on the weighted (by g) difference between the desired (real) projections and the actual (calculated) projections p:

$$p^{i+1} = p^i + g(desired - actual).$$

When a stopping criteria - maximum difference between *real* and *desired* projections - is reached, the iteration stops and gives a final result, which is the desired image.

Iterative methods are slow compared to filtered back-projection, but it is relatively easy to incorporate prior knowledge of the problem and there is no need of equidistant aligned angles between 0 and π to obtain good results.

3.2 General solution of inverse problems

As already stated one can use the matrix form of the Radon transformation to obtain the inverse solution. Inverse problems, where we know the operator or measurement

matrix A can be tackled in a similar way. In principle one can attempt to minimize

$$\min_x ||Ax - b||_{l_2} < \epsilon, \tag{3.7}$$

where $||Ax - b||_{l_2}$ is the so called cost function and ϵ is a stopping value. One starts with an initial guess and iterates x until the stopping criteria is reached. The change of x for each iteration is usually derived by using the gradient of the cost function. The simplest method is to search along the direction of the gradient, which is called steepest descent. This method often has to be improved - because of slow convergence - by the conjugate gradient method [90], which takes into account and tries to hinder previous search directions. More involved schemes - usually termed as Newton or quasi-Newton methods - also use the second derivative, or approximations of it, to find search direction and step size [91].

Although this problem always yields to a solution, often the solution is not unique and one has to take into account some constraints, which are added to the cost function in order to find a meaningful solution vector x.

3.3 Compressed sensing

One rather new mathematical tool - the first paper was written in 2004 [92] - that is used nowadays in a lot of tomography applications is compressed sensing or compressive sampling. It is used, to name just a few applications, in MRI to increase image reconstruction speed and reduce amount of required data [93], for geophysical problems [94], for single pixel cameras [95], for quantum state [96] and electron [97] tomography, and in general for inverse problems. For introduction and review see e.g. [98, 99].

The basic principle relies on a sampling paradigm that goes beyond the Nyquist-Shanon theorem - the frequency information can only be obtained up to the sampling frequency divided by two - which uses additional information about the signal for recovery: (i) sparsity of the desired signal and (ii) incoherence of the measurement basis with the basis where the signal is sparse.

3.3.1 Sparsity

A signal or some information is sparse in a certain basis, when it can be represented there with just a few number of coefficients unequal to zero. In fact, many natural signals can be represented sparse (almost) without information loss in a proper basis, e.g. a Dirac delta in the time domain is sparse or the size of images can be reduced dramatically by representing them in a wavelet basis. For example see Fig. 3.5, where only three coefficients contain almost all information about a time signal: When only the three largest coefficients are taken for a Fourier transformation, we get essentially the same Fourier coefficients.

In mathematical terms a signal can be represented in a certain basis $\Psi = [\psi_1, \psi_2, ..., \psi_n]$ as

$$f(t) = \sum_i^n c_i \psi_i(t), \tag{3.8}$$

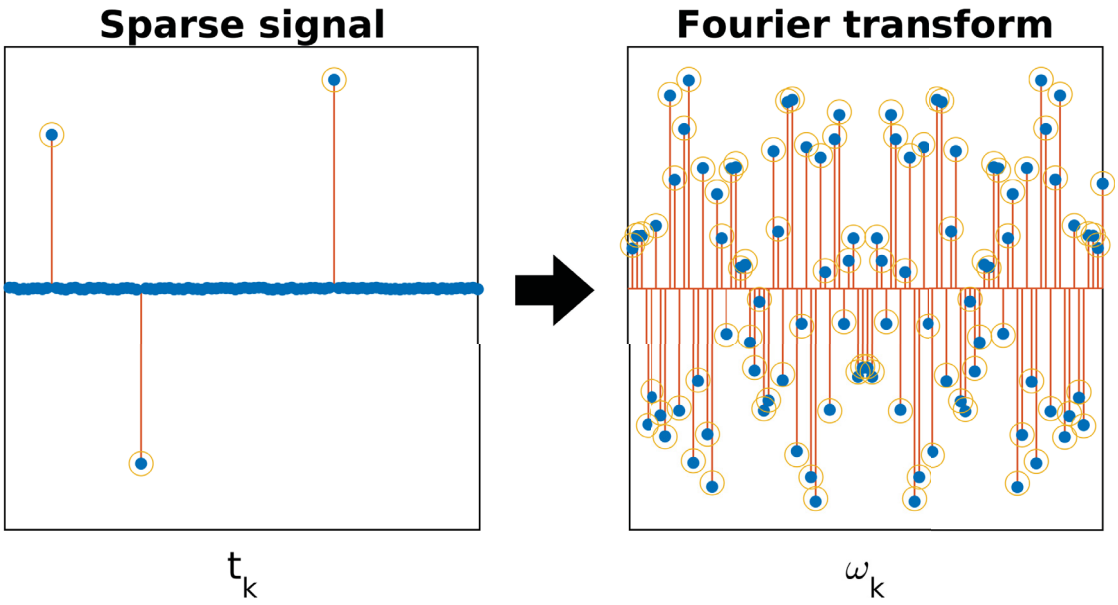

Figure 3.5: Principle of sparsity and incoherence. (Left) A sparse signal in the time domain has three spikes. All other coefficients t_k are approximately zero. (Right) Real part of the discrete Fourier transformation of the signal in left figure. The signal is spread out and all coefficients are unequal to zero and needed to describe the signal. The time-frequency pair is maximal incoherent. Orange circles denote the Fourier transformation of the three largest coefficients only, implying that only this coefficients contain almost all information about the signal.

where c is the coefficient vector of f in basis Ψ and $c_i = \langle f, \psi_i \rangle$. Then the signal is sparse in basis Ψ, when only a small number of coefficients c_i suffices to describe the signal without much information loss. In other words, all $c_i \approx 0$ can be discarded, when the signal is sparse in basis Ψ. This is also reflected by the following: Set c_s the coefficients of the sparse approximation and $f_s = \psi_s c_s$. Then because of the orthonormality of Ψ and from Parseval's identity we arrive at $\|f - f_s\|_{l_2} = \|c - c_s\|_{l_2}$. So, if the error between c and c_s is small, the error between the solution and the approximation of the solution, described only by s basis elements and coefficients, is small and the signal is described well by the sparse approximation (if c_s are the only non-zero entries, the error is zero).

This is the principle which data compression techniques, like JPEG-2000, follow: compute the coefficients of an image in a sparse basis and discard the small coefficients, for an example see e.g. [98, 100]. However compressed sensing goes well beyond that because the sensing itself can be compressed, provided that one uses a largely incoherent measurement basis for sampling.

3.3.2 Incoherent sampling

Incoherence of the measurement basis means that the basis of the measurement is largely incoherent with the sparse basis of the signal. Put differently, the signal should have an extremely dense representation in the measurement basis, such as a Dirac delta distribution in the time domain is spread out in the frequency domain (see Fig. 3.5). Then only a small number of random measurements with dense basis elements already contains enough information to reconstruct the desired signal.

Suppose we have two orthonormal bases (although this restriction is not essential): Ψ and Φ. The first basis represents the signal sparse and the second basis is used for sensing (the measurement basis). Then, by definition [98], the coherence between Ψ and Φ is

$$\mu(\Psi, \Phi) = \sqrt{n} \max_{1 \leq k,j \leq n} |\langle \psi_k, \phi_j \rangle|, \tag{3.9}$$

where n is the number of basis elements. Put differently, coherence measures the largest correlation between all elements of Ψ and Φ and $\mu(\Phi, \Phi) \in [1, \sqrt{n}]$, where 1 expresses minimum coherence and $\sqrt{n}$ maximum coherence. For compressed sensing we want low-coherence pairs.

An example of a basis pair with minimum coherence or maximal incoherence, that is $\mu(\Psi, \Phi) = 1$, is the canonical or spike basis $\psi_k(t) = \delta(t - k)$ and the Fourier basis $\phi_j(t) = n^{-1/2} e^{i2\pi jt/n}$. Here, Ψ corresponds to the classical sampling scheme in space or time. The incoherence of this basis pair is depicted in Fig. 3.5, where a signal is sparse in the spike basis is shown in the Fourier basis, where it is spread out. In a similar vein, spikes and sinusoids - even in three dimensions - are minimal coherent. Other examples are noiselets and Haar wavelets, where $\mu = \sqrt{2}$. For random matrices [101], e.g. random binary entries in a matrix, we get a special result: $\mu = \sqrt{2 \log n}$ for any second basis. In other words: random matrices are largely incoherent with any fixed basis and are therefore a great promise as a sensing basis [95] for sparse signals.

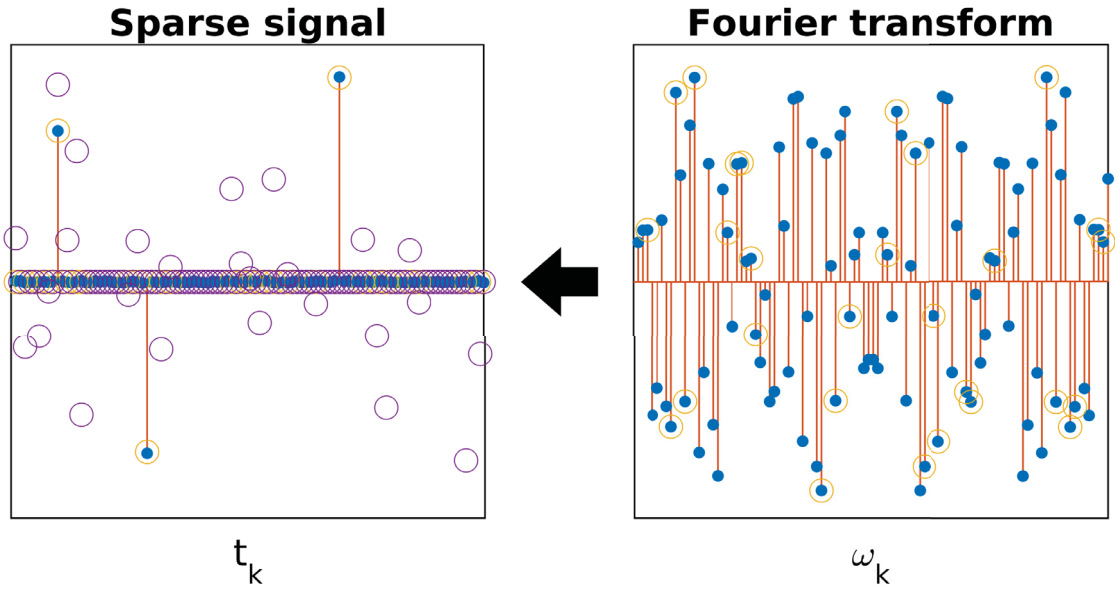

Figure 3.6: Reconstruction of the sample shown in Fig. 3.5. Only one third of the Fourier components are used as measurement data (orange circles in right figure) to solve the inverse problem, which results in a highly under-determined problem. A simple least square minimization yields the purple circles in left figure. The solution of compressed sensing is shown by the orange circles in left figure and agrees almost perfectly with the exact solution shown as blue dots.

3.3.3 Reconstruction

Suppose we have a sparse signal with a sparsifying basis Ψ and a sensing basis Φ, which is largely incoherent with the sparse basis. We measure f, which is the desired information consisting of n entries, e.g. the pixel of an image. Then the collected data takes the form $y_m = \langle f, \psi_m \rangle$, where m is the number of measurements. We have

$$y = Af, \tag{3.10}$$

where A is an $m \times n$ matrix and f and y are $n \times 1$ and $m \times 1$, respectively. If $m > n$ and the matrix A has full rank we are done and can solve either by matrix inversion or with least square techniques. For $m < n$ and ill-posed problems (if a solution exists) we get in principle infinitely many candidate solutions $\tilde{f}$, for which $y = A\tilde{f}$.

How can we use the properties of sparseness and incoherence, or, in other words, which constraints do we have to set on the cost function in order to find the desired signal and can we guarantee that, if we have found a solution by these constraints, the solution is f?

A first guess to implement the constraint of a sparse basis would be to search for a

vector $\tilde{x}$ with $\tilde{f} = \Psi\tilde{x}$ and

$$\min_{\tilde{x}} \|\tilde{x}\|_{l_0} \text{ subject to } y = A\Psi\tilde{x}, \tag{3.11}$$

where $\|.\|_{l_0} = \sum x_i^0$, $0^0 = 0$ checks whether a coefficient is zero or not. Eq. (3.11) searches for a solution $\tilde{x}$ with as little as possible coefficients x_i unequal to zero. This idea has two drawbacks: It does not work for approximately sparse signals, i.e. $c_i \approx 0$ and it can be shown, that it is NP-hard, which means that it is computationally not feasible. Luckily, one can substitute the l_0-norm by the l_1-norm in Eq. (3.11). Then the c_i's can be approximately sparse and the problem can be solved by convex optimization [98], which has the advantage that algorithms for convex optimization exist. Further, if we have noisy data, a robust compressed sensing scheme can be formulated and reads

$$\min_{\tilde{x}} \|\tilde{x}\|_{l_1} \text{ subject to } \|A\Psi\tilde{x} - y\|_{l_2} \leq \epsilon, \tag{3.12}$$

where ϵ is used to define the amount of noise in the data y. Eq. (3.12) can be solved efficiently and is again a convex optimization problem (a second-order cone program) and was first stated in [102]. A Matlab implementation of this and similar compressed sensing problems is available at [103].

If Eq. (3.11) and (3.12) find a sparse solution $\tilde{x}$, do we know that it is the sparse representation of f? It can be shown, that the answer is yes. Put differently, if we find a solution of Eq. (3.11), which is S-sparse, with S the number of non-vanishing coefficients, from m measurements and

$$m \leq C \cdot \mu^2(\Psi, \Phi) \cdot S \cdot \log n, \tag{3.13}$$

holds for some positive constant C, then the solution $\tilde{x}$ is equal to x with overwhelming probability. Eq. (3.13) states that, when $\mu(\Psi, \Phi)$ is close to one, the number of measurements taken has to be in the order of $S \log n$ instead of n. Further, any set of m measurements guarantees a solution. In Fig. 3.6 we show a reconstruction of a sparse signal in the time domain with 101 coefficients (three of them are around zero) and the discrete Fourier transform of the signal (also 101 coefficients). We take approximately a third (31) of the Fourier coefficients as measurement data and try to reconstruct with them - by solving an inverse problem - the time signal. With a simple least square algorithm (standard Matlab routine) this is impossible (highly under-determined system with $m < n$), but compressed sensing (performed with the code in [103]) shows exact recovery for the ill-posed inverse problem.

3.4 Tomography applied to plasmon imaging

First of all, for plasmon tomography one needs an imaging tool, which is capable of exciting surface plasmons. Here, several electromagnetic field sources to excite a surface plasmon come into mind, especially excitation by molecules (oscillating dipole), lasers (plane wave excitation) and fast electron beams (electron energy loss spectroscopy). Second, one needs spatial information at the length scale of surface plasmons, which is in

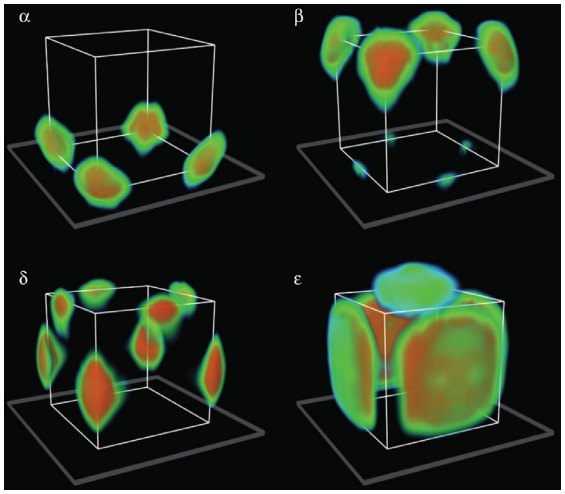

Figure 3.7: Plasmon tomography using electron energy loss spectroscopy: A silver nanocube is studied via a tomography scheme experimentally by means of non-negative-matrix factorization and compressed sensing. Plasmon resonances are imaged in the spatial domain. Adapted from [31].

the nanometer regime. With this second restriction in mind, only a few techniques are in principle suitable to extract three dimensional plasmon information. One of them is near field microscopy [104, 105], where NSOM data is used for the inverse scattering problem, leading to an ill-posed reconstruction problem, which can be solved by means of singular value decomposition. Another promising approach deals with electron energy loss spectroscopy, where two different types of information can be gathered: the scattering spectra from electron beam excitation - cathodoluminescence spectroscopy [23], and the energy loss spectra. Recently, for cathodoluminescence spectroscopy data, a tomography scheme has been used to reconstruct optical properties [106]. Other investigations are going towards electron energy loss tomography [31, 107, 57, 108]. Here, we will discuss them in more detail.

For the small particle approximation, i.e. particle small compared to the resonance wavelength, a tomography scheme based on the quasi-static approximation, i.e. the Poisson equation, was developed theoretically in [107] and studied experimentally for a silver nanocube in [31] (see Fig. 3.7). A model for the reconstruction of surface charges was also reported in [107] and investigated in detail in [108].

For particles with dimensions comparable to the resonance wavelength retardation effects come into play and the situation is more delicate. Here one either refrains from solving an inverse problem directly for the electromagnetic fields and uses the tomographically reconstructed particle surface as input in electromagnetic simulations [82], or uses a more involved reconstruction scheme, which is based on compressed sensing optimization and an eigenmode decomposition of the electromagnetic field propagator in presence of a dielectric body [57].

3.4.1 Quasi-static regime

In the quasi-static regime the eigenpotential expansion of Eq. (2.23)

$$\Gamma_{EELS}(\mathbf{R}_0,\omega) = -\frac{-e^2}{\pi\hbar v^2\epsilon}\sum_k \mathrm{Im}\left[c_k(\omega)\right]\left|\int_{-\infty}^{\infty} e^{iqz}\phi_k(\mathbf{R}_0,z)dz\right|^2$$

leads under some assumptions to a Radon transformation.

First of all, one has to assume that the electron energy loss at a certain resonance frequency ω is dominated by one mode, hence we neglect the sum in Eq. (2.23). It can be checked in the electron energy loss spectra if this assumption is true, which is the case for a lot of particle geometries.

Second, the exponential factor in Eq. (2.23) refrains from reformulating electron energy loss spectroscopy in terms of a simple Radon transformation. Fortunately, this factor can be neglected provided the sign of the eigenmode potential does not change at the interaction length along the electron path.[1] In principle the exponential factor could also be incorporated in the reconstruction process by using diffraction tomography [109].

Third, Eq. (2.23) applies only to electron paths passing by the particle. For electrons penetrating the particle a more complicated scheme, relying also on the Radon transformation can be used [107].

By applying these assumptions and restrictions we are left with a simple form of the reconstruction process - a Radon transform, which is easily implemented and well understood. Neglecting constant factors and at a certain resonance frequency the energy loss can be written as

$$\Gamma_{EELS}(\mathbf{R}_0) \propto \left|\int_{-\infty}^{\infty}\phi(\mathbf{R}_0,z)\right|^2 = R_\theta[\phi(\mathbf{r})]^2, \tag{3.14}$$

stating, that the electron energy loss is connected with the eigenmode potential of plasmonic particles by a Radon transformation squared. So we loose the sign of the potential due to the square of a Radon transformation. Therefore one has to carefully choose the reconstruction plane in a way that the potential has always the same sign thereon.

To lift some of the above restrictions and assumptions, one may refrain from a simple Radon transformation and solve an inverse problem based on more complicated models of the electron energy loss. A reconstruction based on the source of the eigenmode potential, i.e. surface charges on the particle boundary, was reported in [107], where Eq. (2.23) was modified by inserting Eq. (2.21). Then connecting the free Green function showing up in Eq. (2.21) with the electron beam one is left with integrals over the particle boundary only and obtains a model for the surface charge distribution on the boundary, which can be used to introduce a cost function and minimize it according to

$$\min_{\boldsymbol{\sigma}(\mathbf{s})} \left\|\Gamma^{\mathbf{R}_0,\theta}_{\mathrm{EELS}} - \Gamma^{\mathbf{R}_0,\theta}_{\mathrm{MODEL}}[\boldsymbol{\sigma}(\mathbf{s})]\right\|_{l_2}. \tag{3.15}$$

[1] Then the imaginary part in the integral approximately cancels because of symmetry reasons, and the lasting cosine function is approximately equal to one due to the reason that $qz = w/vz << 1$ at the interaction regime, which is restricted to the evanescent decaying eigenmode potential(see e.g. Fig. 2.5.

It is advantageous over a Radon transformation reconstruction, because penetrating electron beams and the sign problem are not apparent. As the inverse problem does not give a unique solution, it relies on an initial guess $\sigma_0(\mathbf{s})$ and therefore one should carefully choose an initial guess with proper symmetry. An experimental realization for silver bipyramids was shown in [108]. The authors revealed the three dimensional profile of plasmon modes and showed substrate-induced mode degeneracy breaking. They added to the cost function in Eq. (3.15) a regularization term in order to promote parsimonious solutions.

3.4.2 Full Maxwell equations

A reconstruction scheme for particles, where retardation effects come into play - i.e. particles with at least one dimension greater than 50 to 100 nm, has to take into account the full Maxwell equations. Then we do not obtain a scalar quantity from the reconstruction, as in the quasi-static case, but vector valued solutions. Therefore things get more complicated.

The electron energy loss can be written for the full Maxwell equations as (see also Eq. (2.15))

$$\Gamma_{EELS}(\mathbf{R}_0,\omega) = -\frac{4e}{\hbar}\int_{-\infty}^{\infty} dzdz' \ \mathrm{Im}\left[e^{iqz}\mathbf{v}\cdot\mathbf{G}(\mathbf{r},\mathbf{r}',\omega)\cdot\mathbf{v}e^{-iqz'}\right]. \tag{3.16}$$

The response of the particle due to applied electric fields is governed in the dyadic Green tensor $\mathbf{G}$. So we want to reconstruct this quantity from the energy loss data. In order to solve the inverse problem the Green tensor can be decomposed into a set of modes as shown in subsection 2.2.5. Then an approximation of the dyadic Green tensor reads

$$\mathbf{G}(\mathbf{r},\mathbf{r}',\omega) \approx \sum_k C_k \mathbf{E}_k(\mathbf{r}) \otimes \mathbf{E}_k(\mathbf{r}'), \tag{3.17}$$

where C_k control the contribution of each mode. It is motivated by the fact that $\mathbf{G}(\mathbf{r},\mathbf{r}') = \mathbf{G}^{\intercal}(\mathbf{r}',\mathbf{r})$ is a complex symmetric operator. A singular value decomposition of the associated complex symmetric matrix leads to a decomposition of this type. Further, the same decomposition is used, when the Green tensor is decomposed into quasinormal modes, see Eq. (2.28). When inserting Eq. (3.17) into (3.16) one ends up with a model for the electron energy loss probability, which depends only on the coefficients of the decomposition and reads at a certain energy ω

$$\Gamma^{\mathbf{R}_{\hat{\mathbf{v}}}}_{\mathrm{MODEL}}[C_k] = \sum_k \ \mathrm{Im}\left[C_k A^+(\mathbf{R}_{\hat{\mathbf{v}}})A^-(\mathbf{R}_{\hat{\mathbf{v}}})\right], \tag{3.18}$$

where $A^{\pm}_k(\mathbf{R}_{\hat{\mathbf{v}}}) = \int_{-\infty}^{\infty} e^{\pm iqz}\hat{\mathbf{v}}\cdot\mathbf{E}_k(\mathbf{R}_0+\hat{\mathbf{v}}z)dz$. These integrals can be tackled in a way that only integrals over the surface of the particle have to be taken into account. Eq. (3.18) leads to a linear system of equations with k unknowns and can be solved by optimizing

$$\min_{C_k} \ \left\|\Gamma^{\mathbf{R}_{\hat{\mathbf{v}}}}_{\mathrm{EELS}} - \Gamma^{\mathbf{R}_{\hat{\mathbf{v}}}}_{\mathrm{MODEL}}[C_k]\right\|_{l_2} \tag{3.19}$$

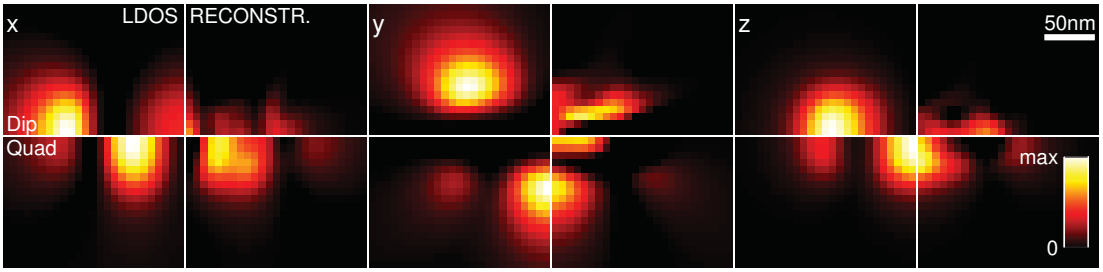

Figure 3.8: Least square reconstruction of the photonic local density of states of a rectangular nanoparticle with dimensions $200 \times 65 \times 30\text{nm}^3$ and a dielectric function for gold from the Drude model. Shown are the dipolar (top panels) and quadrupolar (bottom panels) modes of the plasmonic structure and the true local density of states compared to the density of states evaluated from the reconstructed Green tensor via least square optimization. As measurement data a set of rotated electron energy loss maps was used. As reconstruction basis bi-orthogonal eigenmodes, as described in subsection 2.2.5, where used. For further details, see [57].

for different impact parameters $\mathbf{R}_{\hat{\mathbf{v}}}$ with orientation of the electron trajectory $\hat{\mathbf{v}}$.

In principle, one could expand the eigenmodes $\mathbf{E}_k$ again into a set of basis vector functions, which fulfill Maxwell's equations in free space, such as vector spherical harmonics. A proper framework for non-smooth particles would be to use a multiple multipole expansion, as is depicted in subsection 2.3.1. Such a decomposition would be nice, because one could use quite general basis functions to expand the solution and there would be no need for additional assumptions, as is the case for a decomposition, where modes defined on the surface of a particle, such as quasinormal modes or constant flux states, are used. Then the modes read $\mathbf{E}_k(\mathbf{r},\omega) = \sum_l C_l \mathbf{f}_l(\mathbf{r},\omega)$ and one gets an expansion in the form of

$$\mathbf{G}(\mathbf{r},\mathbf{r}',\omega) \approx \sum_{k,l} C_{kl} \mathbf{f}_k(\mathbf{r},\omega) \otimes \mathbf{f}_l(\mathbf{r}',\omega), \tag{3.20}$$

where also non diagonal entries in the expansion need to be accounted for and the number of coefficients therefore grows with N^2, where N is the number of basis functions used. In contrast to this, for basis functions leading to a decomposition of the form of Eq. (3.17), the number of coefficients is N. If we insert the expansion of Eq. (3.20) in the formula for the electron energy loss Eq. (2.15) we get a model, which can be solved for the coefficients C_{kl} with linear least square optimization. Unfortunately the least square optimization fails to converge to the Green tensor, as can be seen in Fig. 3.8, where a comparison between the true local density of states of a plasmonic nanoparticle and the one from a reconstructed Green tensor - via least square optimization - are plotted and show almost no agreement. In order to converge to the desired solution, one needs to implement some additional information in the reconstruction process. Choosing a basis, where the dyadic Green tensor can be decomposed into a form like Eq. (3.17), is one such assumption.

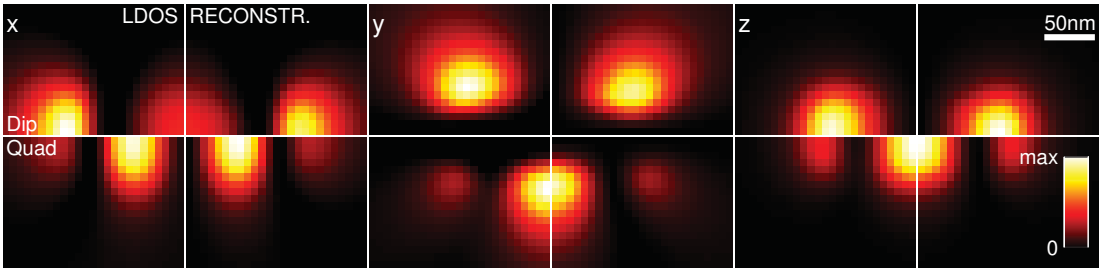

Figure 3.9: Least square reconstruction of the photonic local density of states of a rectangular nanoparticle with dimensions $200 \times 65 \times 30\text{nm}^3$ and a dielectric function for gold from the drude model. Shown are the dipolar (top figures) and quadrupolar (bottom figures) modes of the plasmonic structure and the true local density of states compared to the density of states evaluated from the reconstructed Green tensor by compressed sensing. As measurement data a set of rotated electron energy loss maps was used. As reconstruction basis bi-orthogonal eigenmodes, as described in subsection 2.2.5, where used. For further details, see [57].

Here, in order to derive such a basis set, one needs the particle geometry and the dielectric function of the material, as described in the former chapter. From the experimental point of view, it is not really a big problem to obtain the particle geometry, because usually one automatically gets some high angle annular dark field images in addition to electron energy loss maps, which can be used for a geometry reconstruction [82]. Even armed with the natural basis functions for the inverse problem, the solution shows no agreement with the true dyadic Green tensor (Fig. 3.8) and additional assumptions need to be made.

Assuming that only a small number of modes contribute to the electron energy loss, is such an assumption. When one looks at typical electron energy loss spectra (see e.g. [82, 110]), one finds that there are typically just a few Lorentz shaped peaks, which are attributed to different modes. Therefore this is probably a good assumption. In order to implement it, one could use compressed sensing optimization, where one searches for a solution with as little as possible coefficients unequal to zero, as described in section 3.3. Then the optimization problem reads

$$\min_{C_k} \left[\|C_k\|_{l_1} + \frac{1}{2\mu} \left\| \Gamma^{\mathbf{R}_{\hat{\mathbf{v}}}}_{\text{EELS}} - \Gamma^{\mathbf{R}_{\hat{\mathbf{v}}}}_{\text{MODEL}}[C_k] \right\|_{l_2} \right], \tag{3.21}$$

where μ is a parameter, which allows to switch between compressed sensing and simple linear least square optimization. A comparison of the true photonic local density of states with the one derived from the dyadic Green tensor, reconstructed by compressed sensing, provides excellent agreement, as can be seen in Fig. 3.9, showing that the assumption of a sparse basis and therefore a regularization term $\|C_k\|_{l_1}$ is a good choice.

4 Paper 1: Tomography of Particle Plasmon Fields from Electron Energy Loss Spectroscopy

Published in: Physical Review Letters (2013)

Tomography of Particle Plasmon Fields from Electron Energy Loss Spectroscopy

Anton Hörl, Andreas Trügler, and Ulrich Hohenester*

Institut für Physik, Karl-Franzens-Universität Graz, Universitätsplatz 5, 8010 Graz, Austria

(Received 12 April 2013; revised manuscript received 18 June 2013; published 13 August 2013)

We theoretically investigate electron energy loss spectroscopy (EELS) of metallic nanoparticles in the optical frequency domain. Using a quasistatic approximation scheme together with a plasmon eigenmode expansion, we show that EELS can be rephrased in terms of a tomography problem. For selected single and coupled nanoparticles we extract the three-dimensional plasmon fields from a collection of rotated EELS maps. Our results pave the way for a fully three-dimensional plasmon-field tomography and establish EELS as a quantitative measurement device for plasmonics.

DOI: 10.1103/PhysRevLett.111.076801 PACS numbers: 73.20.Mf, 68.37.Og, 78.20.Bh, 79.20.Uv

Electron energy loss spectroscopy (EELS) has emerged as an ideal tool for the study of surface plasmon polaritons and particle plasmons [1]. For surface plasmon polaritons, electrons with kinetic energies of a few to hundreds of keV penetrate through a metal film and excite surface and bulk plasmons, whose resonance frequencies can be directly extracted from the energy loss spectra [2,3]. By raster scanning the electron beam over a plasmonic nanoparticle, one can extract both the resonances and field maps of the particle plasmons [4,5]. This technique has been extensively used in recent years to map out the plasmon modes of nanotriangles [5–7], nanorods [4,8–10], nanodisks [11], nanocubes [12], nanoholes [13], and coupled nanoparticles [14–17].

Despite its success and widespread application, the interpretation of plasmonic EELS data remains unclear. In [18] the authors speculated that EELS renders the photonic LDOS, a quantity of immense importance in nano-optics [19], but the interpretation was questioned in [20]. A detailed comparison between LDOS and EELS was given recently in [21], where the authors provided an intuitive interpretation of different measurement schemes in terms of an eigenmode expansion. It should be noted that the controversy only concerns the interpretation, whereas the theoretical description of EELS maps is well established [1] and very good agreement between experiment and simulation has been achieved [5,8,11,12].

In this Letter we challenge the interpretation of EELS maps of plasmonic nanoparticles, and rephrase the problem in terms of a tomography scheme. For sufficiently small nanoparticles, where the quasistatic approximation can be employed, we expand the particle fields in terms of plasmonic eigenmodes [21–23] and the EELS signal becomes a simple spatial average along the electron propagation direction. We show by the example of single and coupled nanorods that the extraction of plasmon fields from EELS data can be reduced to an inverse Radon transformation, which is at the heart of most modern computer tomography algorithms [24]. Otherwise the field extraction can be formulated in terms of an inverse problem which can be solved by optimization techniques.

EELS simulation.—Electron energy loss is a two-step process, where the electron first excites a surface plasmon and, in turn, the electron has to perform work against the induced surface plasmon field. The energy loss becomes [1,2]

$$\Delta E = e\int \boldsymbol{v}\cdot\boldsymbol{E}_{\mathrm{ind}}[\boldsymbol{r}_e(t),t]dt = \int_0^\infty \hbar\omega\Gamma_{\mathrm{EELS}}(\omega)d\omega, \quad (1)$$

where $-e$ and $\boldsymbol{v}$ are the charge and velocity of the electron, respectively, and $\boldsymbol{E}_{\mathrm{ind}}$ is the electric field of the surface plasmon evaluated at the electron positions. In the second expression of Eq. (1) we have spectrally decomposed the different loss contributions and introduced the loss probability Γ_{EELS}. A similar expression can also be obtained from a fully quantum-mechanical description scheme [1]. For nanoparticles much smaller than the wavelength of light, one can employ the quasistatic limit by keeping only the scalar potential and performing the static limit for the Green functions, while retaining the full frequency dependence for the material permittivities [1]. We are then led to [1,25]

$$\Gamma_{\mathrm{EELS}}(\boldsymbol{R}_0,\omega) = -\frac{e^2}{\pi\hbar v^2}\int_{-\infty}^{\infty} dzdz' \times \mathrm{Im}[e^{-i\omega z/v}G_{\mathrm{ind}}(\boldsymbol{r}_e,\boldsymbol{r}_e',\omega)e^{i\omega z'/v}]dzdz' \quad (2)$$

for the loss probability. Here G_{ind} is the Green function in the quasistatic limit that describes the response of the metallic nanoparticle [1,20]. We next introduce plasmonic eigenmodes [21–23] defined through

$$\int_{\partial\Omega}\frac{\partial G(\boldsymbol{s},\boldsymbol{s}')}{\partial n}\sigma_k(\boldsymbol{s}')da' = \lambda_k\sigma_k(\boldsymbol{s}), \quad (3)$$

where λ_k and $\sigma_k(\boldsymbol{s})$ denote the plasmonic eigenvalues and eigenmodes, respectively, and $\partial G/\partial n$ is the derivative of the Green function of an unbounded medium with respect to the outer surface normal. The eigenmodes are orthogonal in the sense $\int\sigma_k(\boldsymbol{s})G(\boldsymbol{s},\boldsymbol{s}')\sigma_{k'}(\boldsymbol{s})dada' = \delta_{kk'}$ and can be chosen real [22,23]. Let $\phi_k(\boldsymbol{r}) = \int_{\partial\Omega}G(\boldsymbol{r},\boldsymbol{s})\sigma_k(\boldsymbol{s})da$ denote the potential of the kth eigenmode. The induced

Green function can then be decomposed into these eigenmodes according to [21]

$$G_{\mathrm{ind}}(\boldsymbol{r},\boldsymbol{r}') = -\sum_k \frac{\lambda_k \pm 2\pi}{\Lambda + \lambda_k}\phi_k(\boldsymbol{r})\phi_k(\boldsymbol{r}')\frac{1}{\varepsilon(\boldsymbol{r}')}, \quad (4)$$

with $\Lambda = 2\pi(\varepsilon_1 - \varepsilon_2)/(\varepsilon_1 + \varepsilon_2)$ and ε_1 and ε_2 being the dielectric functions inside and outside the particle, respectively. The plus and minus signs correspond to the situations where $\boldsymbol{r}'$ lies outside or inside the particle. Inserting Eq. (4) into the loss probability of Eq. (2), we obtain for an electron trajectory that does not penetrate the particle the final result

$$\Gamma^{\mathrm{out}}_{\mathrm{EELS}}(\boldsymbol{R}_0,\omega) = -\frac{e^2}{\pi\hbar v^2\varepsilon_2}\sum_k \mathrm{Im}\left(\frac{\lambda_k + 2\pi}{\Lambda + \lambda_k}\right) \times \left|\int_{-\infty}^{\infty} e^{i\omega z/v}\phi_k(\boldsymbol{r})dz\right|^2. \quad (5)$$

This expression, which has been previously derived in [21], forms the starting point for our following analysis. At a plasmon resonance, defined through $\mathrm{Re}[\Lambda(\omega) + \lambda_k] = 0$, the resonance term in Eq. (5) becomes large and its contribution can dominate the total loss probability. Let us assume for the moment that $\omega z/v \ll 1$, such that the EELS probability for the single, dominant mode reduces to

$$\Gamma^{\mathrm{out}}_{\mathrm{EELS},\theta}(\boldsymbol{R}_0,\omega) \sim |\mathcal{R}_\theta[\phi_k(\boldsymbol{r})]|^2. \quad (6)$$

Here $\mathcal{R}_\theta$ is the Radon transformation [24,26] that performs a line integration of $\phi_k(\boldsymbol{r})$ along the z direction. We have included in Eq. (6) an angle θ that accounts for a possible rotation of the integration axis, as schematically depicted in Fig. 1. A collection of Radon transformations for a complete set of rotation angles is conveniently called a sinogram [26]. The projection-slice theorem then states that one can uniquely reconstruct the original function from the sinogram. Equation (6) differs from a normal sinogram in that Γ_{EELS} depends on the square of the Radon transforms, which leads to a sign ambiguity in the sinogram. In the following we first analyze a situation where the sign ambiguity can be ignored, and we will discuss the more general situation further below.

Results.—We first consider the setup depicted in Fig. 1, where an electron beam is raster scanned over a single nanorod and the EELS maps are recorded for different loss energies $\hbar\omega$ and rotation angles θ. In Fig. 2(a) we show the simulated EELS spectrum for the electron beam positions shown in the inset. We use a dielectric function for silver [27] and employ the MNPBEM toolbox [28] for the solution of the full Maxwell equations (without the quasistatic approximation). At low loss energies one observes two peaks which can be attributed to the dipolar and quadrupolar plasmon modes. Owing to the symmetry of the modes, an electron propagating along z always passes through regions where $\phi_k(\boldsymbol{r})$ is either solely positive or negative, which allows us to perform the inverse Radon transformation in Eq. (6). Results are reported in 2(d) and 2(e), showing almost perfect agreement between the reconstructed

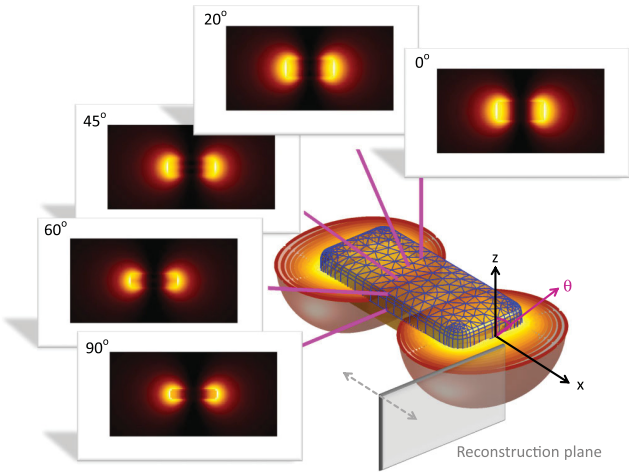

FIG. 1 (color online). Schematics of EELS tomography. An electron beam is raster scanned over a metallic nanoparticle, and EELS maps are recorded for different rotation angles θ. The main panel shows the isosurface and contour lines for the modulus of the dipolar surface plasmon potential, and the insets report the different EELS maps. From the complete collection of maps one can reconstruct the plasmon fields, as described in text (positions of reconstruction planes used in Figs. 2 and 3 are indicated in the main panel).

potentials and $\phi_k(\boldsymbol{r})$, apart from the potential sign that cannot be reconstructed from the EELS data. This is an encouraging finding, considering that our EELS maps are obtained from the solutions of the full Maxwell equations.

In Fig. 3 we show EELS maps for coupled nanoparticles, which have received considerable interest in recent years [14–17,20], partially due to their importance for surface enhanced Raman scattering [29,30]. Inside the gap region the EELS signal becomes zero for the bonding mode and maximal for the antibonding mode, as discussed in detail in Ref. [20]. However, from the reconstructed potential maps one observes a significant variation of the bonding potential along x, indicating a strong electric field in the gap region, contrary to the antibonding mode which has only a weak dependence along x. Thus, although "being blind to hot spots" [20,31], EELS tomography even allows us to reconstruct the complete field distribution inside the gap region.

The situation becomes more complicated when the electron passes through the metallic nanoparticle, and the induced Green function in Eq. (4) has to be separated into contributions where the electron is either inside or outside the metallic particle. Inside the metal the electron becomes efficiently screened by free electrons through the ε^{-1} term. To a good approximation, we can ignore this contribution and approximate the EELS probability by

$$\Gamma_{\mathrm{EELS},\theta}(\boldsymbol{R}_0,\omega) \sim (\mathcal{R}_\theta[\phi_k(\boldsymbol{r})])(\mathcal{R}_\theta[\phi_k^{\mathrm{out}}(\boldsymbol{r})]), \quad (7)$$

where $\phi_k^{\mathrm{out}}(\boldsymbol{r})$ is the potential that is artificially set to zero inside the particle. In Eq. (7) it is no longer possible to

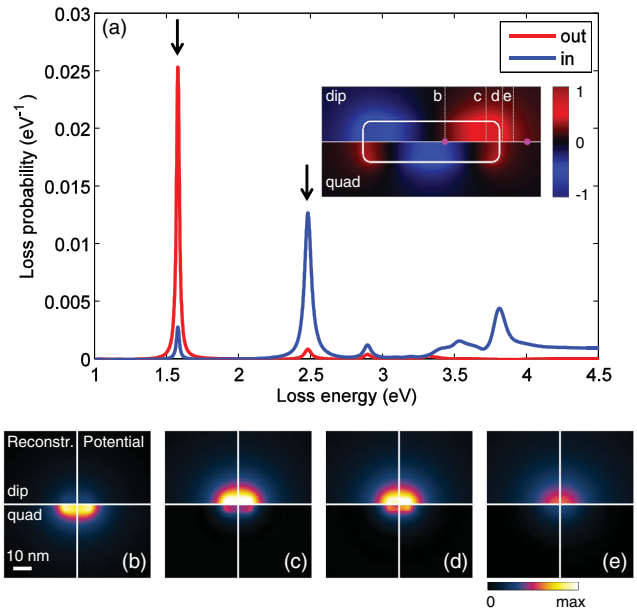

FIG. 2 (color online). (a) EELS spectrum for silver nanorod with dimensions of $50 \times 15 \times 7$ nm^3 and for the two beam positions indicated with circles in the inset. The inset also reports the potentials maps for the dipole and quadrupole mode at $z = 0$. The dashed lines indicate the positions of the planes where the potentials are reconstructed from the collection of EELS maps. (b)–(e) Potential maps reconstructed from EELS maps (left-hand panels) and potential maps (right-hand panels) for dipole mode (upper panels) and quadrupole mode (lower panel). In the simulations we assume a kinetic electron energy of 200 keV and use a dielectric constant of 1.6 for the embedding medium.

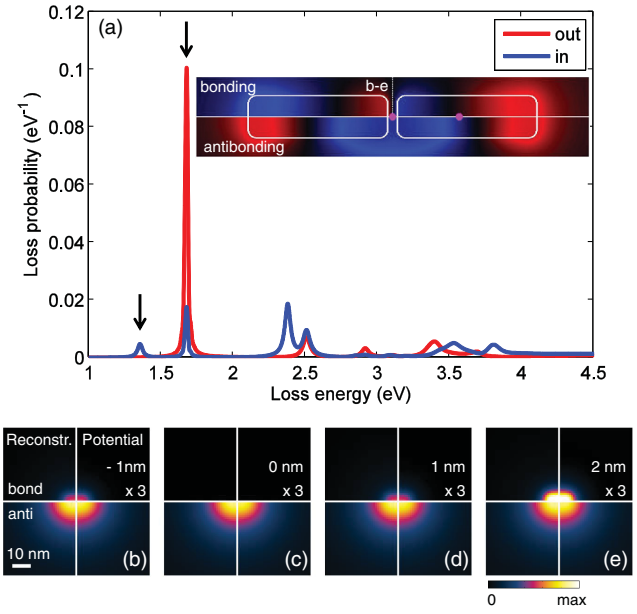

FIG. 3 (color online). (a) Same as Fig. 2 but for coupled nanorods. The particle and simulation parameters are the same as those given in the caption of Fig. 2, the gap distance between the nanoparticles is 5 nm. In the inset we report the potentials for the bonding and antibonding modes. (b)–(e) Reconstructed and true potential maps at different x positions, reported in the panels, as measured with respect to the gap center. For clarity, the potentials for the bonding mode are multiplied by a factor of 3.

perform an inverse Radon transformation to reconstruct the plasmon potential, and we have to proceed in a different manner. First, we introduce a cost function that measures the distance between the computed EELS probabilities and those computed from Eq. (7). Let f_0 denote the EELS probabilities for all impact parameters and rotation angles, and $f[\phi_k(\boldsymbol{r})]$ the corresponding probabilities computed from Eq. (7). In a second step we then determine, starting from some reasonable initial guess, those potentials that minimize the cost function $J = (1/2)|f_0 - f[\phi_k(\boldsymbol{r})]|^2$ using a nonlinear conjugate gradient method [32]. In most cases the initial guess for the potentials was not overly critical and the minimization algorithm converged after a few iterations. Figures 2(b) and 2(c) report the reconstructed potentials and $\phi_k(\boldsymbol{r})$ for electrons penetrating through the metallic nanoparticle, and we again observe very good agreement.

Having established a numerical optimization scheme for the potential through minimization of the cost function, we can also rephrase the EELS tomography problem of Eqs. (5) and (6) in a way that appears better suited for experimental implementation and that can also be employed for more complicated structures. To this end, we first note that the source for the potential $\phi_k(\boldsymbol{r})$ is the charge distribution $\sigma_k(\boldsymbol{s})$ of the eigenmodes, and one can reconstruct equally well the surface charge distribution or the potential. We next rewrite Eq. (5) in the form

$$\Gamma^{\text{out}}_{\text{EELS},\theta}(\boldsymbol{R}_0, \omega) = \sum_k C_k(\omega) \left| \int \phi^*_{\boldsymbol{R}_0,\theta}(\boldsymbol{s}) \sigma_k(\boldsymbol{s}) da \right|^2, \quad (8)$$

where $\phi_{\boldsymbol{R}_0,\theta}(\boldsymbol{s}) = -(e/v) \int_{-\infty}^{\infty} G(\boldsymbol{s}, \boldsymbol{r}_e) e^{i\omega z_e/v} dz_e$ is the potential of the electron propagating along $\boldsymbol{r}_e$, with direction θ and impact parameter $\boldsymbol{R}_0$, and the form of $C_k(\omega)$ follows directly from the comparison with Eq. (5). Equation (8) allows for the reconstruction of $\sigma_k(\boldsymbol{s})$, which can be approximated by boundary elements (as used in our simulation approach [28]) or some free-form surface functions such as nonuniform splines, provided that the nanoparticle surface is known [26]. In what follows, we again set $\omega/v \approx 0$.

Figure 4 shows for a number of particle shapes the reconstruction based on Eq. (8). In all cases we used for the initial guess a mode profile with proper symmetry, whereas other details turned out to be unimportant. Figure 4(a) reports $\sigma_k(\boldsymbol{s})$ (left) and the reconstructed surface charge distributions (right) for the dipolar and quadrupolar nanorod modes, which are in very good agreement. In Fig. 4(b) we show results for a disk-shaped particle with two degenerate eigenmodes. For the reconstruction, we keep in Eq. (8) two modes with identical coefficients C_k, and ensure that, because of symmetry, the

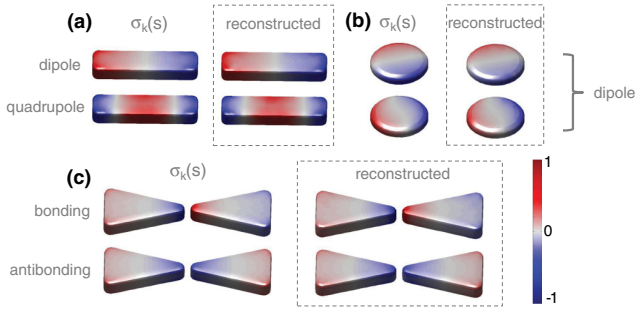

FIG. 4 (color online). Surface charge distribution $\sigma_k(\boldsymbol{s})$ of eigenmodes (left) and surface charge distribution reconstructed from the EELS maps (right), using Eq. (8), for (a) nanorod, (b) nanodisk, and (c) bowtie geometry. Surface charge distribution is given in arbitrary units. For the reconstruction of σ_k we consider EELS maps with a resolution of 40×40 pixels, and use 45 rotation angles within $\theta \in [0, 90°]$ (similar results were obtained with only 10 rotation angles).

charge distributions of these modes are identical but rotated by 90° with respect to each other. Again the optimization procedure comes up with the correct modes. We emphasize that a similar approach could be used for modes that are energetically close to each other, although in this case the coefficients C_k are different and the optimization should include EELS maps for different loss energies. Finally, Fig. 4(c) shows the bonding and antibonding mode distributions for a bowtie geometry, demonstrating that our approach can also be applied to more complicated structures.

In Fig. 5 we compare for the nanorod the true and reconstructed potentials along the line (e) shown in the inset of Fig. 2(a) [$z = 0$]. We observe that the quasistatic potential and the potentials reconstructed from the EELS maps, through either the Radon transformation [Eq. (6)] or the surface charges of Eq. (8), are in good agreement, demonstrating the quantitative measurement capability of our approach. The comparison with the retarded potentials is complicated by the fact that there exists no clear eigenmode concept for the full Maxwell equations, and we thus we have to proceed in a different manner. In the figure we show the modulus of the induced potentials for a plane-wave excitation (we use an incidence angle of 45° where both dipolar and quadrupolar modes can be excited). Good agreement between the solutions of the quasistatic and full Maxwell equations is found, with only small deviations at larger positions, attributed to the different excitation conditions and/or retardation effects not included in the quasistatic solutions.

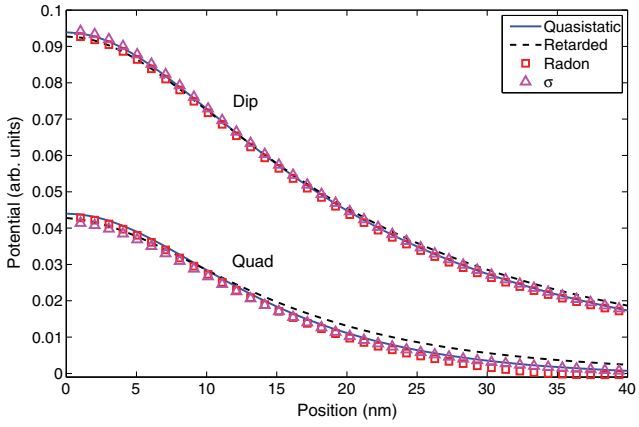

FIG. 5 (color online). Eigenmode potential $\phi_k(\boldsymbol{r})$ (solid line) and reconstructed potentials along the line (e) shown in the inset of Fig. 2(a) [$z = 0$]. For the reconstruction we use either the inverse Radon transformation of Eq. (6) (square symbols) or the surface charge decomposition of Eq. (8) (triangles). The square modulus of the retarded scalar potential (scaled by an arbitrary factor) is computed for a plane-wave excitation, as described in text.

There are several reasons why Eq. (8) is advantageous in comparison to Eq. (6). First, while $\sigma_k(\boldsymbol{s})$ can typically be represented by a few tens to hundreds of boundary elements or parameters, the EELS maps for different rotation angles provide a much larger data set, thus making the optimization procedure for the reconstruction a highly overdetermined problem. The reason for this overdetermination is the two-dimensional nature of the surface charge distribution, whereas the potential, which is uniquely determined by $\sigma_k(\boldsymbol{s})$, can be measured in the entire three-dimensional space. For the reconstruction of $\sigma_k(\boldsymbol{s})$ one can thus even discard trajectories where the electrons pass through the nanoparticle, which are problematic in experiment because of the electron attenuation within the metal. The inverse Radon transformation additionally requires a large field of view, to properly include the far-reaching components of the dipolar or multipolar surface plasmon fields, in contrast to Eq. (8) that can be restricted to significantly smaller regions. Consideration of finite wave numbers ω/v naturally enters the framework of Eq. (8), in the spirit of diffraction tomography [33], although in this work we have neglected for simplicity such wave number effects. Finally, effects of substrates or layers supporting the nanoparticles can be included in our approach by replacing in Eq. (3) and in the definition of $\phi_{\boldsymbol{R}_0,\theta}(\boldsymbol{s})$ the Green function of an unbounded medium by that including substrate or layer effects. The main limitations of our tomography scheme are probably the quasistatic approximation, which restricts the scheme to sufficiently small particles, and the high degree of preknowledge needed for the surface charge reconstruction (homogeneous dielectric function of particle, surface charge distributions as the only source for plasmonic fields).

We are grateful to Gerald Kothleitner, Toni Uusimäki, Franz Schmidt, Harald Ditlbacher, and Joachim Krenn for very helpful discussions. This work has been supported by the Austrian Science Fund FWF under Project No. P24511-N26 and the SFB NextLite.

*ulrich.hohenester@uni-graz.at

[1] F. J. Garcia de Abajo, Rev. Mod. Phys. **82**, 209 (2010).
[2] R. H. Ritchie, Phys. Rev. **106**, 874 (1957).
[3] C. J. Powell and J. B. Swan, Phys. Rev. **115**, 869 (1959).
[4] M. Bosman, V. J. Keast, M. Watanabe, A. I. Maaroof, and M. B. Cortie, Nanotechnology **18**, 165505 (2007).
[5] J. Nelayah, M. Kociak, O. Stephan, F. J. Garcia de Abajo, M. Tence, L. Henrard, D. Taverna, I. Pastoriza-Santos, L. M. Liz-Martin, and C. Colliex, Nat. Phys. **3**, 348 (2007).
[6] J. Nelayah, L. Gu, W. Sigle, C. T. Koch, I. Pastoriza-Santos, L. M. Liz-Martin, and P. A. van Anken, Opt. Lett. **34**, 1003 (2009).
[7] B. Schaffer, W. Grogger, G. Kothleitner, and F. Hofer, Ultramicroscopy **110**, 1087 (2010).
[8] B. Schaffer, U. Hohenester, A. Trügler, and F. Hofer, Phys. Rev. B **79**, 041401(R) (2009).
[9] O. Nicoletti, M. Wubs, N. A. Mortensen, W. Sigle, P. A. van Aken, and P. A. Midgley, Opt. Express **19**, 15 371 (2011).
[10] D. Rossouw and G. A. Botton, Phys. Rev. Lett. **110**, 066801 (2013).
[11] F.-P. Schmidt, H. Ditlbacher, U. Hohenester, A. Hohenau, F. Hofer, and J. R. Krenn, Nano Lett. **12**, 5780 (2012).
[12] S. Mazzucco, N. Geuquet, J. Ye, O. Stéphan, W. Van Roy, P. Van Dorpe, L. Henrard, and M. Kociak, Nano Lett. **12**, 1288 (2012).
[13] W. Sigle, J. Nelayah, C. Koch, and P. van Aken, Opt. Lett. **34**, 2150 (2009).
[14] M. W. Chu, V. Myroshnychenko, C. H. Chen, J. P. Deng, C. Y. Mou, and J. Garcia de Abajo, Nano Lett. **9**, 399 (2009).
[15] M. N'Gom, S. Li, G. Schatz, R. Erni, A. Agarwal, N. Kotov, and T. B. Norris, Phys. Rev. B **80**, 113411 (2009).
[16] A. L. Koh, K. Bao, I. Khan, W. E. Smith, G. Kothleitner, P. Nordlander, S. A. Maier, and D. W. McComb, ACS Nano **3**, 3015 (2009).
[17] A. L. Koh, A. I. Fernandez-Dominguez, D. W. McComb, S. A. Maier, and J. K. W. Yang, Nano Lett. **11**, 1323 (2011).
[18] F. J. Garcia de Abajo and M. Kociak, Phys. Rev. Lett. **100**, 106804 (2008).
[19] L. Novotny and B. Hecht, *Principles of Nano-Optics* (Cambridge University Press, Cambridge, England, 2006).
[20] U. Hohenester, H. Ditlbacher, and J. R. Krenn, Phys. Rev. Lett. **103**, 106801 (2009).
[21] G. Boudarham and M. Kociak, Phys. Rev. B **85**, 245447 (2012).
[22] F. Ouyang and M. Isaacson, Philos. Mag. B **60**, 481 (1989).
[23] I. D. Mayergoyz, D. R. Fredkin, and Z. Zhang, Phys. Rev. B **72**, 155412 (2005).
[24] G. T. Herman, *Image Reconstruction from Projections: The Fundamentals of Computerized Tomography* (Academic, New York, 1980).
[25] F. J. Garcia de Abajo and J. Aizpurua, Phys. Rev. B **56**, 15 873 (1997).
[26] P. A. Midgley and M. Weyland, Ultramicroscopy **96**, 413 (2003).
[27] P. B. Johnson and R. W. Christy, Phys. Rev. B **6**, 4370 (1972).
[28] U. Hohenester and A. Trügler, Comput. Phys. Commun. **183**, 370 (2012).
[29] I. Khan, D. Cunningham, S. Lazar, D. Graham, W. Ewen Smith, and D. W. McComb, Faraday Discuss. **132**, 171 (2006).
[30] N. Mirsaleh-Kohan, V. Iberi, P. D. Simmons, N. W. Bigelow, A. Vaschillo, M. M. Rowland, M. D. Best, S. J. Pennycook, D. J. Masiello, and B. S. Guiton *et al.*, J. Phys. Chem. Lett. **3**, 2303 (2012).
[31] N. Zabala, A. Rivacoba, and P. M. Echenique, Phys. Rev. B **56**, 7623 (1997).
[32] R. Roy and E. M. Sevick-Muraca, Opt. Express **9**, 49 (2001).
[33] M. M. Bronstein, A. M. Bronstein, M. Zibulevsky, and H. A. Azhari, IEEE Trans. Med. Imaging **21**, 1395 (2002).

5 Paper 2: Effect of multipole excitations in electron energy-loss spectroscopy of surface plasmon modes in silver nanowires

Published in: Journal of Applied Physics (2014)

JOURNAL OF APPLIED PHYSICS **116**, 223101 (2014)

Effect of multipole excitations in electron energy-loss spectroscopy of surface plasmon modes in silver nanowires

Xiuli Zhou,[1] Anton Hörl,[2] Andreas Trügler,[2] Ulrich Hohenester,[2] Theodore B. Norris,[1] and Andrew A. Herzing[3,a)]

[1]*Center for Ultrafast Optical Science, University of Michigan, Ann Arbor, Michigan 48109, USA*
[2]*Institut für Physk, Karl-Franzens-Universität Graz, 8010 Graz, Austria*
[3]*Material Measurement Laboratory, National Institute of Standards and Technology, Gaithersburg, Maryland 20899, USA*

(Received 8 October 2014; accepted 19 November 2014; published online 8 December 2014)

We have characterized the surface plasmon resonance (SPR) in silver nanowires using spatially resolved electron energy loss spectroscopy (EELS) in the scanning transmission electron microscope. Non-symmetric EELS spectra due to high-k SPR propagation along the nanowire and spectral shifts due to higher-order mode excitation are observed when the beam is positioned near the tip of the nanowire. When the beam is far from the tip region and on the side of nanowire, no spectral shifts are observed as the beam is scanned in the radial direction of the nanowire. The experimental spectra are compared with three different theoretical approaches: direct numerical calculation of the energy loss, analytical models for energy loss, and numerical simulations using an optical model. All three models reproduce the spectral shifts as the electron beam approaches the cap of the nanowire. The analytical model reveals the origin of the shifts in high-order plasmon mode excitation. © *2014 AIP Publishing LLC*. [http://dx.doi.org/10.1063/1.4903535]

I. INTRODUCTION

The surface plasmon resonance (SPR) modes of metal nanoparticles (NPs) enable the development of nano-optics and the manipulation of light at length scales far below the diffraction limit. In recent years, researchers have developed an extraordinary degree of control over the propagation of confined optical modes on the nanoscale in a variety of metallic systems. The character of SPR modes has been studied for varieties of geometries, including cubes,[1] prisms,[2] rods, and wires.[3–5] Metal nanowires are of particular interest since they may serve as the building blocks of more complex plasmonic systems or circuits. Metal nanowires exhibit an enhanced polarizability compared to more spherical shapes, and their resonance frequency can be tuned by changing their length and/or diameter and the composition of the surrounding medium. Some recently published theoretical analysis and experimental measurements have illustrated their optical properties and potential applications.[6–8]

In order to determine their spectral properties or their suitability for various applications, SPR modes are typically excited optically. In this case, it is difficult to study the spatial modes in great detail since no optical characterization with truly single-nanometer spatial resolution exists. However, electron energy loss spectroscopy (EELS) performed in the scanning transmission electron microscope (STEM) is capable of such resolution. In recent years, EELS has become a powerful tool to study optical-frequency SPR modes in individual nanostructures as a result of the improved energy resolution enabled by electron monochromators.[4,5,9] In this case, the attainable energy resolution approaches the width of SPR excitations in noble metals[10] and the signal can be acquired with nanometer-scale spatial resolution.[11]

Theoretical and experimental investigations of SPR excitation using EELS have been conducted on a variety of nanostructures, including single NPs of various shapes, nanoparticle arrays, thin films, and composite metamaterials.[10,12–16] Specifically for wire-type structures, Nicoletti *et al.*[17] and Rossouw *et al.*[18] have both recently utilized EELS to map the spatial extent of SPR's in single silver nanorods. They observed confined modes along the length of the wires as well as anti-node bunching of high-order resonant modes at the nanowire ends. They illustrated mode confinement effects and interpreted their results with the aid of optical excitation calculations, which were found to be in good agreement with experiment. Rossouw and Botton also analyzed the resonant modes of bent and kinked silver nanowires for their potential use in nanophotonic circuits.[19] Interestingly, no interruption of the mode propagation was observed due to the bends and kinks, such that the optical response was similar to that of a straight wire.

In this work, we further explore EELS of silver NWs, presenting new data on the detailed dependence of the spectral response on the electron beam position near the nanowire surface. We observe an asymmetrical loss spectrum and spectral shifts in the loss peak that we attribute to high-order mode excitation. To aid interpretation, we compare the experimental results with previously published analytical theories, optical excitation models, and direct calculation of electron energy loss probability.

II. EXPERIMENTAL SETUP

Silver nanowires were synthesized through $CuCl_2$ mediated polyol reduction.[20] 5 ml of ethylene glycol (EG) in a

a)Author to whom correspondence should be addressed. Electronic mail: tnorris@umich.edu

20 ml disposable glass vial was submerged in an oil bath and heated to 150 °C under magnetic stirring. After 1 h of heating, 40 ml of 4 mM $CuCl_2{\cdot}2H_2O$ in EG was added and the solution was heated for an additional 15 min. 3 ml of 147 mM polyvinylpyrrolidone (PVP) and 3 ml of 94 mM $AgNO_3$ solutions in EG were synchronously injected into the heated EG solution at a constant flow rate of 0.45 ml/min. Upon the formation of long silver nanowires, an hour from the injection of PVP and $AgNO_3$, the solution turned opaque and wispy gray. The silver nanowires were separated from the EG and PVP by centrifugation at 209 rad/s (2000 RPM) for 20 min in acetone and re-dispersed in water.

The silver nanowires were dispersed in organic solvents by replacing the PVP with an alkanethiol.[21] Specifically, 1 mg/ml of silver nanowires in ethanol were mixed with 10 mM of 1-undecanethiol (UDT) in chloroform in equal volume and sonicated for 10 min after which the mixture was left for 24 h. This allowed for displacement of the PVP and formation of a UDT self-assembled monolayer on the nanowires. The silver nanowires were further purified by centrifugation, supernatant extraction, and re-suspension in target organic solvents.

In preparation for STEM-EELS analysis, silver nanowires were deposited from solution by drop-casting onto a thin lacey-carbon film supported on a standard 3 mm copper mesh grid. EELS spectrum imaging and high-angle annular dark-field imaging (HAADF) were carried out using an FEI Titan 80–300 STEM equipped with a double-hexapole spherical aberration corrector on the probe-forming side of the objective lens and a Wien-filter monochromator.[31] The instrument was operated at an accelerating voltage of 300 kV using an accelerating gun lens resulting in a final probe current of ≈100 pA. While the spherical aberration corrector permits the formation of an electron probe with a diameter of approximately 0.1 nm, additional source magnification is incurred due to the dispersive action of the monochromator. The exact probe shape is difficult to measure and calculate, but the final probe size is on the order of 0.3 nm.

Spectroscopy was carried out with a Gatan Tridiem 865 imaging energy-filter, with typical acquisition times of 100 ms per spectrum, using a convergence angle of 13 mrads and a collection angle of 13 mrads. The energy dispersion was set to 0.01 eV/channel. To provide a measure of the energy-resolution of the system under these conditions, the full-width half maximum and full-width tenth maximum of the zero-loss peak were measured and found to be 0.2 eV and 0.5 eV, respectively. Spectra were aligned in the energy dimension using Matlab code to set the channel with maximum intensity to zero energy-loss. While it was impossible to analyze free-standing NWs, in order to minimize substrate effects, care was taken to analyze only the ends of those NWs that extended far from the underlying amorphous carbon support. STEM-HAADF images were collected both before and after EELS acquisition. Images collected prior to analysis showed that the nanowires exhibited clean surfaces, with no evidence of oxide or carbonaceous surface layers present. However, the presence of ultrathin layers of this kind cannot be entirely ruled out. Images collected after analysis showed that some hydrocarbon deposition did occur during the analysis. No other evidence of specimen alteration was observed.

In order to study the plasmon modes in detail, we performed EELS of individual silver nanowires. In the first set of experiments, we acquired EELS spectra at a series of electron beam positions relative to the nanowire. All spectra are presented as they were acquired, without applying background subtraction or deconvolution. We investigated the dependence of the spectral response on the distance of the beam from the nanowire tip and the distance from the side of the nanowire in a region that was far from the tip. The spectral response was also measured at a fixed distance from the side of the wire as a function of distance from the wire's tip. This measurement was complemented by hyperspectral EELS imaging of the entire region of the nanowire within several hundred nanometers of the tip.

III. RESULTS

EELS spectra collected as a function of beam distance from the tip of the nanowire are shown in Fig. 1(a). The inset shows the experimental setup, where spectra were acquired every nanometer along a 50 nm line (indicated in orange). The acquisition began with the beam positioned inside of the wire and then moving away from it into the surrounding vacuum. A 2-D plot of the spectral response vs. beam position is given in Fig. 1(a), with the white dashed line indicating the interface between the tip of the nanowire and vacuum. A similar set of data was acquired for beam positions scanned perpendicular to the side of the nanowire, and this is shown in Fig. 1(b). Spectra extracted at various intervals along the line of acquisition are presented in Figs. 1(c) and 1(d). In all cases, a strong loss peak due to SPR has been excited near 3.6 eV. The SPR excitation efficiency drops off exponentially as the beam moves away from the wire, corresponding to the confinement of the SPR mode to the metal surface, as has been established by a number of recent studies.[4,18,22,23] When the beam is positioned near the tip of the nanowire, the SPR peak is highly asymmetric and broad. In addition, the peak was observed to continuously shift from ≈3.5 eV when the beam was near the metal-vacuum interface to ≈3.3 eV when the beam was 25 nm away as indicated by the dashed black line in Fig. 1(c). By contrast, as shown in Figs. 1(b) and 1(d), the spectral peak in the transverse case was relatively narrow and was positioned at 3.6 eV regardless of beam position.

SPR propagation along the side of the nanowire was also investigated by positioning the beam at the positions indicated in the STEM image shown in Figure 2(a). The corresponding EELS spectra for each of these positions contain a strong peak at ≈3.6 eV, as well as a series of peaks at lower energy-loss (indicated by arrows). These lower energy-loss peaks are due to the excitation of Fabry-Perot modes along the wire due to its finite length.[17,18] Moreover, it is shown that the strongest silver SPR peak occurs at ≈3.6 eV when the beam is positioned along the side of the wire, but that the peak shifts to ≈3.5 eV when the beam is moved to the tip of the nanowire. This observed difference in the energy-loss position is consistent with the previously presented spectra.

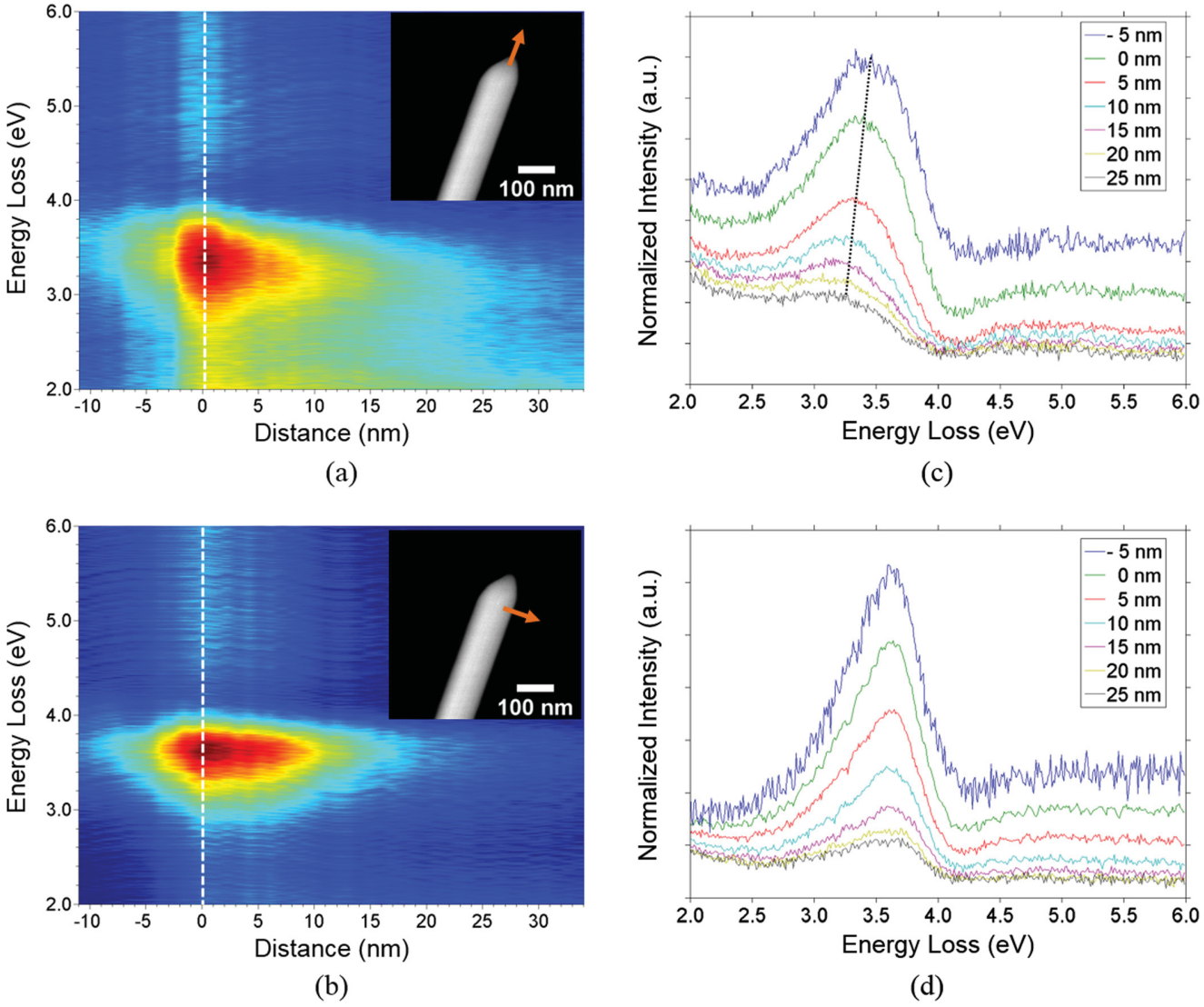

FIG. 1. Experimental EELS spectra collected near the end of a 100 nm diameter silver nanowire with the beam traveling in (a) the longitudinal direction and (b) the transverse direction. The inset STEM-HAADF images show the region analyzed. Data were collected serially in 1 nm increments in the direction indicated by the orange arrow. The white dashed line overlaid in the EELS data represents the interface between the silver nanowire and vacuum which is set as the origin of the abscissa. Also shown are EELS spectra as a function of distance from the nanowire surface along the (c) longitudinal direction and (d) the transverse direction.

Figs. 2(b) and 2(c) show another STEM-HAADF image of the nanowire and the corresponding spectra obtained along the wire surface at the indicated positions. In this case, the Fabry-Perot modes are again observed at low energy-loss in addition to a pair of stronger peaks positioned at 3.5 eV and 3.75 eV. As discussed previously, the former peak is due to the delocalized SPR at the wire-vacuum boundary, while the latter is due to the bulk plasmon loss as the beam passes through the wire itself.[4,24,25]

The spatial distribution of the low-energy modes was observed by extracting images from an EELS spectrum image at varying energy-loss values, and a subset of the data is shown in Fig. 3(a). As observed in the previous studies,[17–19] the propagating modes along the length of the wire become standing waves in a finite system due to boundary confinement resulting in the Fabry-Perot type resonances. These images can be compared to simulated electric field distributions obtained by finite-difference time-domain (FDTD) simulations of the optical response of the nanowire (Fig. 3(b)) and the results are qualitatively quite similar. By measuring the spatial separation between the peaks of each SPR mode in Figs. 3(a) and 3(b), the dispersion relations are obtained and plotted in Fig. 3(c). The values of k (in nm^{-1}) are measured from the experimental EELS series in Fig. 3(a) and the simulated series in Fig. 3(b). k is given by

$$k = \frac{2\pi}{\lambda_{sp}},$$

where λ_{sp} is the wavelength between two resonance peaks. For a given resonance mode, the spacing between adjacent maxima of intensity varies slightly along the silver nanowire, so that the k does not have a unique value. The theoretical dispersions from a model neglecting retardation and substrate

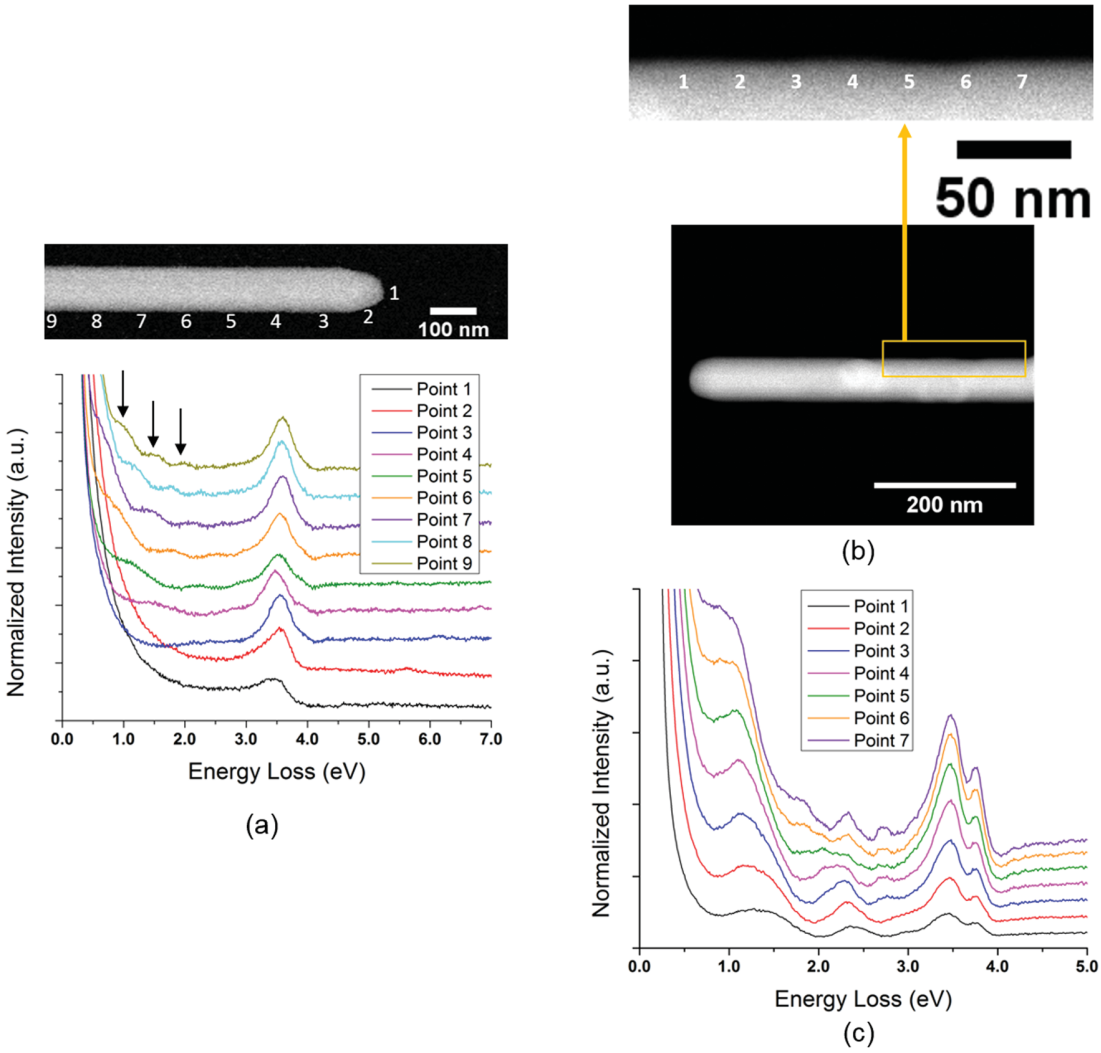

FIG. 2. (a) STEM-HAADF image of 100 nm diameter silver nanowire and corresponding EELS spectra extracted from the numbered locations. The strongest SPR peaks are at ≈3.5 eV to ≈3.6 eV, while the black arrows highlight the Fabry-Perot resonances observed at lower energy-loss, the position of which depends strongly on distance from the nanowire tip. (b) STEM-HAADF image of a silver nanowire and a zoomed image of the region analyzed by EELS. (c) Corresponding EELS spectra extracted from the seven numbered positions denoted in (c).

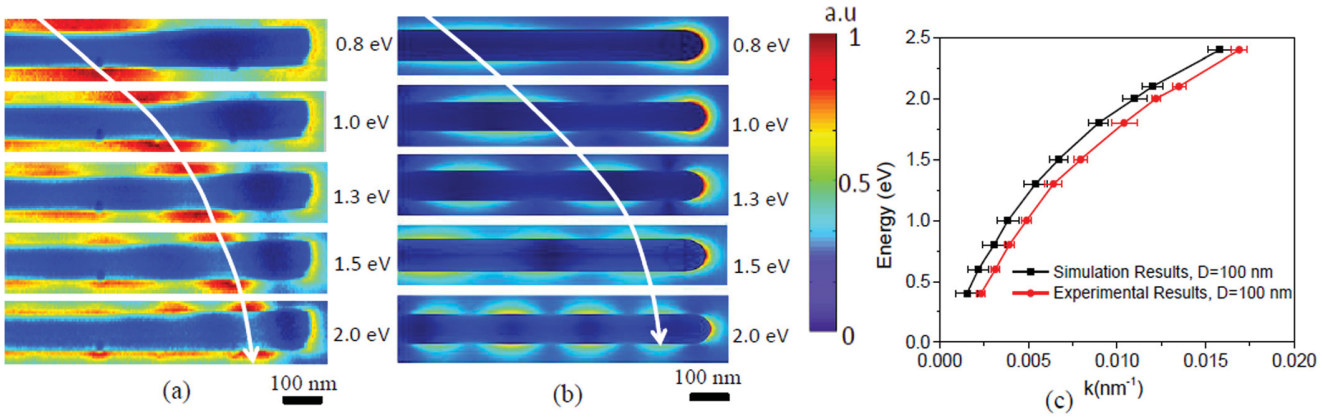

FIG. 3. (a) Images extracted from a EELS hyperspectral dataset acquired from near the end of a 100 nm diameter. The images show the spatially resolved EELS response at various energy-loss values and depict the standing wave pattern in the nanowire resulting from surface plasmon resonances. (b) Simulated electric field distributions resulting from optical excitation of a model silver nanowire. The intensity has been scaled independently for all of the images in. (c) Experimental and calculated dispersion relations as a function of wavenumber k, where $k = 2\pi/\lambda sp$ and $\lambda sp/2$ is the half wavelength measured between two resonance peaks. Note that the k values are not uniquely defined but have an error range, as the EELS signal is not perfectly periodic.

effects are also shown; clearly, a small systematic shift is observed between the model and experimental dispersions, which may be due to limiting assumptions of the model as well as effects due to shape, size, and composition.[19]

IV. DISCUSSION

To investigate the features observed in the collected spectra and the relation between the optical and energy loss responses, we first performed EELS simulations using the MNPBEM toolbox.[26] The nanowire was modeled as a 1 μm long cylindrical wire with spherical caps at both ends; the wire diameter was set to 100 nm. Values for the silver permittivity were extracted from optical experiments,[27] and the EELS maps and spectra were computed according to the protocol given previously.[28,29]

In Figure 4, the calculated EELS response is shown as a function of distance from the nanowire when the beam is moving in the longitudinal and transverse directions (Figs. 4(a) and 4(b), respectively). The interface between the nanowire and vacuum is again denoted by the white dashed lines. The corresponding spectra for selected impact parameters are also shown in Figs. 4(c) and 4(d). In both cases, a number of peaks associated with Fabry-Perot resonances are observed at lower loss energies (<3 eV), which then merge into a continuum of states around 3.60 eV. Also, in both sets of simulations, a peak is observed at 3.75 eV when the beam is positioned inside the nanowire, which corresponds to excitation of the bulk plasmon for silver. If only the asymptotic SPR peak near 3.60 eV is considered, a higher degree of dispersion was observed in the longitudinal case than in the transversal. This can be seen in the insets of Figs. 4(c) and 4(b), which enlarge this spectral region near the wire surface, as well as in Fig. 4(c) where the peak near 3.6 eV shifts to lower energies when the electron beam moves away from the nanowire. In contrast, the asymptotic peak in the inset of Fig. 4(b) and in Fig. 4(d) shows almost no dispersion whatsoever. Therefore, the experimental and theoretical results show very nice agreement, especially in the asymptotic regime.

However, there are some interesting differences between the acquired spectra and the calculated EELS response. First, in the experimental EELS data, the Fabry-Perot modes are much less distinct than the EELS calculations suggest. This is likely due to the finite energy resolution of the experimental data. Indeed, when the simulated spectra are convolved

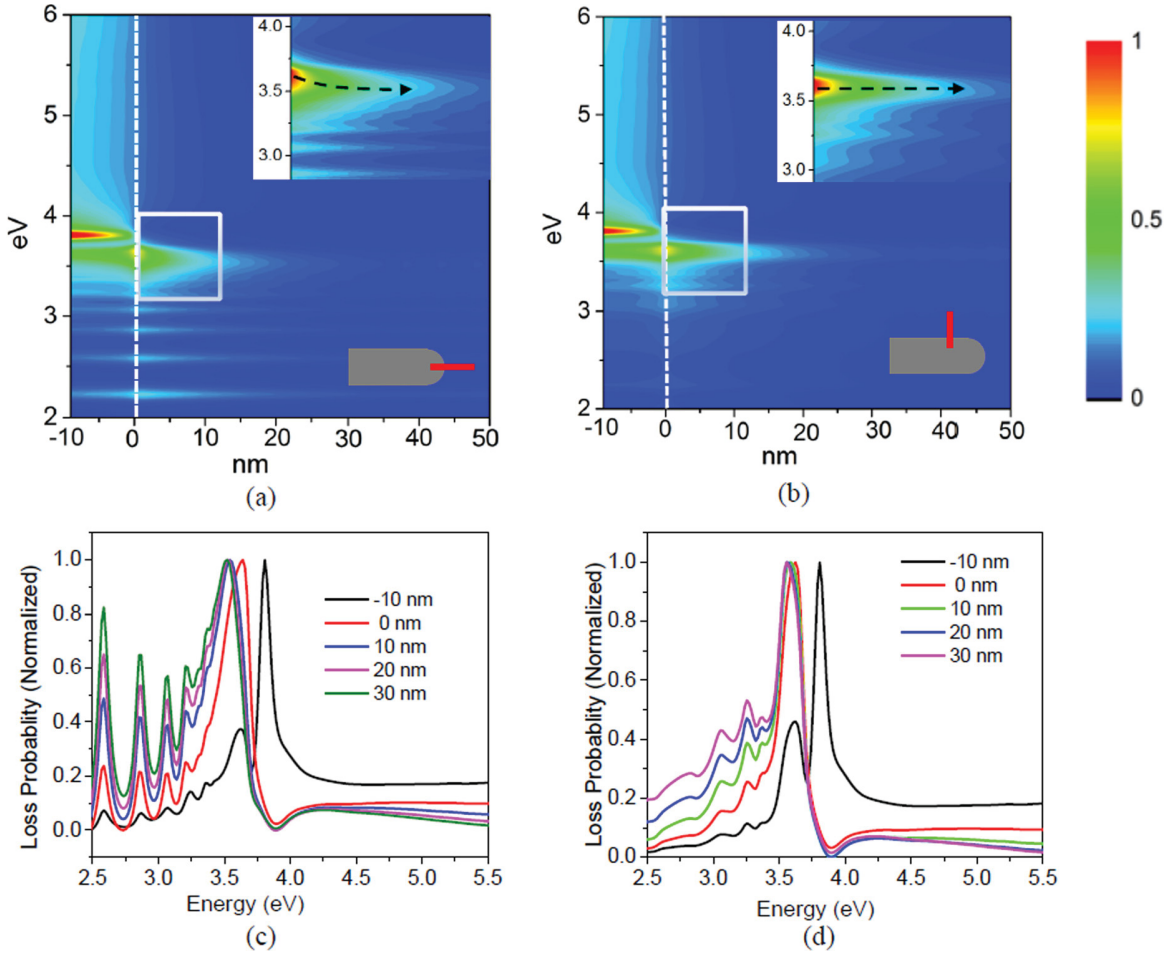

FIG. 4. Simulation results for a cylindrical nanowire of 1 μm length and 100 nm diameter, using the MNPBEM toolbox.[27] Density plot for electron energy loss maps as a function of loss energy and impact parameter along the (a) longitudinal and (b) transversal directions. The insets show a magnified view of the asymptotic regime, marked by the white box. The nanowire boundary at 0 nm is shown by the dashed line. (c) and (d) Corresponding spectra for selected impact parameters.

with a Gaussian function with FWHM = 0.3 eV (shown in Fig. 5), the pronounced peak structure is almost completely indiscernible and the simulated spectra more closely match those acquired experimentally (Figs. 1(b) and 1(d)) quite well. Therefore, the modeled spectra indicate that the origin of the observed spectral asymmetry arises from the contributions of the high-k longitudinal modes on the low energy side of the SPR peak. Another discrepancy is that the bulk peak is less intense in the experimental data and optical excitation calculation than in the EELS simulations. A quantitative explanation of this requires further work but is possible that this effect is due to the attenuation of the electron beam within the metal nanowire, which is not accounted for in the EELS calculations.

While the EELS spectra calculated using the MNPBEM toolbox nicely replicated the spectral shift behavior observed in our experiments, they did not indicate what the origin of this behavior could be. In order to obtain physical insight into the observed plasmonic modes and the relation between the nanoscale optical and EELS responses, we then carried out detailed simulations using energy loss theories and optical models. A theoretical description of the collective electronic excitations at metal surfaces has been presented by Pitarke *et al.*,[25] who predicted that a number of multipolar modes can be excited and contribute to the energy loss of moving electrons. To approximate the nanowires that were examined experimentally, we have considered two distinct geometries. First, a semi-spherical model was used to approximate the tip of the nanowire, although it is apparent from the image in Fig. 1 that the true tip geometry deviates from this simplified geometry. To compare the analytical theory of energy loss with the optical response of this silver nanosphere, we performed numerical simulations using the FDTD Lumerical package, assuming excitation by an optical dipole source at different positions to mimic the electron beam positions. The frequency dependent dielectric function of silver was taken from previously reported optical data.[30]

Figure 6(a) presents a schematic of the silver nanosphere model used to approximate the nanowire tip. The red line in Fig. 6(a) depicts the electron beam traveling at a particular distance, b, from the center of the silver nanosphere. Fig. 6(b) shows the calculated FDTD normalized power flow distribution as a function of distance from a silver nanosphere with diameter of 100 nm. The origin of the x-axis is set in the nanosphere, and the white dashed line at x = 0 denotes the interface between the sphere's surface and vacuum. When the beam is positioned within the sphere, the resonance peak is observed at ≈3.7 eV, which corresponds to the bulk plasmon energy. This peak is stable as the beam moves towards the surface of the sphere. However, when it reaches the interface and progresses away from the sphere, the resonance peak steadily shifts towards ≈3.5 eV. The inset in Fig. 6(b) presents the electric field power flow distribution in the region near the nanowire tip. The black dashed curve with arrow indicates the resonance peak position as the beam moves away from the tip. The spectral shift observed in this simulation agrees quite well with that observed in the experimental EELS data (Figs. 1(a) and 1(c)).

To investigate the origin of this shift, the electron energy-loss probability was also calculated analytically for the spherical model.[25] Fig. 6(c) shows the results of this calculation for several SPR resonance modes: the dipole mode (mode index $\ell = 1$), quadrupole mode ($\ell = 2$), octupole mode ($\ell = 4$), and hexadecapole mode ($\ell = 8$). In this case, the resonance peaks are seen to shift from 3.50 eV for $\ell = 1$ to 3.66 eV for $\ell = 8$. In addition, the higher order modes are noticeably more localized at the surface of the sphere than the lower order modes which extend much further into vacuum. Since the tip of the nanowire analyzed using EELS can be considered pseudo-spherical, these analytical computations suggest that the spectral shift observed in the experimental data (Figs. 1(a) and 1(c)) arises due to the differences in energy-loss probabilities between the lower- and higher-order modes. When the beam is positioned near the nanowire surface, the more localized, higher-order modes contribute more significantly. As the beam moves away from the surface, the energy-loss is

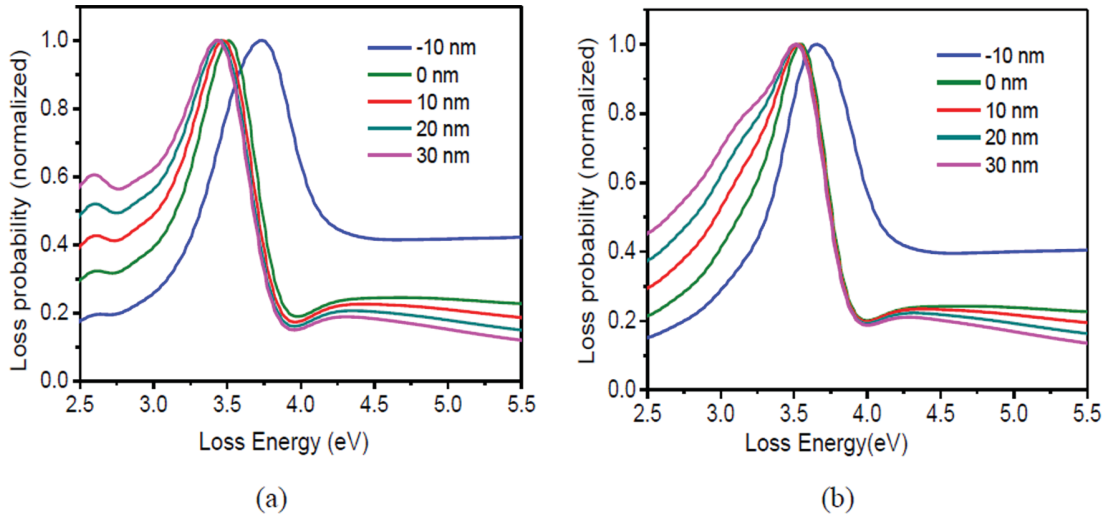

FIG. 5. Simulated spectra from the (a) longitudinal and (b) transversal directions after convolution with a Gaussian function (FWHM = 0.3 eV).

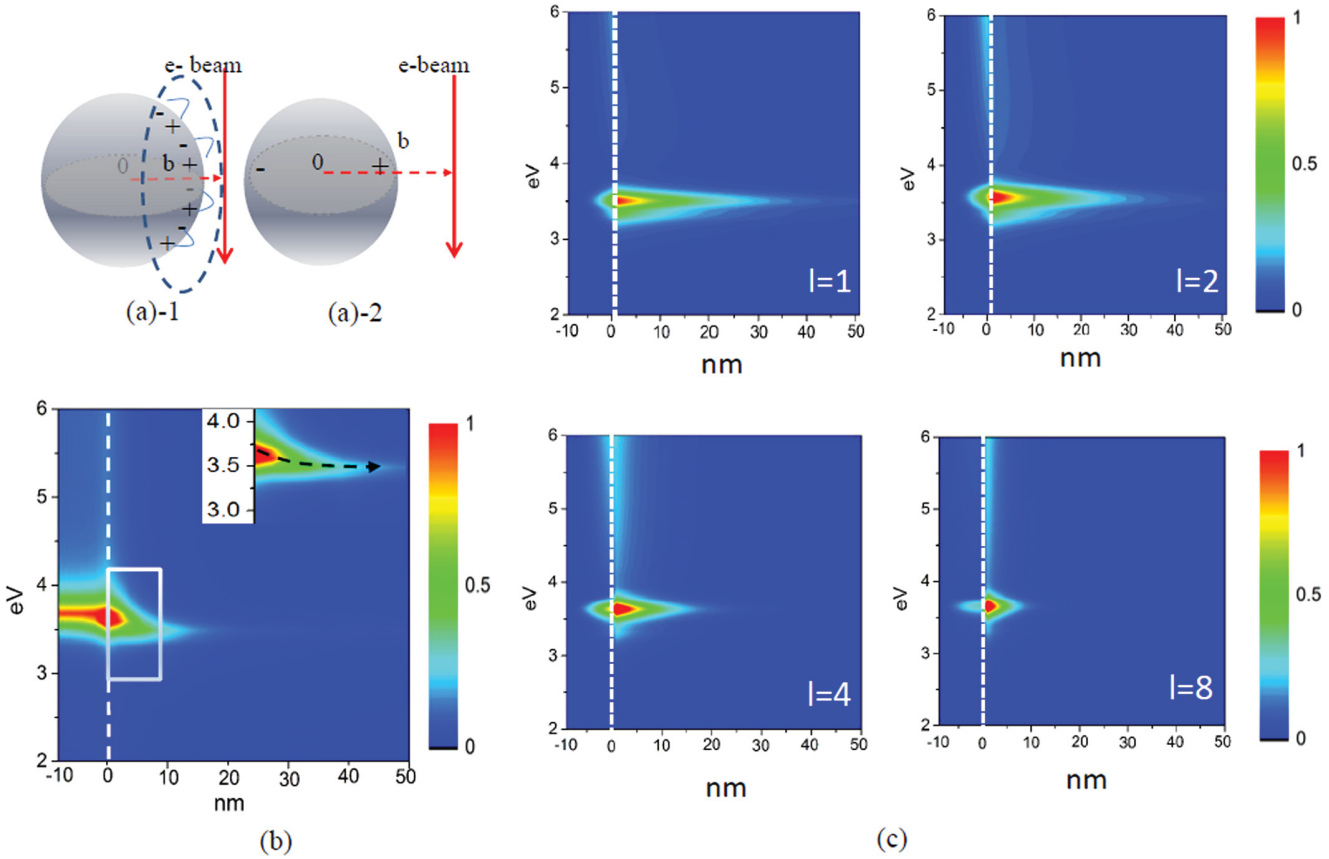

FIG. 6. Results of analytical energy loss and optical simulations for an ideal silver nanosphere. (a) Schematics of the surface charge densities induced by an electron beam (denoted by the red line) placed (a-1) close to the surface of the sphere and (a-2) far away from the surface of the sphere. (b) FDTD simulated power flow intensity distributions as a function of distance from the surface of an ideal silver nanosphere under optical excitation. The position of the surface is indicated by the white dashed line at 0 nm. (c) Analytically computed electron energy loss probabilities from the silver nanosphere for various resonance modes (mode index $\ell = 1$, 2, 4, and 8). Due to the strong variation in maximum energy-loss intensity and for better visibility, the color scale has been scaled independently for all of the images.

dominated by the more delocalized dipole mode resulting in a shift of the observed resonance peak to lower energy-loss. As discussed by Pitarke *et al.*[25] and shown schematically in Fig. 6(a-1), multipolar resonances are readily excited when the beam is near the edge of the sphere since it effectively interacts with a nearly planar surface. In contrast, the dipole resonance will be dominant when the beam is far from the surface of the nanosphere and the impact parameter is large (Fig. 6(b-2)).

To model the EELS response when the beam was positioned along the side of the nanowire, we have performed similar calculations using an infinitely long cylinder geometry.[25] Figure 7(a) shows a schematic of this case where the solid red line represents the electron beam trajectory and the dashed red line indicates its distance, b, from the center of the cylinder. Fig. 7(b) shows the FDTD calculated normalized power flow distribution as a function of radial distance. In contrast to the case of the spherical model, in this case, the power flow shows a single peak at ≈3.6 eV that does not shift as the beam moves away from the cylinder. The inset in Fig. 7(b) depicts the power flow distribution from the region near the edge of the cylinder, and the dashed black line shows a consistent resonance peak that does not shift with excitation position. The observed insensitivity of the peak energy-loss with beam position differs markedly from the calculations for the spherical model but agrees quite well with the experimental EELS data.

Once again, to investigate the origin of these observations, the analytical energy loss probabilities for the various modes ($\ell = 1$–8) were calculated, and the results are presented in Figure 7(c). For all four modes, peaks are observed at ≈3.65 eV and ≈3.3 eV, which are confined near the interface region. For the dipole mode ($\ell = 1$) ,these two peaks exhibit very similar amplitudes. However, as ℓ increases, the higher energy-loss peak becomes progressively more intense relative to the lower energy-loss peak. These results fit quite well with the peak shapes and intensities observed in the experimental EELS spectra collected along the side of the nanowire (Figs. 1(d) and 2(c)), suggesting that the multipolar resonances dominate the SPR response in this case. Finally, despite the differences in amplitude, the peak positions for all four modes do not change as a function of distance from the nanowire surface. This is markedly different from the calculations already discussed for the spherical model but matches the behavior observed in the experimental EELS spectra acquired in the transverse orientation. Therefore, the characteristics of the SPR peak in the two experimental cases we have investigated can be explained by the spatial dependence of the energy-loss probabilities of the various modes excited by the electron beam.

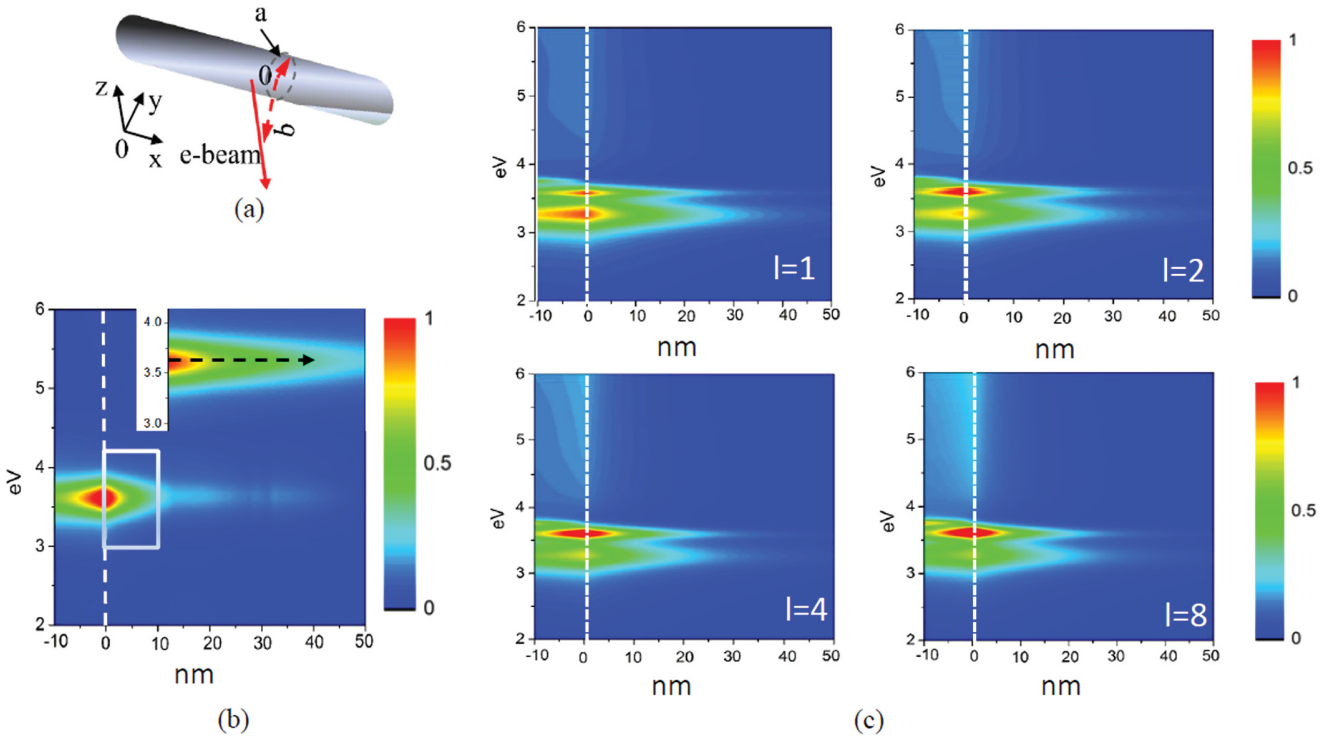

FIG. 7. Results of analytical energy loss and optical simulations for an ideal 100 nm diameter silver nanocylinder. (a) Schematic showing the 100 nm diameter cylinder lying in the (x,y) plane with the electron beam (solid red line) positioned parallel to the z-axis. The dashed red line indicates the distance from the beam to the center of the cylinder. (b) FDTD simulated power flow intensity distributions as a function of distance from surface of the silver nanocylinder under optical excitation. The cylinder surface is indicated by the white dashed line at 0 nm. (c) Analytically computed electron energy loss probabilities from the silver nanocylinder for various resonance modes (mode index $\ell = 1$, 2, 4, and 8). Due to the strong variation in maximum energy-loss intensity and for better visibility, the color scale has been scaled independently for all of the images.

V. CONCLUSIONS

We have explored the detailed spatial dependence of the electron energy loss at optical frequencies when the electron beam is directed near the surface of silver nanowires. Due to the pseudospherical shape of nanowire tip, the detailed loss spectrum near this region depends strongly on the position of the electron beam. Far from the tip, the spectral response is dominated by the dipolar excitation, as predicted theoretically for a spherical geometry. As the beam approaches the tip, the surface of the wire becomes effectively planar, resulting in the excitation of higher-order modes and a shift of the resonance peak towards higher energies. The spectral response was simulated in three ways: (1) using previously published analytical models of energy loss for ideal spheres and infinite wires, (2) by calculating the optical response with dipole optical field excitation, and (3) by simulating the EELS maps using a boundary element method. With the aid of these calculations, it was shown that the spatial variations of the loss peak in the experimental spectra were due to excitation of the more localized higher-order modes when the beam is very close to the nanowire surface. For detailed calculation of the loss spectra and the spatial response profiles, both numerical optical excitation and energy loss simulations showed good agreement with the experimental results. These experiments and calculations demonstrate that the energy loss and optical spectra provide complementary insight into the plasmonic modes of metallic nanostructures.

ACKNOWLEDGMENTS

This work was supported by the Center for Photonic and Multiscale Nanomaterials (C-PHOM) funded by the National Science Foundation Materials Research Science and Engineering Center program DMR 1120923.

This material is also based upon work partially supported by the Center for Solar and Thermal Energy Conversion, an Energy Frontier Research Center funded by the U.S. Department of Energy, Office of Science, Office of Basic Energy Sciences under Award No. #DE-SC0000957 used to purchase materials for NP and nanowire synthesis.

The portion of the work at Karl-Franzens-Universität Graz has been supported by the Austrian Science Fund FWF under Project P24511-N26 and the SFB NextLite.

[1]Y. G. Sun and Y. N. Xia, Science **298**(5601), 2176–2179 (2002).
[2]I. Washio, Y. J. Xiong, Y. D. Yin, and Y. N. Xia, Adv. Mater. **18**(13), 1745–1749 (2006).
[3]T. K. Sau and C. J. Murphy, Langmuir **20**, 6414 (2004).
[4]M. N'Gom, J. Ringnalda, J. F. Mansfield, A. Agarwal, N. Kotov, N. J. Zaluzec, and T. B. Norris, Nano Lett. **8**, 3200 (2008).
[5]M. N'Gom, T. B. Norris, and R. Erni, in *Conference on Lasers and Electro-Optics and 2009 Conference on Quantum Electronics and Laser Science Conference, Baltimore, MD, USA, 31 May–5 June 2009* (IEEE, New York, 2009), pp. 3228–3229.
[6]L. Novotny, Phys. Rev. Lett. **98**, 266802 (2007).
[7]E. R. Encina, E. A. Perassi, and E. A. Coronado, J. Phys. Chem. A **113**, 4489 (2009).
[8]E. J. R. Vesseur, R. de Waele, M. Kuttge, and A. Polman, Nano Lett. **7**, 2843 (2007).

[9]F. J. Garcia de Abajo and M. Kociak, Phys. Rev. Lett. **100**, 106804 (2008).
[10]J. Nelayah, M. Kociak, O. Stephan, F. J. G. de Abajo, M. Tence, L. Henrard, D. Taverna, I. Pastoriza-Santos, L. M. Liz-Marzan, and C. Colliex, Nat. Phys. **3**, 348 (2007).
[11]P. E. Batson, N. Dellby, and O. L. Krivanek, Nature **418**, 617 (2002).
[12]P. M. Echenique and J. B. Pendry, J. Phys. C: Solid State Phys. **11**, 2065 (1978).
[13]M. V. Bashevoy, F. Jonsson, A. V. Krasavin, N. I. Zheludev, Y. Chen, and M. I. Stockman, Nano Lett. **6**, 1113 (2006).
[14]R. H. Ritchie, Surf. Sci. **34**, 1 (1973).
[15]M. Rocca, Surf. Sci. Rep. **22**, 1 (1995).
[16]T. L. Ferrell and P. M. Echenique, Phys. Rev. Lett. **55**, 1526 (1985).
[17]O. Nicoletti, M. Wubs, N. A. Mortensen, W. Sigle, P. A. van Aken, and P. A. Midgley, Opt. Express **19**, 15371 (2011).
[18]D. Rossouw, M. Couillard, J. Vickery, E. Kumacheva, and G. A. Botton, Nano Lett. **11**, 1499 (2011).
[19]D. Rossouw and G. A. Botton, Phys. Rev. Lett. **110**, 066801 (2013).
[20]K. E. Korte, S. E. Skrabalak, and Y. N. Xia, J. Mater. Chem. **18**, 437 (2008).
[21]P. Andrew and A. Ilie, J. Phys.: Conf. Ser. **61**, 36 (2007).
[22]C. J. Rossouw, L. J. Allen, S. D. Findlay, and M. P. Oxley, Ultramicroscopy **96**, 299 (2003).
[23]A. L. Koh, D. W. McComb, S. A. Maier, H. Y. Low, and J. K. W. Yang, J. Vac. Sci. Technol., B **28**, C6O45 (2010).
[24]R. H. Ritchie, Phys. Rev. **106**, 874 (1957).
[25]J. M. Pitarke, V. M. Silkin, E. V. Chulkov, and P. M. Echenique, Rep. Prog. Phys. **70**, 1 (2007).
[26]U. Hohenester and A. Trugler, Comput. Phys. Commun. **183**, 370 (2012).
[27]E. D. Palik, *Handbook of Optical Constants of Solids* (Academic, Orlando, 1985).
[28]U. Hohenester, Comput. Phys. Commun. **185**, 1177 (2014).
[29]F. J. Garcia de Abajo, Rev. Mod. Phys. **82**, 209 (2010).
[30]P. B. Johnson and R. W. Christy, Phys. Rev. B **6**, 4370 (1972).
[31]Commercial equipment, instruments, and materials or software is identified in this report to specify adequately the experimental procedure. Such identification does not imply recommendation or endorsement of these items by the NIST nor does it imply that they are the best available for the purpose.

6 Paper 3: Full Three-Dimensional Reconstruction of the Dyadic Green Tensor from Electron Energy Loss Spectroscopy of Plasmonic Nanoparticles

Published in: ACS Photonics (2015)

ACS Photonics

Article

pubs.acs.org/journal/apchd5

Full Three-Dimensonal Reconstruction of the Dyadic Green Tensor from Electron Energy Loss Spectroscopy of Plasmonic Nanoparticles

Anton Hörl, Andreas Trügler, and Ulrich Hohenester*

Institute of Physics, University of Graz, Universitätsplatz 5, 8010 Graz, Austria

ABSTRACT: Electron energy loss spectroscopy (EELS) has emerged as a powerful tool for the investigation of plasmonic nanoparticles, but the interpretation of EELS results in terms of optical quantities, such as the photonic local density of states, remains challenging. Recent work has demonstrated that, under restrictive assumptions, including the applicability of the quasistatic approximation and a plasmonic response governed by a single mode, one can rephrase EELS as a tomography scheme for the reconstruction of plasmonic eigenmodes. In this paper we lift these restrictions by formulating EELS as an inverse problem and show that the complete dyadic Green tensor can be reconstructed for plasmonic particles of arbitrary shape. The key steps underlying our approach are a generic singular value decomposition of the dyadic Green tensor and a compressed sensing optimization for the determination of the expansion coefficients. We demonstrate the applicability of our scheme for prototypical nanorod, bowtie, and cube geometries.

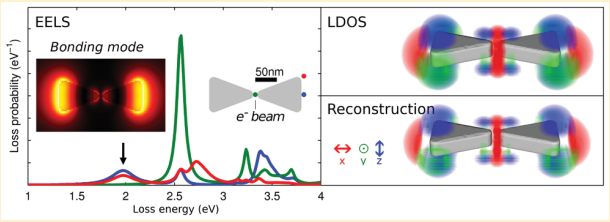

KEYWORDS: *plasmonics, electron energy loss spectroscopy, tomography, compressed sensing*

Electron energy loss spectroscopy (EELS) is a powerful tool for the investigation of plasmonic nanoparticles.[1,2] EELS is a technique based on electron microscopy and measures the probability of a swift electron to lose part of its kinetic energy through plasmon excitation as a function of electron beam position. Following first proof of principle experiments,[3,4] in the last couple of years EELS has been exhaustively used for the investigation of plasmon modes in single and coupled nanoparticles.

Despite its success, the interpretation of EELS data in terms of optical quantities, such as the photonic local density of states[5] (LDOS), remains challenging.[6,7] To overcome this problem, in ref 8 we formulated EELS as a tomography scheme[9] and showed that under certain assumptions a collection of EELS maps can be used to reconstruct the three-dimensional mode profile of plasmonic nanoparticles. A similar approach was presented independently by Nicoletti and co-workers,[10] who demonstrated the applicability of the scheme for a silver nanocube. Extracting three-dimensional information through sample tilting was also shown for a split-ring resonator[11] and a nanocrescent using cathodoluminescence imaging.[12]

The problem with EELS tomography is that the measurement signal (the loss probability) is not simply the integral of local losses along the electron trajectory but involves a two-step process where the swift electron first excites a particle plasmon and then performs work against the induced particle plasmon field. This leads to a nonlocal response function, which allows for a tomographic reconstruction only under restrictive assumptions, such as the applicability of the quasistatic approximation or a plasmonic response governed by a single mode. In this paper we use additional preknowledge, namely, that the particle plasmon fields are solutions of Maxwell's equations and that the dyadic Green tensor[5] can be decomposed into modes, in order to rephrase EELS in terms of an inverse problem. We develop a rather generic model for the EELS probabilities, which depends on a few parameters, and determine the parameters such that the model data match as closely as possible the measured data. Within this approach we are able to obtain the most accurate reconstructions of the dyadic Green tensor, which, in turn, allows us to extract the three-dimensional photonic LDOS from a collection of tilted EELS maps. We demonstrate the applicability of our scheme for prototypical nanorod, bowtie, and cube geometries.

THEORY

We start by analyzing EELS within a semiclassical framework,[1] where a swift electron propagating with velocity $\boldsymbol{v}$ loses a tiny part of its kinetic energy by performing work against the electric field $\mathbf{E}[\mathbf{r}_e(t)]$ produced by itself. For sufficiently large velocities, we can ignore velocity changes in the electron trajectory $\mathbf{r}_e(t) \approx \mathbf{R}_0 + \mathbf{v}t$, with $\mathbf{R}_0$ being the impact parameter. It is convenient to split $\mathbf{E} = \mathbf{E}_{\mathrm{bulk}} + \mathbf{E}_{\mathrm{surf}}$ into a bulk contribution[13] $\mathbf{E}_{\mathrm{bulk}}$, corresponding to the electric field within an unbounded homogeneous medium, and a surface contribution $\mathbf{E}_{\mathrm{surf}}$, corresponding to field modifications (including surface plasmons) from the interfaces between different materials. Bulk losses are due to Cherenkov radiation and electronic excitations,[1] and the loss probability is obtained by simply multiplying the loss probability per unit length $\gamma_{\mathrm{bulk}}'(\omega)$, inside

Received: May 18, 2015
Published: September 4, 2015

DOI: 10.1021/acsphotonics.5b00256
ACS Photonics 2015, 2, 1429−1435

material j and for loss energy $\hbar\omega$, with the path length l_j of the electron inside material j,

$$\Gamma_{\text{bulk}}(\omega) = \sum_j \gamma^j_{\text{bulk}}(\omega) l_j \tag{1}$$

Bulk losses can be interpreted in terms of local scatterings where the electron emits a photon or excites electrons in the dielectric material and loses part of its kinetic energies. To compute the surface loss probability, we integrate the work $dW = e\mathbf{E}_{\text{surf}}\cdot\mathbf{v}dt$ performed by the electron over the entire trajectory and decompose it into the different loss energies $\hbar\omega$ according to

$$W = e\int_{-\infty}^{\infty} \mathbf{v}\cdot\mathbf{E}_{\text{surf}}[\mathbf{r}_e(t)]dt = \int_0^{\infty} \hbar\omega\Gamma_{\text{surf}}(\omega)d\omega \tag{2}$$

Thus, the energy loss probability becomes[1]

$$\Gamma_{\text{surf}}(\mathbf{R}_{\hat{\mathbf{v}}}, \omega) = \frac{e}{\pi\hbar\omega}\int_{-\infty}^{\infty} \text{Re}\{e^{-i\omega t}\mathbf{v}\cdot\mathbf{E}_{\text{surf}}[\mathbf{r}_e(t), \omega]\}dt \tag{3}$$

where we have explicitly indicated the dependence on the electron propagation direction and the impact parameter through $\mathbf{R}_{\hat{\mathbf{v}}} = (\hat{\mathbf{v}},\mathbf{R}_0)$. To understand the physical process underlying eq 3, it is convenient to introduce the current distribution $\mathbf{J}(\mathbf{r},t) = -ev\delta(\mathbf{r} - \mathbf{r}_e(t))$ of the swift electron and the dyadic Green tensor[5] $\mathbf{G}(\mathbf{r},\mathbf{r}',\omega)$ that relates for a given frequency ω a current source at position $\mathbf{r}'$ to an electric field at position $\mathbf{r}$ via $\mathbf{E}(\mathbf{r},\omega) = i\omega\mu_0\mathbf{G}(\mathbf{r},\mathbf{r}',\omega)\cdot\mathbf{J}(\mathbf{r}',\omega)$. The loss probability of eq 3 can then be rewritten in the form

$$\Gamma_{\text{surf}}(\mathbf{R}_{\hat{\mathbf{v}}}, \omega) = \frac{\mu_0}{\pi\hbar}\int \text{Im}\{\mathbf{J}^*(\mathbf{r}, \omega)\cdot\mathbf{G}(\mathbf{r}, \mathbf{r}', \omega)\cdot\mathbf{J}(\mathbf{r}', \omega)\}d\mathbf{r}d\mathbf{r}' \tag{4}$$

where $d\mathbf{r}$ denotes integration over the spatial variable $\mathbf{r}$. Contrary to eq 1, the above expression describes a genuinely nonlocal self-interaction process where the electron first induces a field (through excitation of a surface plasmon) and then performs work against the induced field.

In ref 6, the authors tried to interpret eq 4 in terms of the photonic local density of states[5] (LDOS)

$$\rho_{\hat{\mathbf{n}}}(\mathbf{r}, \omega) = \frac{6\omega}{\pi\omega^2}\text{Im}\{\hat{\mathbf{n}}^*\cdot\mathbf{G}(\mathbf{r}, \mathbf{r}, \omega)\cdot\hat{\mathbf{n}}\} \tag{5}$$

which is of paramount importance in the field of nanooptics and describes how the decay rate of a quantum emitter located at position $\mathbf{r}$ and with dipole moment oriented along $\hat{\mathbf{n}}$ becomes modified in the presence of a structured dielectric environment. While such interpretation can be formally established for nanostructures with translational symmetry along one spatial dimension, it becomes problematic for nanoparticles with generic shape.[7]

A different interpretation of eq 4 in terms of a tomography scheme was formulated independently in refs 8 and 10. As a preliminary step, let us consider the bulk losses of eq 1 for a given $\mathbf{R}_{\hat{\mathbf{v}}}$ value. Then, each point $\mathbf{r}$ inside a medium j contributes with γ^j_{bulk} to the total loss rate. Within the field of tomography[9] it is well-known that the three-dimensional profile of $\gamma_{\text{bulk}}(\mathbf{r})$ can be uniquely reconstructed from a *sinogram*, where bulk losses are recorded for all possible propagation directions $\hat{\mathbf{v}}$, using the inverse Radon transform. Such tomography reconstruction is significantly more complicated for the surface losses of eq 4 since Γ_{surf} is not the sum of local losses (as in the bulk case) but governed by the self-interaction process of excitation and back-action. Only for certain, rather restrictive simplifications, a viable tomography scheme can be formulated:[8,10] the nanoparticles must be small enough such that the quasistatic approximation can be employed; the plasmonic response must be governed by a single plasmonic eigenmode; the sinogram must only consist of electron trajectories that do not penetrate the particle; the sign of the eigenmode potentials must be unique. Although it has been demonstrated that reconstruction is possible in certain cases,[8,10] it is obvious that the above restrictions provide a serious bottleneck for general plasmon field tomography.

In this paper we formulate a significantly more general scheme, which approaches the reconstruction as an *inverse problem* rather than a tomography scheme. We first describe our approach and discuss possible problems and generalizations at the end. First, we decompose the dyadic Green tensor into a number of modes $\mathbf{E}_k(\mathbf{r},\omega)$

$$\mathbf{G}(\mathbf{r}, \mathbf{r}', \omega) \approx \sum_{k=1}^{n} C_k\mathbf{E}_k(\mathbf{r}, \omega) \otimes \mathbf{E}_k(\mathbf{r}', \omega) \tag{6}$$

where C_k controls how much the different modes contribute to the decomposition. In the following we only consider positions $\mathbf{r}$ and $\mathbf{r}'$ outside the plasmonic nanoparticle and assume that $\mathbf{E}_k(\mathbf{r},\omega)$ is a solution of Maxwell's equations. The expansion of eq 6 is generally possible because $\mathbf{G}$ is a symmetric matrix that can be submitted to a singular value decomposition, with C_k being the singular values and $\mathbf{E}_k$ being the orthogonal matrices. In this respect, eq 6 is similar to a wave function expansion in quantum mechanics into a complete set of basis functions.

To be useful as a reconstruction scheme the modes $\mathbf{E}_k(\mathbf{r},\omega)$ should be sufficiently well adapted to the problem such that a limited number n suffices for a suitable representation of $\mathbf{G}(\mathbf{r},\mathbf{r}',\omega)$. Possible modes are quasi normal modes of the plasmonic nanoparticles,[14−17] which have recently received considerable interest, or natural oscillation modes of our boundary element method approach (see Methods). With these modes, the surface losses of eq 4 become

$$\tilde{\Gamma}_{\text{surf}}(\mathbf{R}_{\hat{\mathbf{v}}}, \omega) \approx \frac{\mu_0 e^2}{\pi\hbar}\sum_{k=1}^{n} \text{Im}\{C_k A^+(\mathbf{R}_{\hat{\mathbf{v}}}, \omega)A^-(\mathbf{R}_{\hat{\mathbf{v}}}, \omega)\} \tag{7}$$

where $A_k^{\pm}(\mathbf{R}_{\hat{\mathbf{v}}},\omega) = \int_{-\infty}^{\infty} e^{\pm i\omega z/v}\ \hat{\mathbf{v}}\cdot\mathbf{E}_k(\mathbf{R}_0 + \hat{\mathbf{v}}z,\omega)dz$ is the averaged mode profile along the electron propagation direction. We can now formulate our inverse problem as follows. Suppose that one has measured EELS spectra Γ_{exp} for a given loss energy and for various impact parameters and electron propagation directions. We then determine the coefficients C_k such that the entity of measurement data differs as little as possible from the model data of eq 7,

$$\min_{C_k} \frac{1}{2}\left\|\Gamma_{\text{exp}}(\mathbf{R}_{\hat{\mathbf{v}}}, \omega) - \tilde{\Gamma}_{\text{surf}}(\mathbf{R}_{\hat{\mathbf{v}}}, \omega)\right\|^2_{L_2} \tag{8}$$

resulting in a least-squares optimization (we adopt the norm definitions $\|\mathbf{x}\|^2_{L_2} = \sum_i |x_i|^2$ and $\|\mathbf{x}\|_{L_1} = \sum_i |x_i|$). Alternatively, in this work we will use a compressed sensing optimization[18,19]

$$\min_{C_k}\left[\|C_k\|_{L_1} + \frac{1}{2\mu}\left\|\Gamma_{\text{exp}}(\mathbf{R}_{\hat{\mathbf{v}}}, \omega) - \tilde{\Gamma}_{\text{surf}}(\mathbf{R}_{\hat{\mathbf{v}}}, \omega)\right\|^2_{L_2}\right] \tag{9}$$

which attempts to minimize the moduli of the expansion coefficients, therefore the scheme is often referred to as a L_1-

DOI: 10.1021/acsphotonics.5b00256
ACS Photonics 2015, 2, 1429−1435

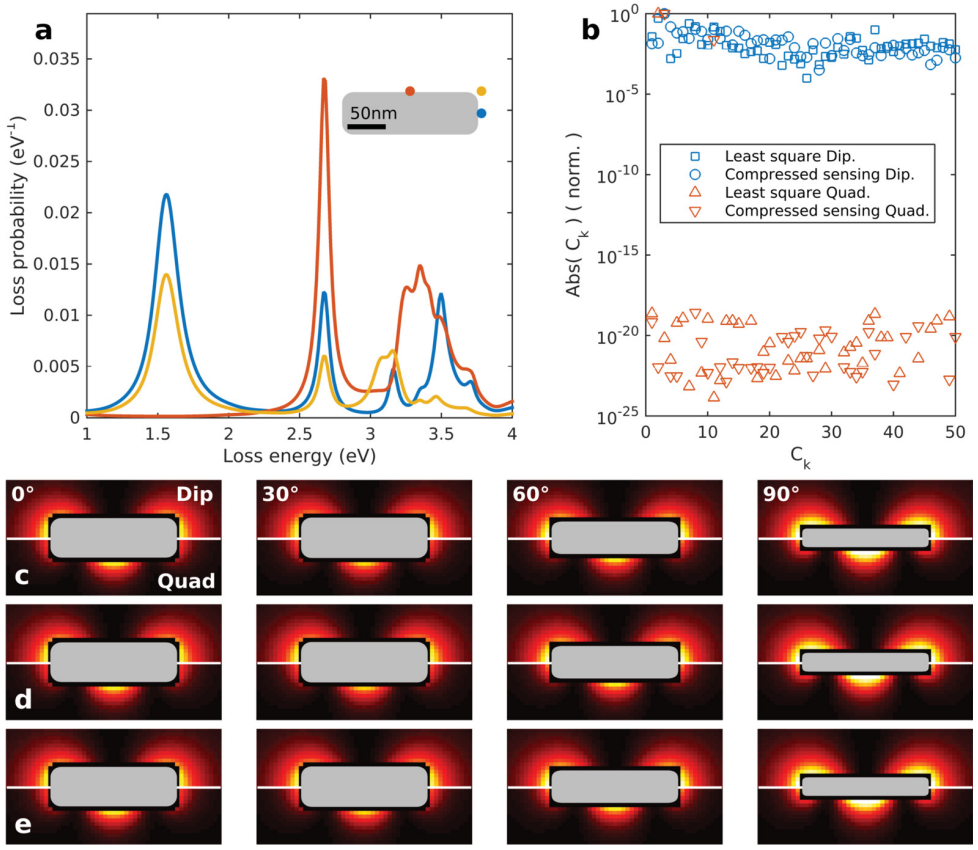

Figure 1. EELS spectra and maps for a silver nanorod. (a) EELS spectra recorded at the positions indicated in the inset. The peaks at approximately 1.5 and 2.7 eV are attributed to the dipole and quadrupole plasmon mode. (b) Mode decomposition of the dipole and quadrupole mode from the collection of rotated EELS maps, using either the least-squares minimization of eq 8 or the compressed sensing optimization of eq 9. For each mode, the coefficients C_k are normalized to unity. (c) Selected EELS maps for dipole (upper part) and quadrupole (lower part) mode and for different electron propagation directions (rotation angles), as computed with the MNPBEM toolbox.[20,21] (d) Back projected EELS maps for the C_k distribution obtained from the compressed sensing optimization, using eq 6 for the Green function decomposition and eq 4 for the calculation of the loss probabilities. (e) Same as panel (d) but for C_k distribution obtained from the least-squares optimization.

optimization, and μ is a parameter that allows to switch between genuine compressed sensing and least-squares optimizations.[19] For a sufficiently small number of expansion modes $\mathbf{E}_k$, the determination of the expansion coefficients C_k is a highly overdetermined problem since the measured loss data can be assembled for many propagation directions and impact parameters $\mathbf{R}_{\hat{\mathbf{v}}}$. The only preknowledge entering our optimization is the self-interaction-type scattering process of the electron loss, eq 4, and the assumption that the dynamics of the electric fields outside the plasmonic nanoparticles is governed by Maxwell's equations. Importantly, once the coefficients C_k are determined, we have (approximately) reconstructed the dyadic Green tensor of eq 6, which allows us to compute all electrodynamic properties including the photonic LDOS.

RESULTS

To prove the applicability of our reconstruction scheme, we generate the "experimental" EELS data Γ_{exp} using the simulation toolbox MNPBEM for plasmonic nanoparticles.[20,21] We first consider a silver nanorod with dimensions 200 × 65 × 30 nm^3 and compute the loss spectra for the three selected impact parameters indicated in Figure 1a. The two prominent loss peaks at low energies can be attributed to the dipole and quadrupole plasmon modes. Corresponding EELS maps at the resonance frequencies are shown for a few selected electron propagation directions (rotation angles) in Figure 1c. The mode profiles are reminiscent of the dipole and quadrupole surface charge distributions.[8] For the decomposition of eq 6 into modes $\mathbf{E}_k(\mathbf{r},\omega)$, we use the information about the nanoparticle shape, which in experiment can be obtained from additional high-angle annular dark-field (HAADF) data[22,23] and compute the 50 natural oscillation modes of lowest energy (see Methods). Figure 1b shows the modulus of coefficients C_k obtained from either a compressed sensing or least-squares optimization. Although the two approaches give quite different C_k distributions, the back-projected EELS maps, obtained by assembling the dyadic Green tensor using eq 6 and computing $\tilde{\Gamma}_{\text{surf}}$ from eq 4, both are in almost perfect agreement with the original Γ_{exp} maps.

Having obtained the C_k values from the optimizations of eqs 8 and 9, we can use eq 6 to approximately reconstruct the dyadic Green tensor, which allows us to compute any electrodynamic response function for the plasmonic nanorod. In the following we consider the projected photonic LDOS of eq 5. Figure 2 shows the true and reconstructed LDOS maps and compares the quality of compressed sensing and least-squares optimizations. In particular, the inspection of panels

DOI: 10.1021/acsphotonics.5b00256
ACS Photonics 2015, 2, 1429−1435

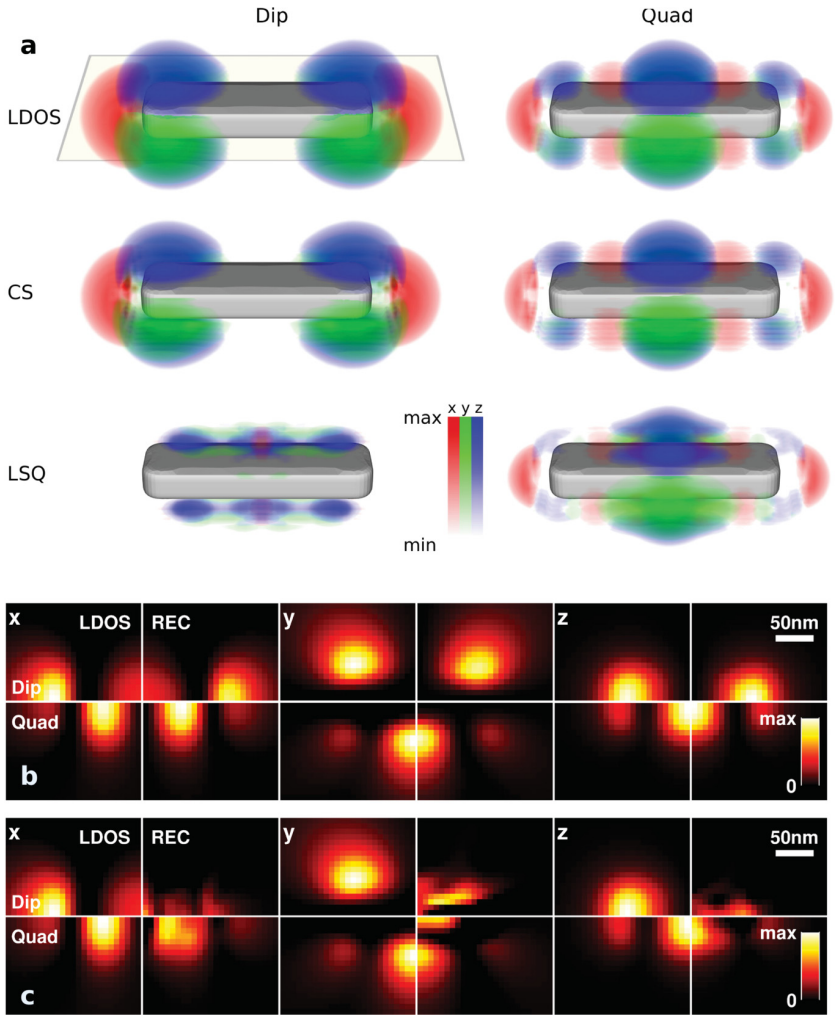

Figure 2. Photonic LDOS of eq 5 and reconstructed LDOS. (a) Three-dimensional LDOS distribution, as computed with the MNPBEM toolbox (LDOS),[20] and the distributions reconstructed from the compressed sensing (CS) and least-squares (LSQ) optimizations. The projected LDOS $\rho_{\hat{\mathbf{n}}}(\mathbf{r},\omega)$ is shown for different projection directions $\hat{\mathbf{n}} = \hat{\mathbf{x}},\hat{\mathbf{y}},\hat{\mathbf{z}}$. (b) LDOS density map in a plane 20 nm above the nanoparticle, as reconstructed from the compressed sensing optimization. The lower (upper) part of each panel shows the dipole (quadrupole) mode, the left (right) part shows the true (reconstructed) LDOS. (c) Same as panel (b) but for least-squares optimization. The reconstructed least-squares LDOS has also negative contributions, which are set to zero for clarity.

(b) and (c), which report the LDOS in a plane 20 nm above the nanorod, reveals that the compressed sensing results are in very good agreement with the true LDOS values, whereas the least-squares optimization completely fails to provide even qualitative agreement. This finding seems at first sight surprising since both optimization approaches were previously capable of reconstructing the experimental EELS data almost perfectly, as shown Figure 1c–e. We attribute the least-squares shortcoming to the fact that the EELS loss of eq 4 is governed by the long-range tails of the particle plasmon field distributions, with which the passing electron predominantly interacts, whereas the LDOS of eq 5 is governed by the short-range evanescent field components. Thus, when the optimization has no strong bias on the C_k determination, it comes up with the proper long-range components, resulting in high-quality EELS maps shown in Figure 1e, but fails for the short-range components, which contribute little to the minimization function of eq 8. In contrast, the compressed sensing optimization of eq 9 seeks for a C_k distribution with as few nonzero components as possible. For suitable basis functions $\mathbf{E}_k$, this bias helps to properly select those modes that contribute little but still noticeably to the loss probability of eq 4. We emphasize that such a bias for selecting a sparse expansion distribution is by no means unique to the problem of our present concern, but has been previously highlighted in various studies, for example, in the context of plasmon tomography[10] or single-pixel cameras,[24] and lies at the heart of the compressed sensing algorithm.

An advantage of compressed sensing is that the reconstruction can, in general, be performed, even with a very limited amount of measurement data, and the quality of the reconstructed data is usually not strongly affected by noise.[18] In Figure 3 we show reconstructed EELS and LDOS maps for the small number of impact parameters and rotation angles shown in the first row of measurement data. As can be seen, the quality of the reconstructed data is extremely good, despite the limited amount of measurement data. This might be beneficial for EELS experiments that typically suffer from a limited

DOI: 10.1021/acsphotonics.5b00256
ACS Photonics 2015, 2, 1429–1435

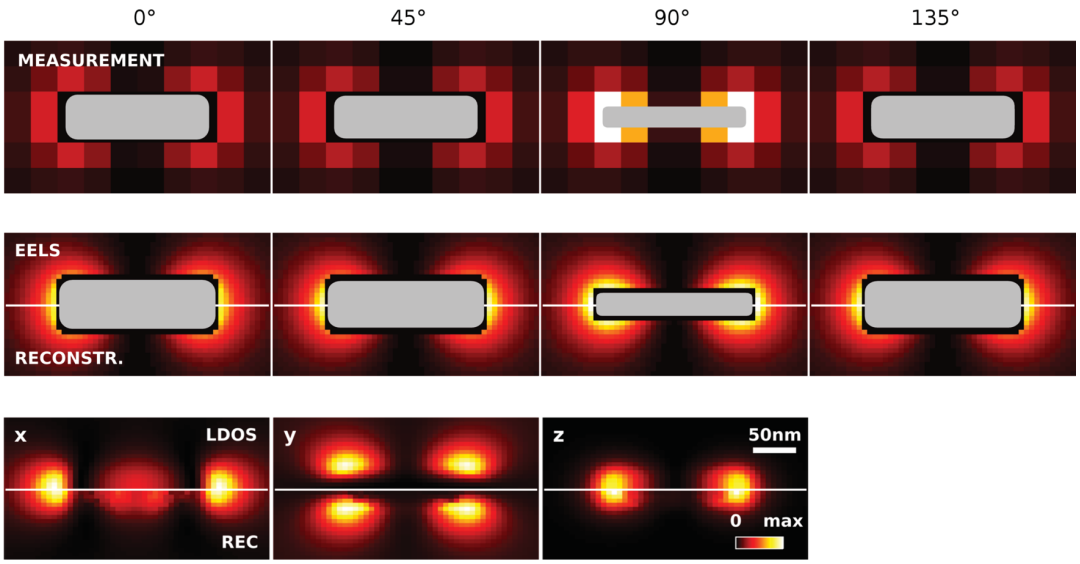

Figure 3. Compressed sensing reconstruction for a strongly reduced number of measurement points. The first row shows the measurement data for a few rotation angles. In the second row we compare the EELS data for a finer sampling mesh (upper part of panel) with the reconstructed signal (lower part), finding almost perfect agreement. The last row reports the true (upper part of panel) and reconstructed (lower part) LDOS maps in a plane 20 nm above the nanorod.

amount of rotation angles (missing wedge problem) and where the number of measurement points is often kept low to avoid sample contamination.

Finally, in Figure 4 we compare LDOS maps with reconstructed maps for (a,b) a bowtie nanoparticle and (c,d) a cube. For the bowtie geometry, we show the LDOS for the two plasmon modes of lowest energy, which can be labeled as bonding and antibonding according to the parallel and antiparallel orientation of the dipole moments of the individual nanotriangles.[25] The agreement between the true and reconstructed LDOS maps is very good; in particular, one can clearly observe the strongly increased LDOS enhancement in the gap region. For the cube, we show the dipole and corner modes of lowest energy,[10] finding fair agreement between the true and the reconstructed LDOS maps. We attribute the small differences to problems of our algorithm when dealing with degenerate modes of symmetric particles, which might be improved by explicitly accounting for mode symmetries.[26]

SUMMARY AND DISCUSSION

To summarize, we have shown how to extract the dyadic Green tensor of Maxwell's theory from a collection of EELS maps recorded for different electron propagation directions (rotation angles). Our reconstruction scheme is based on a singular-value decomposition of the Green tensor and a compressed-sensing optimization for the expansion coefficients. We have demonstrated the applicability of our approach for various elementary nanoparticle shapes. We foresee several improvements for plasmon tomography based on EELS. On the experimental side, electron holography[22] can provide additional information and could allow to disentangle the excitation and measurement channels of plasmonic EELS. On the theoretical side, the presented reconstruction scheme works surprisingly well for most nanoparticle geometries, but further work is needed to clarify the role of various ingredients.

First, there are several possibilities for choosing the basis functions for the decomposition of the dyadic Green tensor, eq 6. In this work we have chosen biorthogonal "constant flux states"[27] that are the eigenstates of the Green function evaluated for real frequencies (see Methods). They have the advantage that they can be computed rather straightforwardly, even in the case of degenerate or near-degenerate modes; on the other hand, they have to be computed for each loss energy separately, and several of these modes can govern the plasmonic response. Another possibility for a basis are the quasi normal modes evaluated at the poles of the Green function in complex frequency space.[14−17] The computation of these modes requires an iterative solution scheme,[17] however, once they are computed, they can be used for a large frequency range, and in general, the plasmonic response is only governed by very few of these modes.

In this work we have considered the situation where the basis is already computed for the true nanoparticle shape and have shown that even in this case the EELS tomography scheme can be quite tricky. However, our approach is less restrictive than it may appear: in principle, for electron beams not penetrating the nanoparticle, any basis with modes being solutions of the free-space Maxwell's equations can be employed. Thus, even if a slightly different particle shape or dielectric material is considered in the computation of the basis, this will not necessarily degrade the quality of the reconstruction. In this case, it might be beneficial to adapt our approach such that (i) the modes for the Green function decomposition are expanded in a given nonideal basis and (ii) the compressed sensing algorithm seeks for a minimum number of decomposition modes. Here it might be advantageous to use quasi normal modes, because the same few modes could be optimized for a whole range of loss energies, thus, imposing stronger restrictions in comparison to an independent optimization at individual loss energies.

Although further work is needed to establish EELS tomography of plasmonic nanoparticles as a robust and out-of-the-box scheme, we believe that our present work provides an important step forward for reconstructing electrodynamic quantities from EELS measurements and makes significant

DOI: 10.1021/acsphotonics.5b00256
ACS Photonics 2015, 2, 1429−1435

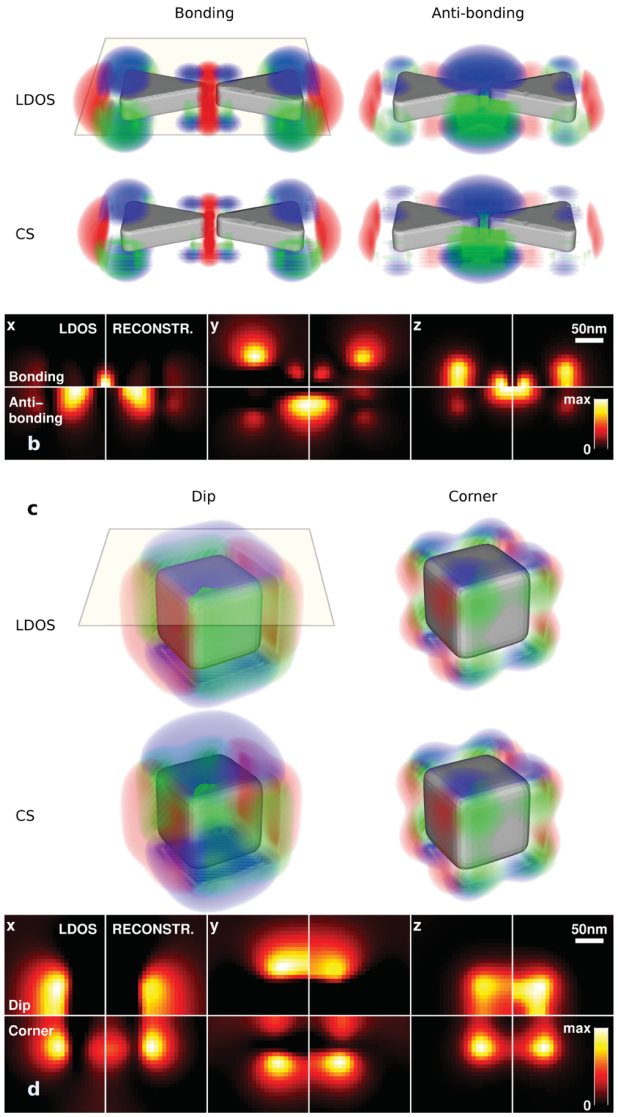

Figure 4. (a) True (upper row) and reconstructed (lower row) LDOS for a bowtie geometry (total size 215 × 85 × 30 nm^3 and 10 nm gap) and for the bonding and antibonding modes of lowest energy. Color code is identical to Figure 2. (b) Density map of LDOS in a plane 20 nm above the bowtie structure. (c) True (left) and reconstructed (right) LDOS for a cube with 150 nm side length and for the dipole and corner modes of lowest energy.[10] (d) Density map of LDOS in a plane 30 nm above the cube.

progress with respect to the recently developed tomography schemes that were bound to quasistatic approximation and other restrictive assumptions.

METHODS

Simulations. In our simulation approach, we compute the LDOS and EELS spectra using the MNPBEM toolbox[20,21] and a silver dielectric function extracted from optical experiments.[28]

Mode Decomposition. For the mode decomposition of eq 6, we follow the prescription of García de Abajo et al.[29] and compute the natural oscillation modes through diagonalization of the Σ matrix, see eq 21 of ref 29 for details, keeping for the solution of the inverse problem the 50 modes of lowest energy. A higher number of modes did not show a significant improvement in the reconstruction results. For our mode decomposition it turns out to be convenient to use a biorthogonal basis, similarly to the quasistatic case.[30] Our approach closely follows recent related work,[17] and we introduce the right and left eigenmodes $\mathbf{E}_k(\mathbf{r},\omega)$ and $\tilde{\mathbf{E}}_k(\mathbf{r}',\omega)$ associated with the Σ matrix, respectively. Instead of the decomposition of eq 6, we then use

$$\mathbf{G}(\mathbf{r}, \mathbf{r}', \omega) \approx \sum_{k=1}^{n} C_k \mathbf{E}_k(\mathbf{r}, \omega) \otimes \tilde{\mathbf{E}}_k^*(\mathbf{r}', \omega)$$

and, accordingly, also modify eq 7. The biorthogonal expansion turns out to be advantageous in particular for nanoparticles with degenerate modes, as it automatically guarantees proper mode orthonormalization.

Compressed Sensing. The least-squares optimization is performed with the built-in Matlab functions, for the compressed sensing optimization we use the *YALL1* software freely available at http://yall1.blogs.rice.edu/. We set the mixing parameter $\mu = 5 \times 10^{-2}$, and the stopping tolerance has a value of 10^{-4}. We take 12 rotated EEL-maps for each structure with equidistant angles between 0 and 180°, each map consisting of 31 × 51 points. To speed up the optimization process, we take only 2000 random measurement points of the generated maps. Further, only measurement points with distance more than 15 nm away from the particle surface are used for optimization. For the volume visualization of the LDOS, we use the *MatVTK* software freely available at http://hdl.handle.net/10380/3076.

AUTHOR INFORMATION

Corresponding Author

*E-mail: ulrich.hohenester@uni-graz.at.

Notes

The authors declare no competing financial interest.

ACKNOWLEDGMENTS

We thank Georg Haberfehlner and Gerald Kothleitner for most helpful discussion. This work has been supported by the Austria Science Fund (FWF) Project Nos. P24511–N26, P27299–N27, SFB F49 NextLite, and NAWI Graz.

REFERENCES

(1) Garcia de Abajo, F. J. Optical excitations in electron microscopy. *Rev. Mod. Phys.* **2010**, *82*, 209.
(2) Kociak, M.; Stephan, O. Mapping plasmons at the nanometer scale in an electron microscope. *Chem. Soc. Rev.* **2014**, *43*, 3865.
(3) Bosman, M.; Keast, V. J.; Watanabe, M.; Maaroof, A. I.; Cortie, M. B. Mapping surface plasmons at the nanometre scale with an electron beam. *Nanotechnology* **2007**, *18*, 165505.
(4) Nelayah, J.; Kociak, M.; Stephan, O.; Garcia de Abajo, F. J.; Tence, M.; Henrard, L.; Taverna, D.; Pastoriza-Santos, I.; Liz-Martin, L. M.; Colliex, C. Mapping surface plasmons on a single metallic nanoparticle. *Nat. Phys.* **2007**, *3*, 348.
(5) Novotny, L.; Hecht, B. *Principles of Nano-Optics*; University Press: Cambridge, 2006.
(6) Garcia de Abajo, F. J.; Kociak, M. Probing the photonic local density of states with electron energy loss spectroscopy. *Phys. Rev. Lett.* **2008**, *100*, 106804.
(7) Hohenester, U.; Ditlbacher, H.; Krenn, J. Electron energy loss spectroscopy of plasmonic nanoparticles. *Phys. Rev. Lett.* **2009**, *103*, 106801.
(8) Hörl, A.; Trügler, A.; Hohenester, U. Tomography of particle plasmon fields from electron energy loss spectroscopy. *Phys. Rev. Lett.* **2013**, *111*, 086801.

DOI: 10.1021/acsphotonics.5b00256
ACS Photonics 2015, 2, 1429–1435

(9) Herman, G. T. *Image Reconstruction from Projections: The Fundamentals of Computerized Tomography*; Academic Press: New York, 1980.
(10) Nicoletti, O.; de la Pena, F.; Leary, R. K.; Holland, D. J.; Ducati, C.; Midgley, P. A. Three-dimensional imaging of localized surface plasmon resonances of metal nanoparticles. *Nature* **2013**, *502*, 80.
(11) von Cube, F.; Niegemann, J.; Irsen, S.; Bell, D. C.; Linden, S. Angular-resolved electron energy loss spectroscopy on a split-ring resonator. *Phys. Rev. B: Condens. Matter Mater. Phys.* **2014**, *89*, 115434.
(12) Atre, A. C.; Brenny, B. J. M.; Coenen, T.; Garcia-Etxarri, A.; Polman, A.; Dionne, J. A. Nanoscale optical tomography with cathodoluminescence spectroscopy. *Nat. Nanotechnol.* **2015**, *10*, 429.
(13) Jackson, J. D. *Classical Electrodynamics*; Wiley: New York, 1999.
(14) Sauvan, C.; Hugonin, J. P.; Maksymov, I. S.; Lalanne, P. Theory of the Spontaneous Optical Emission of Nanosize Photonic and Plasmon Resonators. *Phys. Rev. Lett.* **2013**, *110*, 237401.
(15) Ge, R. C.; Kristensen, P. T.; Young, J. F.; Hughes, S. Quasinormal mode approach to modelling light-emission and propagation in nanoplasmonics. *New J. Phys.* **2014**, *16*, 113048.
(16) Mäkitalo, J.; Kauranen, M.; Suuriniemi, S. Modes and resonances of plasmonic scatterers. *Phys. Rev. B: Condens. Matter Mater. Phys.* **2014**, *89*, 165429.
(17) Alpeggiani, F.; D'Agostino, S.; Sanvitto, D.; Gerace, D. Single-plasmon blockade from nanostructured metallic dimers. *arXiv:1508.01369*, **2015**.
(18) Candes, E. J.; Wakin, M. B. An introduction to compressed sensing. *Signal Processing Magazine IEEE* **2008**, *25*, 21.
(19) Yang, J.; Zhang, Y. Alternating direction algorithms for l1-problems in compressed sensing. *SIAM J. Sci. Comput.* **2011**, *33*, 250.
(20) Hohenester, U.; Trügler, A. MNPBEM - A Matlab Toolbox for the simulation of plasmonic nanoparticles. *Comput. Phys. Commun.* **2012**, *183*, 370.
(21) Hohenester, U. Simulating electron energy loss spectoscopy with the MNPBEM toolbox. *Comput. Phys. Commun.* **2014**, *185*, 1177.
(22) Midgley, P. A.; Dunin-Borkowski, R. E. Electron tomography and holography in materials science. *Nat. Mater.* **2009**, *8*, 271.
(23) Haberfehlner, G.; Orthacker, A.; Albu, M.; Li, J.; Kothleitner, G. Nanoscale voxel spectroscopy by simultaneous EELS and EDS tomography. *Nanoscale* **2014**, *6*, 14563.
(24) Duarte, M. F.; Davenport, M. A.; Takhar, D.; Laska, J. N.; Sun, T.; Kelly, K. F.; Baraniuk, R. G. Single-pixel imaging via compressive sampling. *IEEE Signal Process. Mag.* **2008**, *25*, 83.
(25) Schmidt, F.; Ditlbacher, H.; Hofer, F.; Krenn, J. R.; Hohenester, U. Morphing a nanodisk into a nanotriangle. *Nano Lett.* **2014**, *14*, 4810.
(26) Langbein, D. Normal modes at small cubes and rectangular particles. *J. Phys. A: Math. Gen.* **1976**, *9*, 627.
(27) Türeci, H. E.; Stone, A. D.; Collier, B. Self-consistent multimode lasing theory for complex or random lasing media. *Phys. Rev. A: At., Mol., Opt. Phys.* **2006**, *74*, 043822.
(28) Johnson, P. B.; Christy, R. W. Optical constants of the noble metals. *Phys. Rev. B* **1972**, *6*, 4370.
(29) Garcia de Abajo, F. J.; Howie, A. Retarded field calculation of electron energy loss in inhomogeneous dielectrics. *Phys. Rev. B: Condens. Matter Mater. Phys.* **2002**, *65*, 115418.
(30) Boudarham, G.; Kociak, M. Modal decompositions of the local electromagnetic density of states and spatially resolved electron energy loss probability in terms of geometric modes. *Phys. Rev. B: Condens. Matter Mater. Phys.* **2012**, *85*, 245447.

DOI: 10.1021/acsphotonics.5b00256
ACS Photonics 2015, 2, 1429−1435

7 Paper 4: Correlated 3D Nanoscale Mapping and Simulation of Coupled Plasmonic Nanoparticles

Published in: Nano Letters (2015)

NANO LETTERS

Letter

pubs.acs.org/NanoLett

Correlated 3D Nanoscale Mapping and Simulation of Coupled Plasmonic Nanoparticles

Georg Haberfehlner,[*,†,‡] Andreas Trügler,[§] Franz P. Schmidt,[‡] Anton Hörl,[§] Ferdinand Hofer,[†,‡] Ulrich Hohenester,[§] and Gerald Kothleitner[†,‡]

[†]Graz Centre for Electron Microscopy, Steyrergasse 17, 8010 Graz, Austria

[‡]Institute for Electron Microscopy and Nanoanalysis, Graz University of Technology, Steyrergasse 17, 8010 Graz, Austria

[§]Institute of Physics, University of Graz, Universitätsplatz 5, 8010 Graz, Austria

Supporting Information

ABSTRACT: Electron tomography in combination with electron energy-loss spectroscopy (EELS) experiments and simulations was used to unravel the interplay between structure and plasmonic properties of a silver nanocuboid dimer. The precise 3D geometry of the particles fabricated by means of electron beam lithography was reconstructed through electron tomography, and the full three-dimensional information was used as an input for simulations of energy-loss spectra and plasmon resonance maps. Excellent agreement between experiment and theory was found throughout, bringing the comparison between EELS imaging and simulations to a quantitative and correlative level. In addition, interface mode patterns, normally masked by the projection nature of a transmission microscopy investigation, could be unambiguously identified through tomographic reconstruction. This work overcomes the need for geometrical assumptions or symmetry restrictions of the sample in simulations and paves the way for detailed investigations of realistic and complex plasmonic nanostructures.

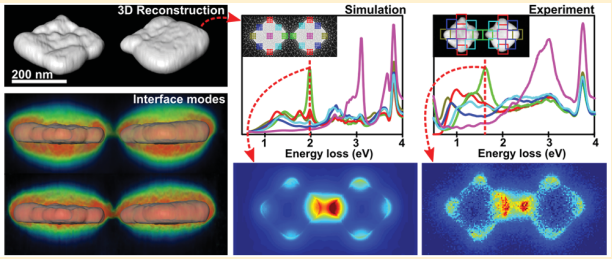

KEYWORDS: *Plasmonics, nanoparticles, electron tomography, electron energy loss spectroscopy, electron beam lithography*

Plasmonics confines light to subdiffraction volumes through excitation of collective electron charge oscillations at the boundaries of metallic nanoparticles, so-called surface plasmons,[1,2] and holds promise for various applications in photonics, optoelectronics, and (bio)sensing.[2,3] By tailoring shape and alignment of metallic nanoparticles, it becomes possible to control properties of localized surface plasmon resoncances (LSPRs), such as spectral peak positions or near-field couplings and enhancements.[1,2,4−6] In particular the top-down approach of electron beam lithography plays an important role in the quest of versatile nanoparticle manufacturing,[7−11] but the technique usually suffers from imperfections, surface roughness, and limited spatial resolution, which leads to nanoparticle shapes that deviate from the design objectives. Similar limitations apply to chemical synthesis, which generally leads to metallic nanoparticle ensembles with size dispersion and nonidentical geometries. Therefore, to exploit the full potential of plasmonics, full 3D characterization and simulation tools taking into account the imperfections of real structures become mandatory.

Monochromated EELS together with scanning transmission electron microscopy (STEM) provides a powerful combination to investigate individual plasmonic nanoparticles with high spatial (subnanometer) and energy (sub 100 meV) resolution.[12−14] Experimental data sets from which both the spatial 2D and energetic information can be retrieved, termed spectrum images (SI), have been used intensively to investigate LSPRs in various nanostructures.[5−11,15−18] The major limitation of this approach is the two-dimensional character of the technique, preventing the plasmon modes and the corresponding electromagnetic fields to be resolved in full 3D, since the spatial field distribution in the direction of the electron beam cannot be recovered from a single SI.

Although spectroscopic electron tomography is nowadays successfully and routinely employed in material science applications,[19−26] tomographic EELS mapping of LSPRs is complicated by the nonlocal self-interaction character of the plasmonic energy loss, where the swift electron first excites a LSPR and then performs work against the induced plasmon field.[27,28] Tomographic plasmon field reconstruction is generally possible only under restrictive assumptions, such as the applicability of the quasistatic approximation or a plasmonic response governed by a single mode, and was demonstrated in a single proof-of-principle experiment for a silver nanocube.[28] Possible routes to overcome these restrictions are based on inverse-problem schemes[29] or combined STEM and cathodo-

Received: September 18, 2015
Revised: October 22, 2015
Published: October 23, 2015

DOI: 10.1021/acs.nanolett.5b03780
Nano Lett. 2015, 15, 7726−7730

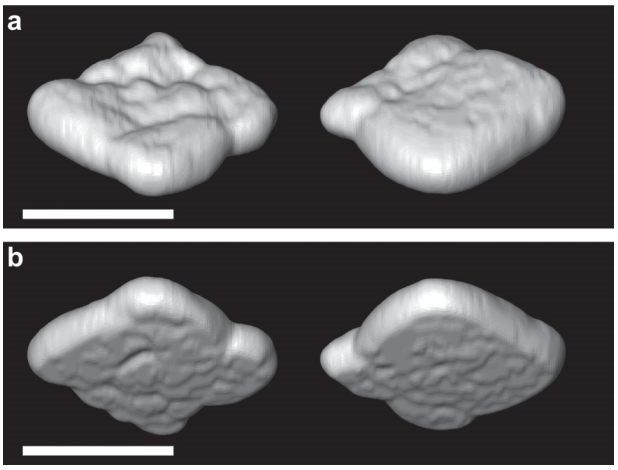

Figure 1. 3D reconstruction of the silver nanocuboids seen (a) from the top side and (b) from the bottom (substrate) side. Scale bars are 200 nm.

luminescence tomography, experimentally demonstrated for a metal−dielectric nanocrescent.[30] However, the quantitative predictability of these techniques still remains vague.

In this paper we demonstrate full 3D tomographic reconstruction of two coupled silver nanocuboids and measured EEL spectra and maps for a series of tilt angles. Instead of attempting a tomographic reconstruction of the plasmon fields (with exception of two interface modes to be discussed at the end), we used the precise 3D geometry of the particles as an input for EELS simulations[14,31−33] and computed EEL spectra and maps for direct comparison with experiment. The rationale behind this approach is that (i) EEL maps contain a vast amount of (partly dependent) information,[27,29] providing access to the entire plasmonic mode spectrum, and (ii) the predictability of EELS simulations has matured in recent years to the point where experiment and simulation can be compared on par. Our work renders plasmonic EELS capable for quantitative juxtaposition of experiment and simulation and significantly improves on previous simulation approaches using idealized geometries, such as perfectly symmetric cylinders, triangles, or cuboids, which neglected imperfections of real nanostructures despite their possible impact on the nanoparticles' plasmonic properties.

We investigated pairs of 30 nm thick silver nanocuboids designed by electron beam lithography on a 15 nm thin Si_3N_4 membrane. To reduce charging during the experiment, the nanocuboids were coated with a thin layer (∼1−2 nm) of carbon (see Supporting Information). Among the various cube sizes and gap distances fabricated on the membrane, in this study we selected two cubes with a nominal edge length of 200 nm and a gap of 70 nm between the corners. This particle dimer sustains a large number of distinct plasmon modes, as further discussed below, and the gap size is small enough to allow coupling between the two cuboids.

EEL spectrum images and mass−thickness high-angle annular dark-field (HAADF) STEM images were acquired for 30 tilt angles between −67° and +73° (see Supporting Information). The measured EEL spectra were treated with a Richardson-Lucy deconvolution[34,35] (see Supporting Information), and each resonance was integrated over 0.17 eV to generate 2D maps for comparison with simulation. The 3D morphology shown in Figure 1 was derived from the HAADF signal with a total-variation (TV) minimization reconstruction algorithm.[25,36] Our reconstruction scheme efficiently reduces missing wedge artifacts and recovers both top and bottom surfaces of the particles, which are impossible to obtain by conventional algorithms (see Supporting Information). While the bottom surface of the rhomboids, in contact with the substrate, are fairly flat, the upper side features significant roughness.

The reconstructed geometry of the silver cuboids served as an input for EELS simulations based on a boundary element method (BEM) approach and carried out with the MNPBEM toolbox.[32,33] In the simulations we consider both the actual geometry of the sample and the Si_3N_4 substrate, and we use a

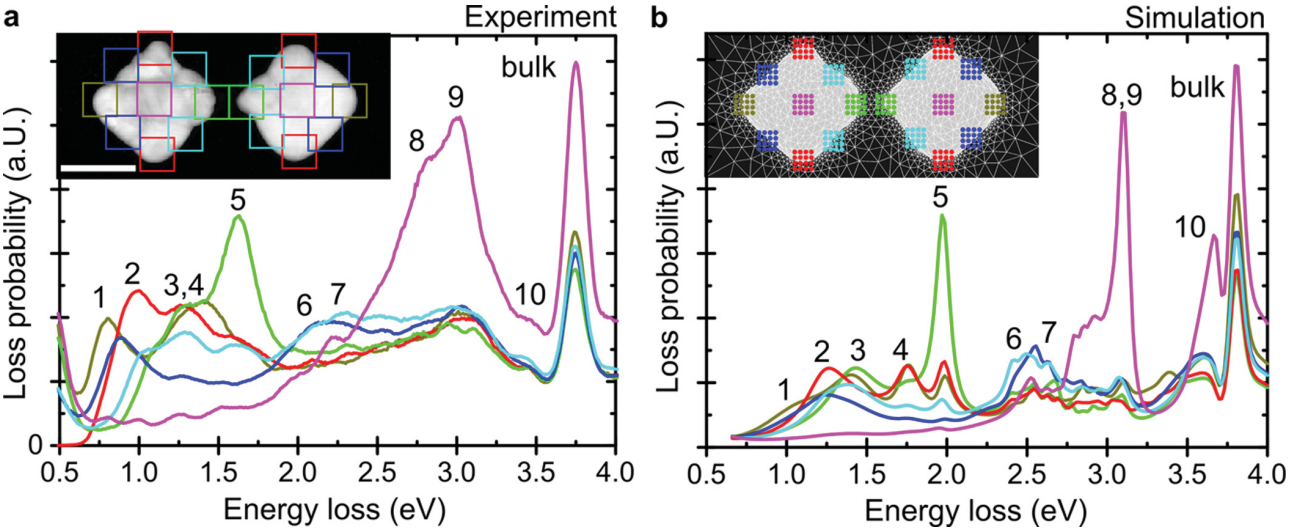

Figure 2. (a) Experimental and (b) simulated spectra extracted from different locations of the nanocuboids. For experimental data the spectra are averaged over regions marked by squares of the same color. For simulations spectra are averaged over the positions indicated by dots of the same color. In the spectra surface plasmon resonance peaks are labeled by numbers. Scale bars are 200 nm.

DOI: 10.1021/acs.nanolett.5b03780
Nano Lett. 2015, 15, 7726−7730

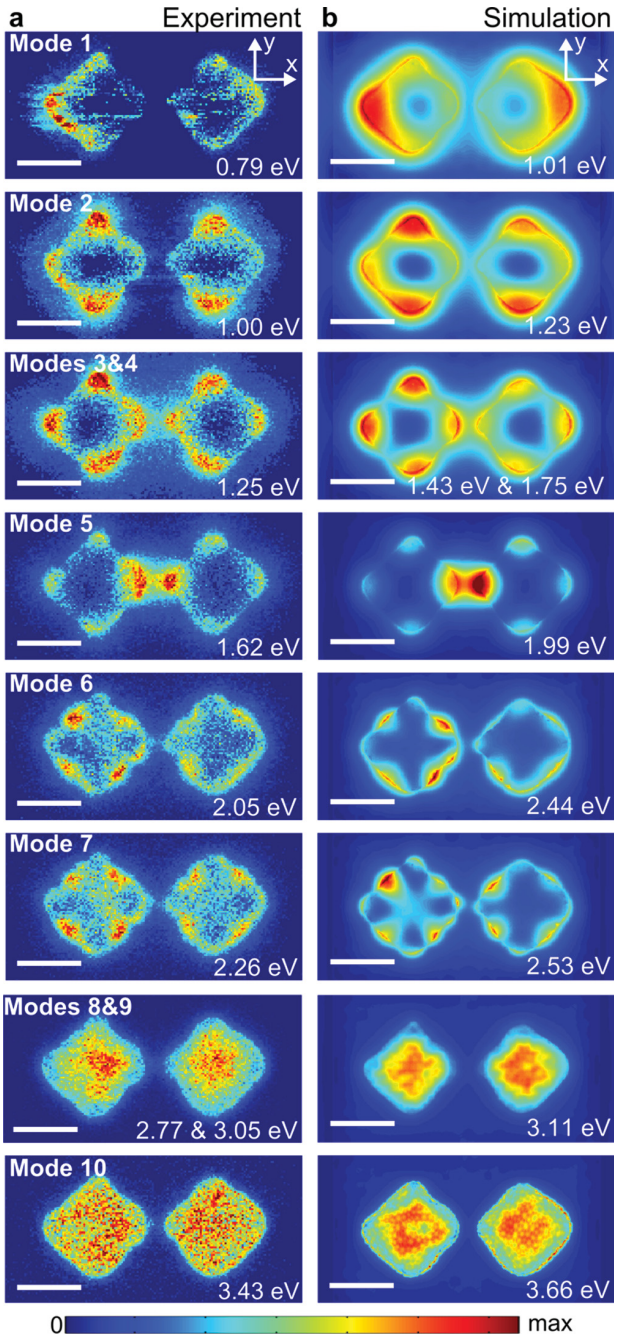

Figure 3. Surface plasmon resonance maps of the peaks indicated in Figure 2 extracted from experiments (a) and simulations (b). Modes 3 and 4 are overlapping in the experiment and summed for the simulations; modes 8 and 9 are overlapping in the simulation and summed for the experiment (see Supporting Information). The maximum in each map has been adapted for increased contrast, absolute peak intensities can be observed in the spectra in Figure 2. Scale bars are 200 nm.

tabulated dielectric function for silver extracted from optical data[37] (see Supporting Information).

Figure 2a and b shows EEL spectra from distinct spatial regions of the sample, extracted from experimental data and simulations, respectively. Experimental spectra were extracted from the spectrum image acquired at 0° tilt angle. Each spectrum shows the averaged value obtained from the colored positions, which were chosen by symmetry arguments; averaging allowed us to improve the signal-to-noise ratio of experimental spectra. This averaging approach can be validated by comparing spectra from the individual positions (see Supporting Information). The following positions on the cuboids are compared: outer corners (dark yellow), inner corners (green), as well as upper and lower corners (red). The outer edges (dark blue), the inner edges (cyan), and the centers of the cuboids (magenta) are also displayed. We find excellent agreement between the experimental and simulated EEL spectra, with exception of a few systematic deviations to be discussed below. Multiple resonant modes can be identified, labeled 1−10, starting from the lowest energy. While modes 1−5 have their maxima at the corners of the cuboids, modes 6 and 7 have them at the edges, and modes 8−10 in the center of the cuboids.

The experimental EEL features are generally slightly broader than the simulated ones, which we attribute to the limited energy resolution of our experiments. Regarding the energetic positions of the modes, a slight mismatch between experiment and simulations is noticeable, with the experimental resonance energies typically occurring at lower values than the simulated ones. The origin of these shifts is investigated by extended simulations (see Supporting Information), and is most likely due to nanoparticle aging and the modification of grain sizes, which leads to a modification of the metal permittivity and in turn to a red-shift of the plasmonic resonances, in agreement to related studies.[38,39] Supporting evidence for this interpretation is our observation of contrast changes for aged particles that went from a large crystal/polycrystalline state to near amorphization between deposition and analysis (see Supporting Information). In Figure 2, these shifts lead in the experimental spectra to an overlap of peaks 3 and 4 (separated peaks in simulations) and to a concurrence of peaks 8 and 9 (overlap in simulations).

At the plasmon peak energies, we extracted EEL maps from the experimental (Figure 3a, at 0° tilt angle) and simulation (Figure 3b) data. Modes 1−5 show maxima on the corners of the particles and are attributed to dipolar and quadrupolar modes based on their resonances energies and the spatial profile of the maps (see Supporting Information). Modes 1−3 show the spatial distribution of dipolar modes in the in-plane (x- and y-) directions. The dipole oriented along the x-direction splits up in energy into a bonding and antibonding mode, due to a coupling between the particles:[40] the bonding mode with dipolar moment in the x-direction (1) has the lowest energy, an uncoupled mode in the y-direction with dipolar moment (2) appears at a higher energy, and finally an antibonding dipolar mode in the x-direction has the highest energy (3). Because of an energetic overlap of modes 3 and 4 in the experiment, these modes are summed up for a more meaningful comparison in Figure 3 (see Supporting Information). Modes 4 and 5 are assigned to quadrupolar modes with the maxima on the corners of the particles. The coupling splits the quadrupoles into two distinct modes, a bonding (4) and an antibonding configuration (5).

In the range from 1.8 to 2.3 eV (2.2 to 2.7 eV) for the experiment (simulations), several other modes become apparent in Figure 2. Quadrupolar resonances, sensitive to the shape and the exact geometry of the particles, split up into several closely spaced signals as a result of structural imperfections. We exemplarily use modes 6 and 7 to highlight

DOI: 10.1021/acs.nanolett.5b03780
Nano Lett. 2015, 15, 7726−7730

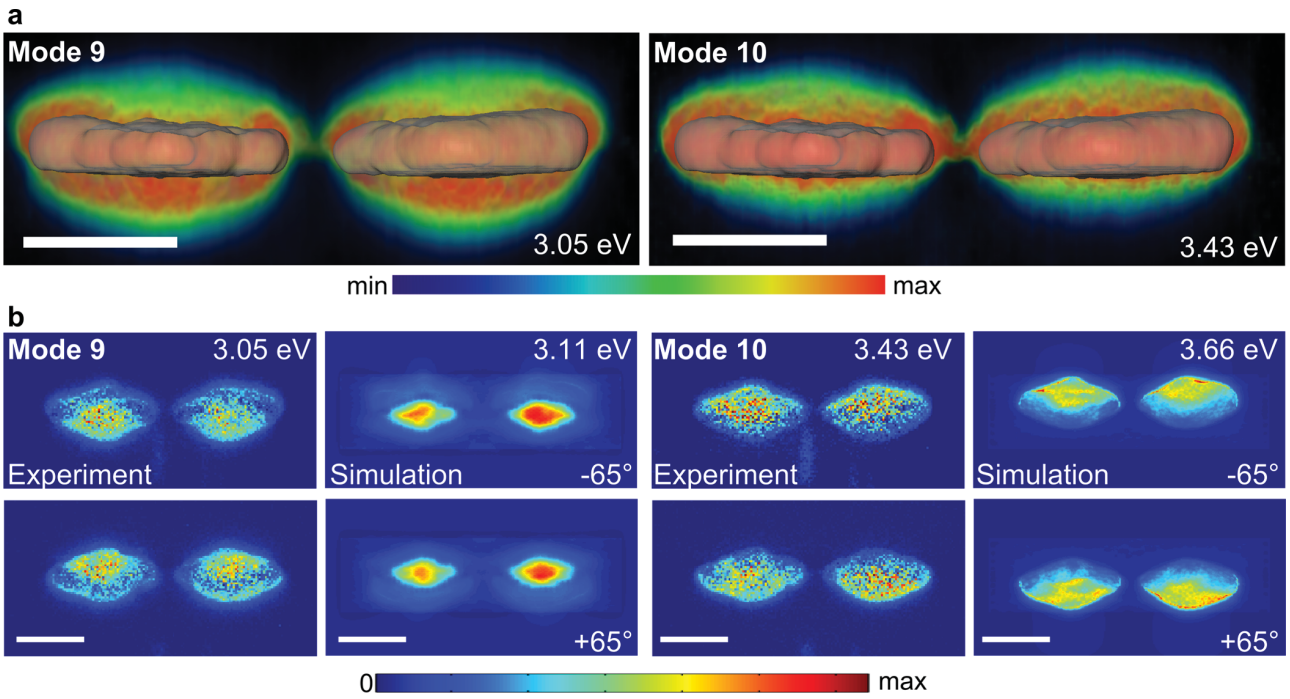

Figure 4. (a) 3D reconstructions of SiN/Ag interface mode (9) showing the maximum on the lower interface and Ag/C interface mode (10) showing the maximum on the upper interface. (b) Experimental and simulated maps of the same modes seen at tilt angles of −65° and +65°. The maximum in each map has been adapted for increased contrast. Scale bars are 200 nm.

the high-quality correlation between the measured and simulated maps: For ideal nanoparticles these EEL maps would have maxima of equal strength at the edge centers; for the realistic geometry in Figure 2 we observe significant differences for the excitation at different edges and even two maxima on a single edge for mode 6. It is gratifying to see the one-to-one mapping of practically all features in the EEL maps, including the absence and presence of signals in the center region for modes 6 and 7, respectively.

At even higher energies, three additional resonances can be observed that are attributed to the breathing mode (8) and the surface plasmon interface modes between Ag and Si_3N_4 (9) and between Ag and carbon/vacuum (10), respectively. As the breathing mode shifts to lower energies, due to aging of silver, modes 8 and 9 can be discriminated from each other (see Supporting Information). By contrast, these modes overlap in the simulations and are summed up for comparison in Figure 3. Mode 10 is significantly weaker in comparison to the simulations (see Figure 2), probably due to damping caused by the carbon layer deposited on top of silver, an effect not accounted for in the simulations.

The question whether modes 9 and 10 stem from different interfaces is addressed by both a tomographic reconstruction and analysis of tilted EEL maps. Quite generally, the size of the structure is too large to allow a quasistatic reconstruction for all modes.[27,28] However, for the vertical (z-) direction we expect the quasistatic reconstruction to provide a reasonable approximation (see Supporting Information). The map reconstructed from a tilt series of the respective EEL images is shown in Figure 4a. The lower energy mode (9) is indeed concentrated on the interface between silver and Si_3N_4, while the higher energy mode (10) is located on the silver/carbon interface. The vertical distribution becomes apparent also when looking at EEL maps of modes 9 and 10 under large angular tilt for both simulation and experimental data (Figure 4b) which are again in almost perfect agreement.

In conclusion, we have demonstrated how 3D reconstructed morphologies of metallic nanostructures can serve as an input for simulations of their plasmonic properties. Simulated EEL spectra and maps of coupled silver nanocuboids agree extremely well with experimental data, except for small deviations originating from incomplete information about the actual material composition and crystallinity. These differences could be eliminated if pure monocrystalline materials were used, or simulation tools would additionally consider the exact material properties. The 3D reconstruction of LSPR maps is feasible and allowed us to identify interface plasmons in the nanoparticles. Our work founds a basis for the detailed investigation of complex and realistic nanostructures, including geometry imperfections and surface roughness. It will be helpful for nanomaterial diagnostics but will also provide a tool for optimizing the material properties of complex nanostructures.

■ ASSOCIATED CONTENT

Supporting Information

The Supporting Information is available free of charge on the ACS Publications website at DOI: 10.1021/acs.nanolett.5b03780.

Methods including sample preparation, image acquisition, and data processing, plasmon resonance maps under several tilt angles, details about simulations, and considerations about sample aging (PDF)

■ AUTHOR INFORMATION

Corresponding Author

*E-mail: georg.haberfehlner@felmi-zfe.at.

DOI: 10.1021/acs.nanolett.5b03780
Nano Lett. 2015, 15, 7726−7730

Notes

The authors declare no competing financial interest.

■ ACKNOWLEDGMENTS

We thank Joachim Krenn and Harald Ditlbacher for access to and support with electron beam lithography and helpful discussion. This research has received funding from the European Union within the 7th Framework Program [FP7/2007-2013] under Grant Agreement no. 312483 (ESTEEM2). We acknowledge support by the Austrian Science Fund FWF under project P27299-N27, the SFB F49 NextLite, and NAWI Graz. Open-source software code has been used: The TV minimization solver TVAL3 (http://www.caam.rice.edu/~optimization/L1/TVAL3/) and the tomographic reconstruction toolbox ASTRA (http://sourceforge.net/projects/astra-toolbox/).

■ REFERENCES

(1) Maier, S. A. *Plasmonics: Fundamentals and Applications*; Springer: Boston, MA, 2007.
(2) Schuller, J. A.; Barnard, E. S.; Cai, W.; Jun, Y. C.; White, J. S.; Brongersma, M. L. *Nat. Mater.* **2010**, *9* (3), 193−204.
(3) Anker, J. N.; Hall, W. P.; Lyandres, O.; Shah, N. C.; Zhao, J.; Van Duyne, R. P. *Nat. Mater.* **2008**, *7* (6), 442−453.
(4) Batson, P. E. *Phys. Rev. Lett.* **1982**, *49* (13), 936−940.
(5) Chu, M.-W.; Myroshnychenko, V.; Chen, C. H.; Deng, J.-P.; Mou, C.-Y.; García de Abajo, F. J. *Nano Lett.* **2009**, *9* (1), 399−404.
(6) Rossouw, D.; Couillard, M.; Vickery, J.; Kumacheva, E.; Botton, G. A. *Nano Lett.* **2011**, *11* (4), 1499−1504.
(7) Boudarham, G.; Feth, N.; Myroshnychenko, V.; Linden, S.; García de Abajo, J.; Wegener, M.; Kociak, M. *Phys. Rev. Lett.* **2010**, *105* (25), 255501.
(8) Koh, A. L.; Fernández-Domínguez, A. I.; McComb, D. W.; Maier, S. A.; Yang, J. K. W. *Nano Lett.* **2011**, *11* (3), 1323−1330.
(9) Duan, H.; Fernández-Domínguez, A. I.; Bosman, M.; Maier, S. A.; Yang, J. K. W. *Nano Lett.* **2012**, *12* (3), 1683−1689.
(10) Schmidt, F.-P.; Ditlbacher, H.; Hohenester, U.; Hohenau, A.; Hofer, F.; Krenn, J. R. *Nano Lett.* **2012**, *12* (11), 5780−5783.
(11) Schmidt, F. P.; Ditlbacher, H.; Hofer, F.; Krenn, J. R.; Hohenester, U. *Nano Lett.* **2014**, *14* (8), 4810−4815.
(12) Bosman, M.; Keast, V. J.; Watanabe, M.; Maaroof, A. I.; Cortie, M. B. *Nanotechnology* **2007**, *18* (16), 165505.
(13) Nelayah, J.; Kociak, M.; Stéphan, O.; García de Abajo, F. J.; Tencé, M.; Henrard, L.; Taverna, D.; Pastoriza-Santos, I.; Liz-Marzán, L. M.; Colliex, C. *Nat. Phys.* **2007**, *3* (5), 348−353.
(14) García de Abajo, F. J. *Rev. Mod. Phys.* **2010**, *82* (1), 209−275.
(15) Koh, A. L.; Bao, K.; Khan, I.; Smith, W. E.; Kothleitner, G.; Nordlander, P.; Maier, S. A.; McComb, D. W. *ACS Nano* **2009**, *3* (10), 3015−3022.
(16) Kociak, M.; Stéphan, O. *Chem. Soc. Rev.* **2014**, *43* (11), 3865−3883.
(17) Schaffer, B.; Hohenester, U.; Trügler, A.; Hofer, F. *Phys. Rev. B: Condens. Matter Mater. Phys.* **2009**, *79* (4), 041401.
(18) N'Gom, M.; Li, S.; Schatz, G.; Erni, R.; Agarwal, A.; Kotov, N.; Norris, T. B. *Phys. Rev. B: Condens. Matter Mater. Phys.* **2009**, *80* (11), 113411.
(19) Möbus, G.; Doole, R. C.; Inkson, B. J. *Ultramicroscopy* **2003**, *96* (3−4), 433−451.
(20) Weyland, M.; Midgley, P. A. *Microsc. Microanal.* **2003**, *9* (6), 542−555.
(21) Gass, M. H.; Koziol, K. K. K.; Windle, A. H.; Midgley, P. A. *Nano Lett.* **2006**, *6* (3), 376−379.
(22) Midgley, P. A.; Dunin-Borkowski, R. E. *Nat. Mater.* **2009**, *8* (4), 271−280.
(23) Yedra, L.; Eljarrat, A.; Arenal, R.; Pellicer, E.; Cabo, M.; López-Ortega, A.; Estrader, M.; Sort, J.; Baró, M. D.; Estradé, S.; Peiró, F. *Ultramicroscopy* **2012**, *122*, 12−18.
(24) Haberfehlner, G.; Bayle-Guillemaud, P.; Audoit, G.; Lafond, D.; Morel, P. H.; Jousseaume, V.; Ernst, T.; Bleuet, P. *Appl. Phys. Lett.* **2012**, *101* (6), 063108.
(25) Haberfehlner, G.; Orthacker, A.; Albu, M.; Li, J.; Kothleitner, G. *Nanoscale* **2014**, *6* (23), 14563−14569.
(26) Midgley, P. A.; Thomas, J. M. *Angew. Chem., Int. Ed.* **2014**, *53* (33), 8614−8617.
(27) Hörl, A.; Trügler, A.; Hohenester, U. *Phys. Rev. Lett.* **2013**, *111* (7), 076801.
(28) Nicoletti, O.; de la Peña, F.; Leary, R. K.; Holland, D. J.; Ducati, C.; Midgley, P. A. *Nature* **2013**, *502* (7469), 80−84.
(29) Hörl, A.; Trügler, A.; Hohenester, U. *ACS Photonics* **2015**, *2* (10), 1429−1435.
(30) Atre, A. C.; Brenny, B. J. M.; Coenen, T.; García-Etxarri, A.; Polman, A.; Dionne, J. A. *Nat. Nanotechnol.* **2015**, *10* (5), 429−436.
(31) Myroshnychenko, V.; Rodríguez-Fernández, J.; Pastoriza-Santos, I.; Funston, A. M.; Novo, C.; Mulvaney, P.; Liz-Marzán, L. M.; García de Abajo, F. J. *Chem. Soc. Rev.* **2008**, *37* (9), 1792−1805.
(32) Hohenester, U.; Trügler, A. *Comput. Phys. Commun.* **2012**, *183* (2), 370−381.
(33) Hohenester, U. *Comput. Phys. Commun.* **2014**, *185* (3), 1177−1187.
(34) Gloter, A.; Douiri, A.; Tencé, M.; Colliex, C. *Ultramicroscopy* **2003**, *96* (3−4), 385−400.
(35) Lazar, S.; Botton, G. A.; Zandbergen, H. W. *Ultramicroscopy* **2006**, *106* (11−12), 1091−1103.
(36) Li, C.; Yin, W.; Jiang, H.; Zhang, Y. *Comput. Optim. Appl.* **2013**, *56* (3), 507−530.
(37) Johnson, P. B.; Christy, R. W. *Phys. Rev. B* **1972**, *6* (12), 4370−4379.
(38) Bosman, M.; Zhang, L.; Duan, H.; Tan, S. F.; Nijhuis, C. A.; Qiu, C.; Yang, J. K. W. *Sci. Rep.* **2014**, *4*, 5537.
(39) Trügler, A.; Tinguely, J.-C.; Jakopic, G.; Hohenester, U.; Krenn, J. R.; Hohenau, A. *Phys. Rev. B: Condens. Matter Mater. Phys.* **2014**, *89* (16), 165409.
(40) Hohenester, U.; Ditlbacher, H.; Krenn, J. R. *Phys. Rev. Lett.* **2009**, *103* (10), 106801.

DOI: 10.1021/acs.nanolett.5b03780
Nano Lett. 2015, 15, 7726−7730

Supporting Information

Correlated 3D nanoscale mapping and simulation of coupled plasmonic nanoparticles

Georg Haberfehlner[1,2], Andreas Trügler[3], Franz P. Schmidt[2], Anton Hörl[3], Ferdinand Hofer[1,2], Ulrich Hohenester[3], Gerald Kothleitner[1,2]

[1]Graz Centre for Electron Microscopy, Steyrergasse 17, 8010 Graz, Austria

[2]Institute for Electron Microscopy and Nanoanalysis, Graz University of Technology, Steyrergasse 17, 8010 Graz, Austria

[3]Institute of Physics, University of Graz, Universitätsplatz 5, 8010 Graz, Austria

S.1 Sample preparation

Electron beam lithography in a RAITH e-line system was applied to produce silver nanocuboids of 30 nm thickness on a 15 nm Si_3N_4 membrane (Ted Pella Inc. (US)) using a standard lift-off process with a poly(methylmetacrylate) resist[1]. The lateral dimensions of the nanoparticles were 200 nm x 200 nm with a gap distance of 70 nm in between the corners of the two nanocuboids. To reduce charging during the TEM measurements an additional thin carbon layer (~ 1-2 nm) was sputtered on the sample (EPA 100, Leybold-Heraeus GmbH (Germany)).

S.2 EELS acquisition & processing

Experiments were performed on a C_S-probe-corrected FEI Titan^3 60-300 microscope, with an X-FEG field-emission electron gun and a Wien-type monochromator operated in decelerated mode. The used acceleration voltage was 300 kV and excitation of the monochromator was set to 0.8. EELS spectra were acquired on a Gatan Imaging Filter (GIF) Quantum in hardware-synchronized mode with 26x vertical binning. Energy spread of the monochromated beam was measured to 170 meV as full-width at half-maximum of the zero-loss peak. The beam convergence semi-angle was 15 mrad and the collection semi-angle was 20.5 mrad.

Spectrum images (SIs) were acquired with a size of 312x198 pixels at a pixel size of 3 nm with an exposure time of 0.7 ms per pixel. All spectrum images were aligned in energy by shifting spectra pixel per pixel relative to their positions of the zero-loss peak and afterwards binned in two spatial dimensions by a factor of 2, i.e. four pixels were combined to a single pixel giving spectrum images with a size of 156x99 pixels. After energy-shift alignment and binning, the spectra were normalized by the maximum intensity of the zero-loss peak and deconvolved using Richardson-Lucy deconvolution (implemented in a home-made analysis program for spectrum images, realized in MATLAB) with 25 iterations (Fig. S1). As

point-spread function for deconvolution, the spectra in a corner of the spectrum image, away from the sample were averaged over 40x40 pixels. This averaged spectrum was fitted by a Gauss-Lorentz fit, which was subsequently used as point-spread function for all pixels in the spectrum image. To extract 2D maps of surface plasmon resonances the spectra were integrated over an energy region of 0.17 eV around the peak in the deconvolved spectrum images. The effects of the Richardson-Lucy deconvolution can be observed in Fig. S1 for both spectra and resonance maps. In the spectra the contribution of the zero-loss peak is well removed, additional resonance peaks (e.g. modes 8&10) become visible and other peaks are sharpened. However noise in the deconvolved dataset is higher, which is visible in particular in the comparison of the plasmon resonance maps before and after deconvolution.

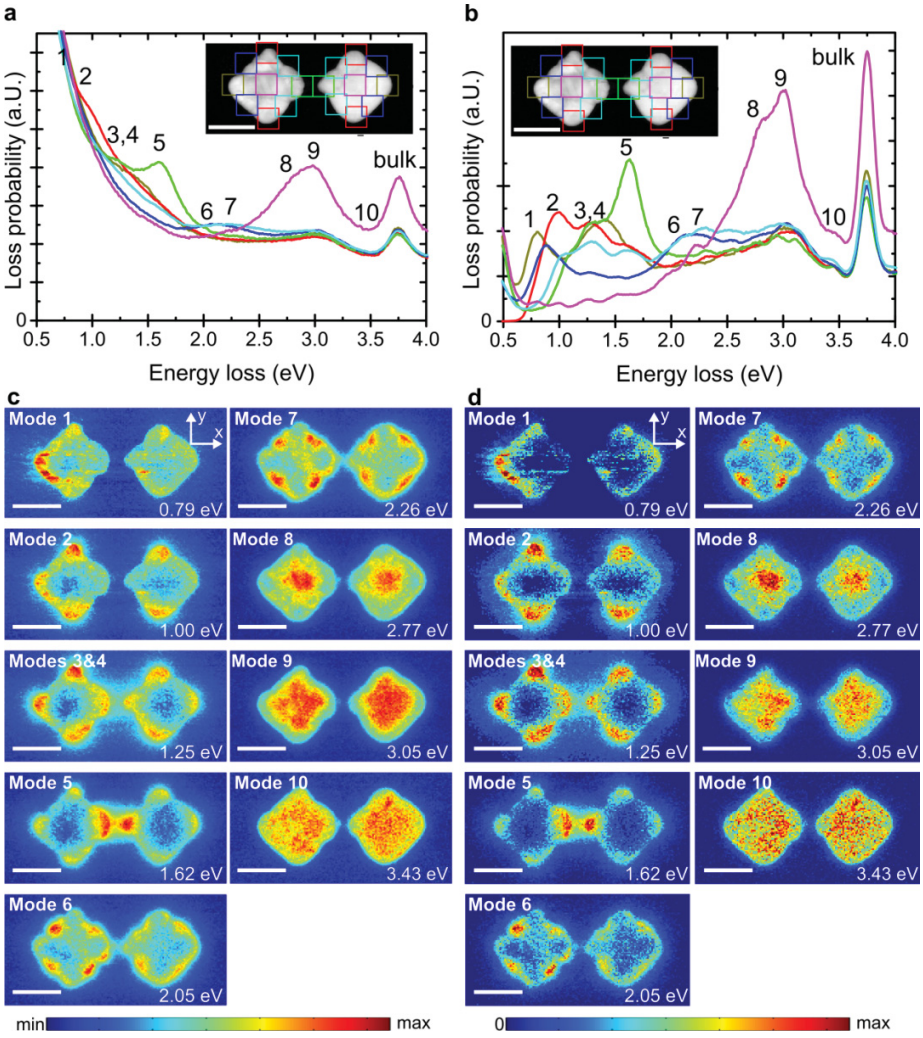

Figure S1. Deconvolution of spectra: (a) original spectra and (b) Richardson-Lucy deconvolved spectra. Spectra are extracted from different regions as indicated in the inset, where the colors of the spectra correspond to the extraction region. (c) 2D maps of surface plasmon resonances extracted from the original (zero-loss normalized) spectrum images and (d) from the Richardson-Lucy deconvolved spectrum images. All maps are integrated over an energy region of 0.17 eV around the peak position. The color-scale is adapted in each image to improve image contrast and remove the contribution of the zero-loss peak for the original dataset. Scale bars are 200 nm.

S.3 Spectra averaging

For comparison of spectra and identification of surface plasmon resonances, spectra were averaged based on the symmetry of the sample. In Fig. S2 we compare spectra from individual averaged regions for both experiment and simulations. Though the amplitude of different peaks varies between the different regions due to imperfections of the sample geometry their resonance energies corresponds well, in particular for the modes with maxima on the corners (1-5) and the interface modes (9-10). For the spectra taken from the edges of the particles, a number of closely spaced maxima is visible in both simulation and experiments, which are however too closely spaced to allow separation. For this reason, maps were extracted for the two strongest peaks in the averaged spectra (6-7) and compared between experiment and simulations. The extracted spectra also indicate that the position of resonance peaks do not depend on local grain structure, as the peak positions remain constant between different regions. The overall crystallographic structure however is known to affect the peak positions for the whole system, which is the suggested cause for peak shifts between experiment and simulations (see Section S.9)

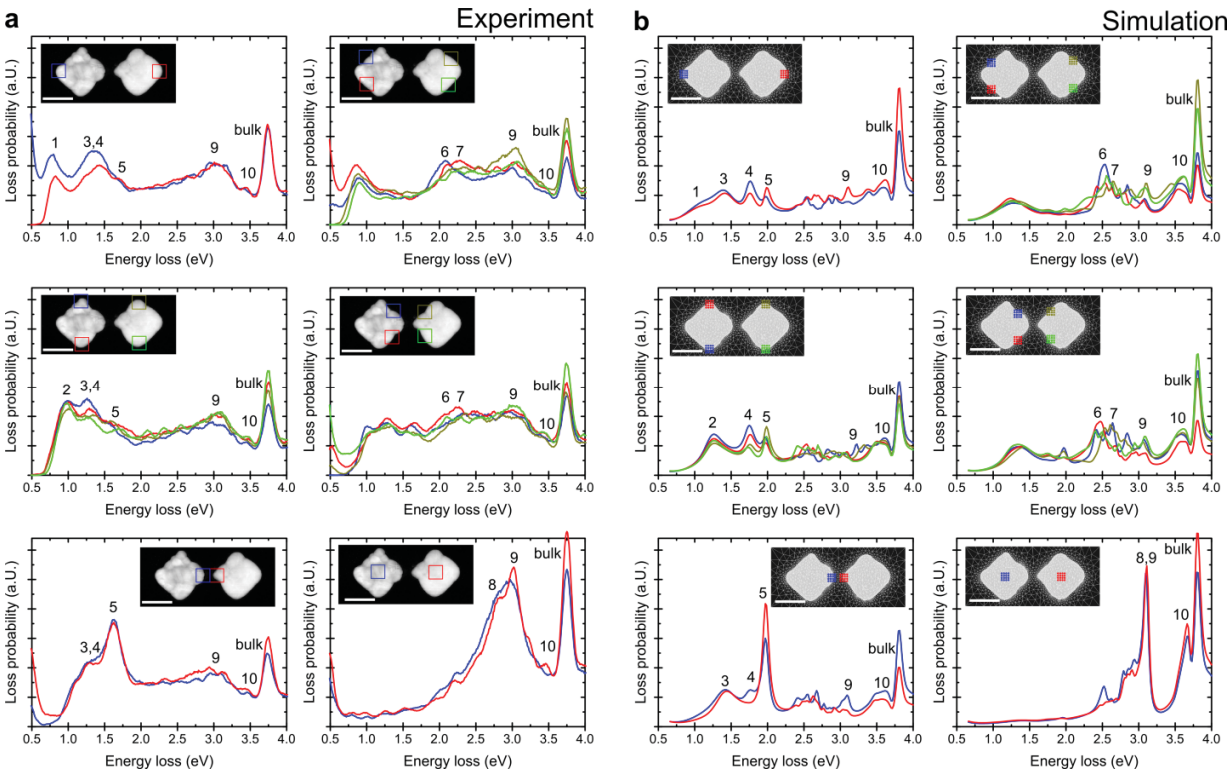

Figure S2. Comparison of spectra extracted from symmetric regions for experiment (a) and simulation (b). The spectra are extracted from the locations indicated in the inset. In the main text (Fig. 2) the spectra within each plot are averaged. Scale bars in the insets are 200 nm.

S.4 HAADF STEM and EELS SI tilt series acquisition

Tilt series were acquired between -73° and +67° with steps of 5° from -70° to +65° and two additional tilt angles at -73° and +67°. EELS SIs at each tilt angle were acquired and processed as described above. For HAADF STEM data the original pixel size (3 nm) was kept without binning. Fig. S3 shows HAADF STEM projections and extracted surface plasmon resonance maps for different tilt angles.

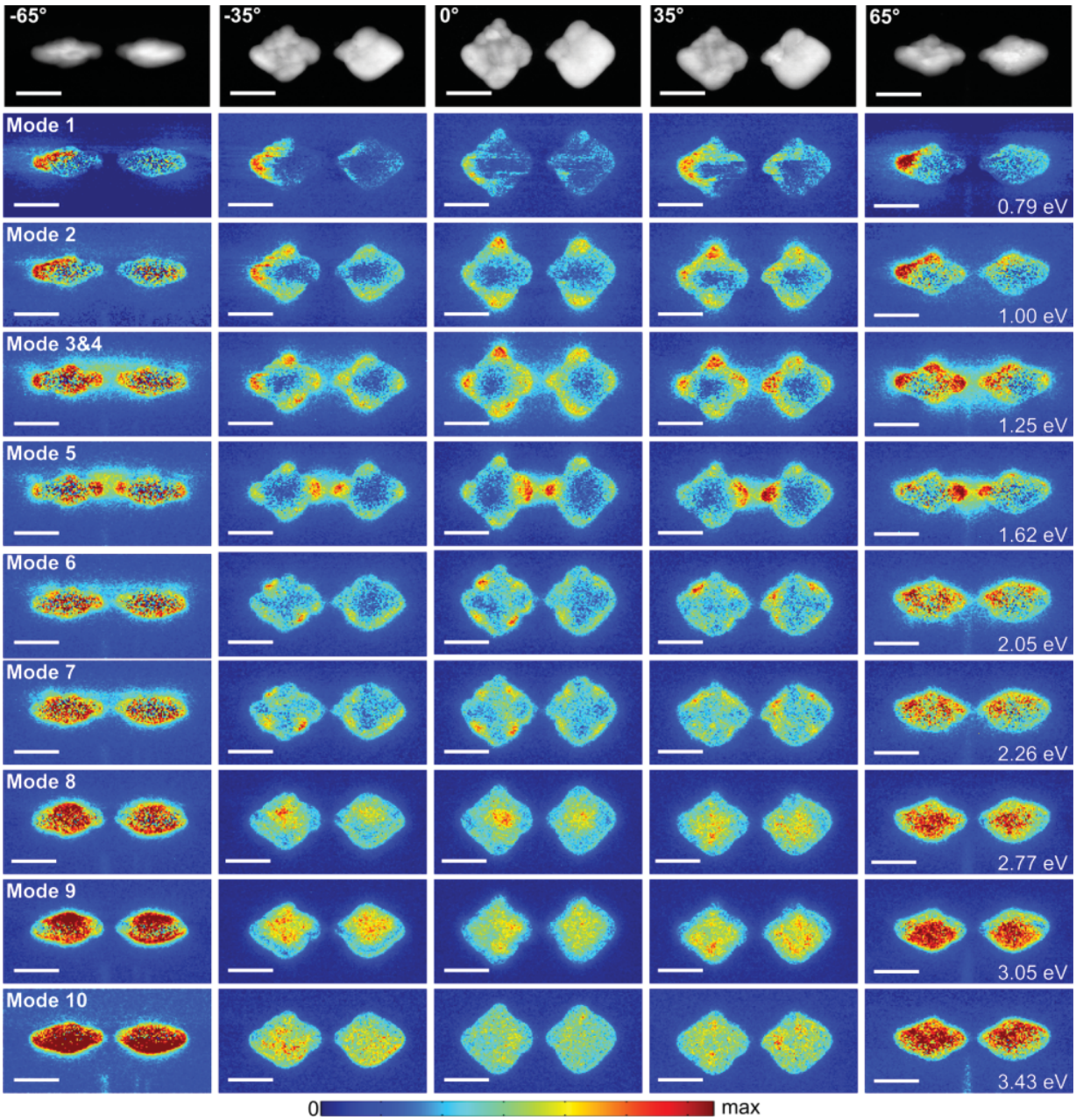

Figure S3. HAADF STEM images and 2D maps of plasmon resonances at different tilt angles. The maximum in each map has been adapted for increased contrast. Scale bars are 200 nm.

S.5 Mode assignments

Due to retardation effects caused by the relatively large sizes of the particles, the simulated charge distributions are rather difficult to interpret. In Fig. S4 we thus only report a sketch of the simulated profiles of dipolar and quadrupolar modes 1 to 5 together with computed EEL maps. Dipolar modes (1-5) show relatively broad maxima at two opposite corners of each particle. Due to coupling of the particles the dipole splits up into 3 modes, a low-energy bonding configuration (mode 1), a neutral configuration (mode 2) and a high-energy anti-bonding configuration (mode 3). The quadrupolar modes (4-5) show sharper maxima on all four corners and have higher energies than the dipolar modes. Upon coupling they split up into a bonding (mode 4) and an anti-bonding configuration (mode 5).

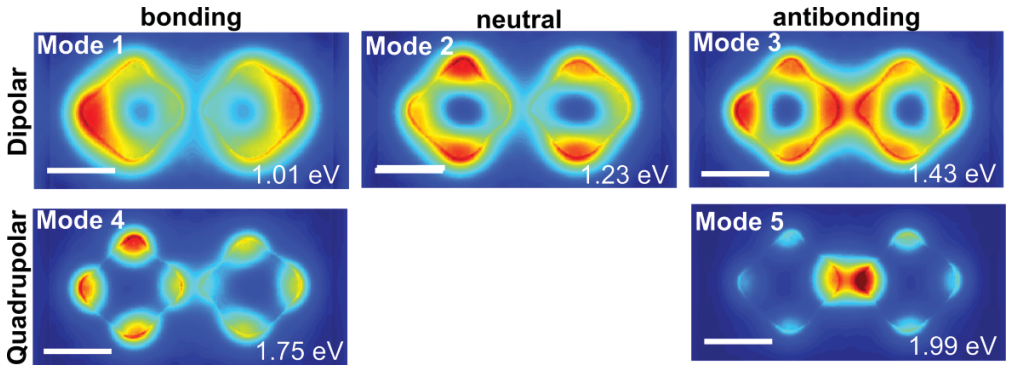

Figure S4. Assignments of dipolar and quadrupolar mode configurations. Scale bars are 200 nm.

S.6 Tilt series alignment

Alignment of the tomographic tilt series was done based on the HAADF STEM images acquired simultaneously with the EELS spectrum images. To remove the influence of the background signal on the alignment, first of all the absolute minimum of each projection was subtracted from every pixel in the projection. Then a mask was created using thresholding and morphological operations to select only pixels in which the cuboids are projected and their close vicinity. All pixels outside of this mask were set to 0. These masked projections were used for the alignment. The center of each projection in x- and y-direction was found by calculating the center of mass of the projection. The tilt-axis was found calculating rotational centers from sinograms, again based on the center of mass. The calculated alignment parameters were used to align both the HAADF STEM tilt series and the tilt series of EELS spectrum images.

S.7 Reconstruction of the HAADF STEM tilt series

The HAADF STEM tilt series is reconstructed using a total-variation (TV) minimization algorithm using the full 3D gradient calculation as described in previous work[2]. In TV minimization it is assumed that the volume gradient is sparse, i.e. is zero at most locations. This leads to sharp interfaces between different materials. A 3D adaptation of the TV minimization solver TVAL3[3] is used in combination with GPU-based

projection and re-projection operators from the ASTRA toolbox[4]. In the present case TV minimization worked well for reconstructing the shape of the nanoparticles, even though the flat interfaces between different materials lie in an unfavorable orientation with respect to the missing wedge. This is illustrated in Fig. S5, where the TV minimization reconstruction is compared to a reconstruction done with the simultaneous iterative reconstruction technique (SIRT)[5].

To get the morphology of the nanocuboids as input for simulations, the HAADF STEM reconstruction is segmented using an Otsu-threshold[6]. From the segmented reconstruction a triangulation of the silver surface is calculated, which can then be used as input for the boundary element method in the simulations.

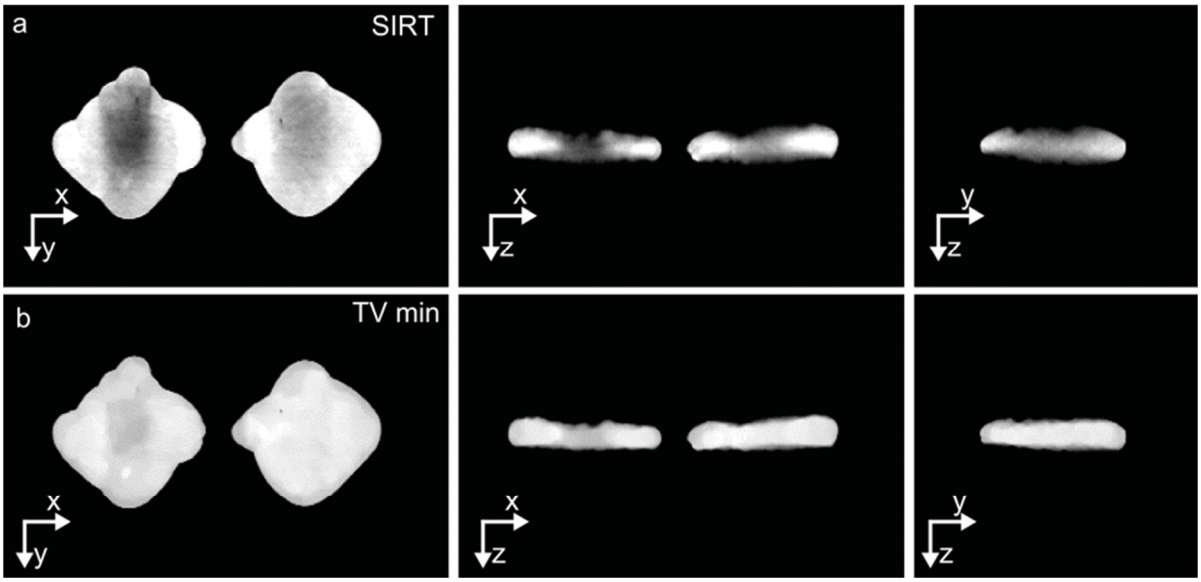

Figure S5. Orthogonal slices through reconstructions from HAADF STEM data using (a) a SIRT algorithm and (b) a total-variation minimization algorithm.

S.8 Superposition of modes in experiment and simulation

In the experiments shifts of resonance peaks led to an overlap of peaks 3 and 4 in the experiment (separated in simulations) and to a separation of peaks 8 and 9 (overlapping in simulations). For the comparison of plasmon resonance maps between experiments and simulation (Fig. 3), the maps of peaks 3 and 4 have been summed up for simulated data (Fig. S6a) and the maps of peaks 8 and 9 for experimental data (Fig. S6b)

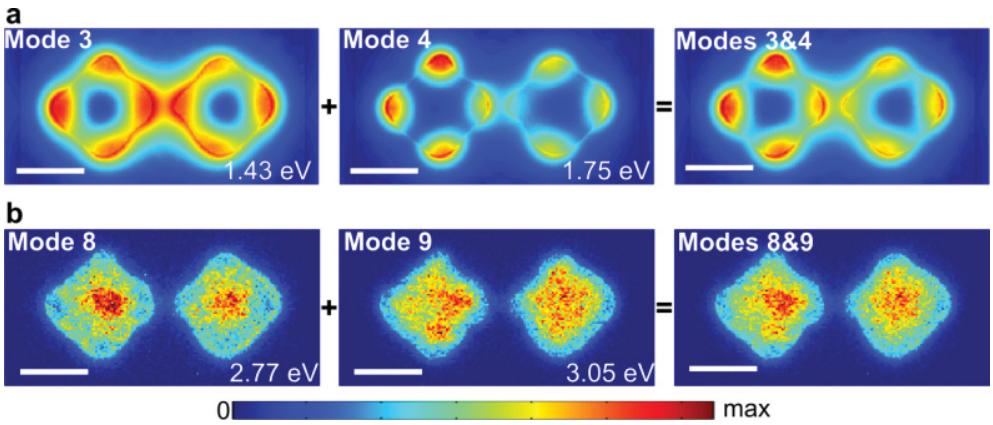

Figure S6. (a) Summation of modes 3 and 4 for simulations for comparison to superposition of modes in experiment. (b) Summation of modes 8 and 9 for experiment for comparison to superposition of the modes in simulation. The maximum in each map has been adapted for increased contrast. Scale bars are 200 nm.

S.9 Experimental observation of sample ageing

During the experiments it was observed that ageing of the samples leads to a red-shift of resonance peaks. First experiments were done on samples immediately after sample preparation without deposition of a carbon layer. A HAADF STEM image of nanocuboids taken in this investigation is shown in Fig. S7a. Here the crystalline structure of the silver is clearly visible. Charging issues in this investigation led to significant sample drift in particular at large tilt angles, which prevented successful acquisition of tilt series. Therefore a second investigation on the same sample was done with an additional thin carbon layer deposited on the sample. This significantly reduced charging of the sample and thereby made tomography possible. Between the first and second investigation the sample was stored in an evacuated chamber to keep the aging process due to chemical reaction of the silver with surrounding air components (mainly oxygen and sulfur) as small as possible. However we observed some aging process as shown in Fig. S7. A HAADF STEM image of the fresh sample (a) is compared to the sample of the second investigated (b). The contrast in Fig. S7b is much more diffuse, which may indicate a loss of crystallinity.

For further detailed investigations of sample ageing bright-field imaging or diffraction studies together with analytical electron microscopy will be useful to clearly reveal structural and chemical changes in the sample. The effects of sample ageing could be reduced by minimizing the time between sample fabrication and investigation. Potentially also a coating layer could reduce ageing, but experimentally a resonance shift is also observed with a thin carbon layer on top. Another possibility could be to use gold instead of silver, which is more stable to environmental influences.

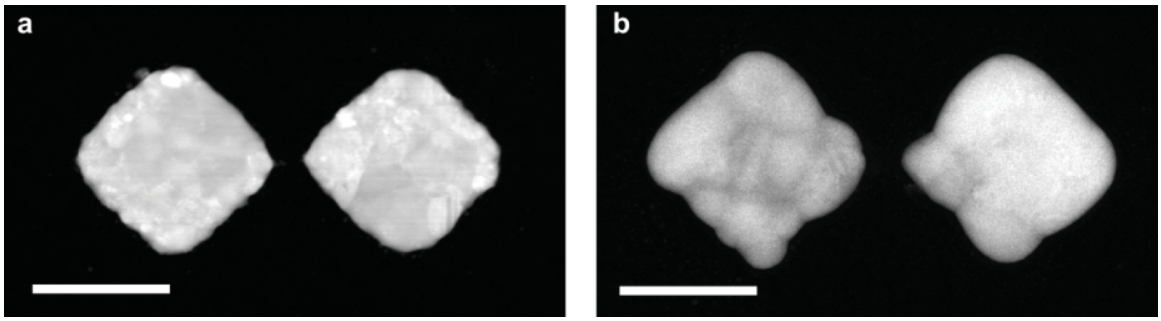

Figure S7. HAADF STEM images of (a) a fresh sample (b) the investigated aged sample (not the same particle pair as in (a)). Scale bars are 200 nm.

S.10 Simulations

In our simulation approach we compute the EEL spectra using the MNPBEM toolbox[7,8] and use a silver dielectric function extracted from optical experiments[9]. The particle boundaries consist of typically 7000 elements, and the 15 nm thick Si_3N_4 membrane (permittivity of 4) is modeled as an additional particle boundary. The simulated EEL maps were computed at the loss energies indicated in the figures (no spectral convolution).

S.11 Investigation of the influence of simulation parameters

To analyze how the plasmonic resonances could be affected by changes of materials chemistry, we performed additional simulations. Fig. S8 shows the simulated nanocube dimers, including the Si_3N_4 membrane, together with four selected beam positions.

To model sample aging, we modified the dielectric properties of the metallic nanoparticle by adding to the silver permittivity ε an additional silver-sulfide contribution. This led to a broadening of the resonance peaks, but to no significant spectral shifts (Fig. S9). Carbon contamination was analyzed in a similar fashion by adding carbon contributions to ε, finding again peak broadenings but no significant spectral shifts (Fig. S10).

In Fig. S11 we finally investigate the influence of the size of the Si_3N_4-substrate plate, demonstrating the convergence of the simulation results shown in the main manuscript. Also possible thickness variations of the membrane were investigated in additional simulations (results not shown), finding red-shifts with increasing thickness. However, significant shifts would require thicknesses 2-3 times larger than the nominal thickness (15 nm). Based on these observations we concluded that the most likely reason for the differences between simulations and experiments is the crystallinity of the silver, which modifies the silver permittivity according to the discussion given in the main manuscript.

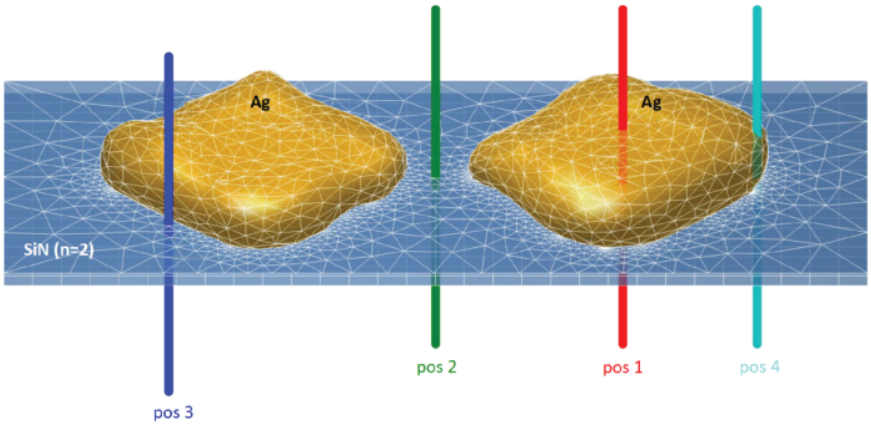

Figure S8. Model of simulated nanocube dimers and beam positions for the spectra extracted in Figs. S9-S11.

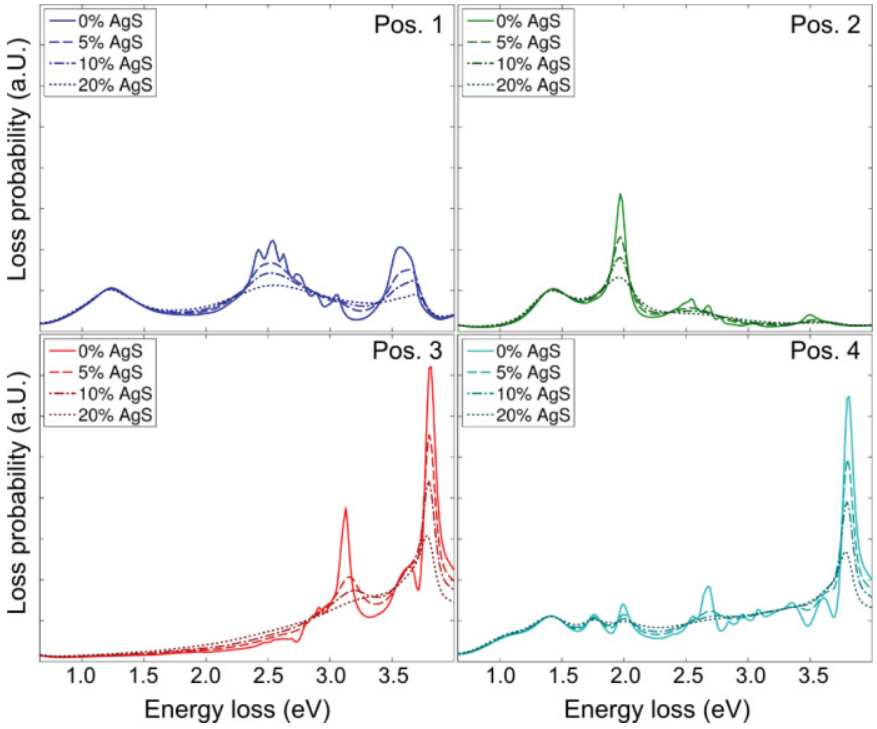

Figure S9. Simulated spectra for different concentrations of silver-sulfide (0-20%) extracted for the 4 positions indicated in Fig. S8.

8 Paper 5: Gap plasmonics of silver nanocube dimers

Published in: Physical Review B, (2016)

PHYSICAL REVIEW B **93**, 081405(R) (2016)

Gap plasmonics of silver nanocube dimers

Dario Knebl,[1] Anton Hörl,[1] Andreas Trügler,[1] Johannes Kern,[2] Joachim R. Krenn,[1] Peter Puschnig,[1] and Ulrich Hohenester[1,*]
[1]*Institute of Physics, University of Graz, Universitätsplatz 5, 8010 Graz, Austria*
[2]*Institute of Physics and Center for Nanotechnology, University of Münster, 48149 Münster, Germany*
(Received 19 August 2015; published 9 February 2016)

We theoretically investigate gap plasmons for two silver nanocubes coupled through a molecular tunnel junction. In the absence of tunneling, the redshift of the bonding mode saturates with decreasing gap distance. Tunneling at small gap distances leads to a damping and slight blueshift of the bonding mode, but no low-energy charge transfer plasmon mode appears in the spectra. This finding is in stark contrast to recent work of Tan *et al.* [Science **343**, 1496 (2014)].

DOI: 10.1103/PhysRevB.93.081405

Gap plasmonics [1] deals with surface plasmons (SPs) [2] in narrow gap regions of coupled metallic nanoparticles. For sufficiently narrow gaps, electrons can tunnel directly from one nanoparticle to the other one, leading to the emergence of new charge transfer plasmons (CTPs) [1,3–6]. Molecular tunnel junctions enable tunneling over larger gap distances in the nanometer regime [7,8], and thus establish a novel platform for hybrid structures reconciling molecular electronics with plasmonics.

Recent years have seen significant research efforts to understand the properties of gap plasmons and have highlighted the importance of the tunneling strength as a trigger for the CTP appearance [9] and of the gap morphology which strongly influences the CTP spectral position [10]: for rounded gap terminations the bonding mode redshifts with decreasing gap separation, until tunneling sets in, as evidenced by the appearance of a low-frequency CTP together with a broadening and blueshift of the bonding mode [1,3,6]. In contrast, for flat terminations the redshift of the bonding mode saturates with decreasing gap distance, while at the same time the transversal cavity plasmon (TCP) modes shift to the red; here, the onset of tunneling has no significant impact on the bonding mode and no low-frequency CTP appears in the spectra.

In this paper, we theoretically investigate the plasmonic properties of two coupled silver nanocubes, similarly to the electron energy loss spectroscopy (EELS) experiments of Tan *et al.* [7] for two nanocubes coupled through a molecular tunnel junction. We compute EEL and extinction spectra using the MNPBEM toolbox [11–13], supplemented with the quantum corrected model (QCM) [14] to account for quantum tunneling. We find that the redshift of the bonding mode saturates with decreasing distance and an additional tunnel conductivity in the gap region leaves the spectral position unaffected. The TCP modes shift with decreasing gap distance to the red, and the tunnel conductivity damps these modes. All these findings are in perfect agreement with the observations of Esteban *et al.* [6] for flat gap terminations and would qualify our work as a systematic research paper, if it was not for this single point: Despite serious efforts we were unable to confirm the emergence of the low-energy CTP observed by Tan *et al.* [7] and could not reproduce their simulation results. We will argue why we believe that our results are valid within the electrodynamic and QCM model under consideration, and why a re-interpretation of the experiments might be needed.

In our simulations we model the cubes with rounded edges and corners as superellipsoides, whose boundaries are parameterized through $u \in [0,\pi)$ and $v \in [-\pi,\pi)$ according to

$$x(u,v) = a\, s(u,r)\, c(v,r) \tag{1a}$$

$$y(u,v) = a\, s(u,r)\, s(v,r) \tag{1b}$$

$$z(u,v) = a\, c(u,r)\,, \tag{1c}$$

where a determines the cube size (we use side lengths of 35 nm throughout), r is a rounding parameter, and we have introduced the functions $s(\xi,r) = \mathrm{sign}(\sin\xi)|\sin\xi|^r$ and $c(\xi,r) = \mathrm{sign}(\cos\xi)|\cos\xi|^r$. For the cubes we set $r = 0.25$, but will later use larger r values in order to morph the cubes to spheres [15]. For the electrodynamic simulations we employ the MNPBEM toolbox [11–13] and use for the dielectric function of silver tabulated values extracted from optical experiments [16].

Figure 1 shows density plots of the (a)–(c) EEL and (d) optical extinction spectra for two coupled silver nanocubes as a function of gap distance, using classical electrodynamic simulations where no tunneling is considered. For the EEL spectra the impact parameters of the electron beams are indicated in the insets, and for the optical spectra the light polarization is along the direction of the cube connection. For large gap separations the EEL and optical spectra agree with those of a single cube, whose modes have been studied in detail elsewhere [17,18]. With decreasing gap distance the bonding mode (denoted in Ref. [10] also as longitudinal antenna plasmon, LAP) shifts to the red [19], as seen most clearly in the extinction spectra of Fig. 1(d). At distances around a few nanometers new modes appear in the spectra which continuously redshift when further decreasing the gap distance. In accordance to Ref. [10], and as shown by the surface charge maps in Fig. 2(c), we assign these modes to TCPs. Whenever these modes cross the bonding mode we observe a clear anticrossing, a finding which we attribute to mode coupling. The overall redshift of the bonding mode saturates for the smallest gap distances, say at a value of 2.8 eV. From the comparison of the different panels of Fig. 1 we see that these mode characteristics can be observed in both EEL

*ulrich.hohenester@uni-graz.at

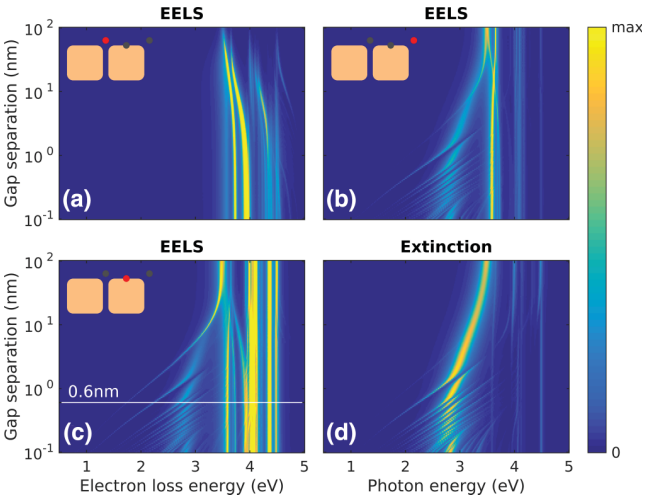

FIG. 1. Classical electrodynamic simulations of (a)–(c) EEL and (d) optical extinction spectra for two coupled silver nanocubes with side lengths of 35 nm. The impact parameters for the electron beams are indicated in the insets of panels (a)–(c), and the light polarization direction is along the cube connection direction in panel (d). Notice the logarithmic scale used for the gap distances. All density plots are normalized to the respective maximal values. The line in panel (c) reports the gap distance used in Fig. 2.

and optical spectra, with the only exception of panel (a), where the electron beam is located in the center plane of the gap and the excitation of the bonding mode is forbidden because of symmetry [20].

Figure 2 shows density plots of EEL spectra (electron beam positions indicated in insets) for two coupled (a) spheres and

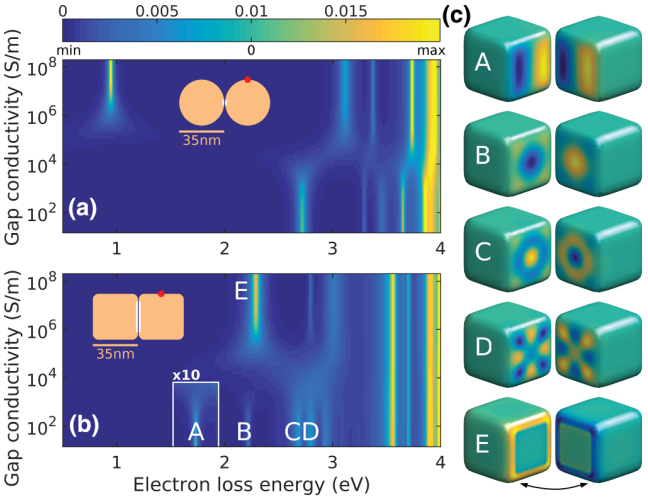

FIG. 2. Density plots for EEL spectra of coupled silver (a) spheres and (b) cubes as a function of loss energy and gap conductivity, and for a gap distance of 0.6 nm. The impact parameters of the electron beams and the active region where tunneling is considered are shown in the insets. The color bar indicates the loss probabilities in eV^{-1}. Probabilities in region A have been multiplied by a factor of ten for clarity. (c) Surface charge distribution (imaginary part) of modes A–E at the resonance energies. Cubes are rotated apart to offer a better view to the gap region.

(b) cubes separated by a distance of 0.6 nm. We allow for tunneling within a distance region of 0.6–0.8 nm (see inset, distance region chosen in order to mimic molecular tunnel junction) using the QCM of Ref. [14]. In each simulation the gap conductivity within the region where tunneling is allowed is set to a constant value. For the spheres shown in panel (a) and for the smallest gap conductivities σ_{gap}, the lowest SP mode at an energy of 2.7 eV is attributed to the bonding mode. When increasing σ_{gap}, above a critical threshold of say 10^5 S/m there is a transition where (i) a CTP appears at an energy of about 1 eV and (ii) the bonding mode blueshifts and broadens. These features are in agreement with the literature [1,6,14]. Also the weak dependence of the SP energy on σ_{gap} above or below the critical threshold has been previously reported [9].

For the coupled nanocubes shown in Fig. 2(b) there is again a transition in the EEL spectra when increasing σ_{gap}, and again above or below the critical threshold the SP energies depend very weakly on the gap conductivity. As regarding the SP modes, we observe above the critical σ_{gap} value the appearance of a new mode E, which, in contrast to the spheres, is *not* accompanied by an additional low-energy CTP mode. This finding is in agreement with that of Esteban *et al.* [10] for flat gap terminations, and highlights the importance of the gap morphology on the SP modes.

In Fig. 2(c) we report the surface charge distributions of a few selected SP modes. For small σ_{gap} values, A–D correspond to hybridizations between TCP and bonding modes. In principle, because of symmetry all modes are double or multiple degenerate [21] and the mode symmetry shown in the figure is governed by the electron beam position. Above the critical σ_{gap} threshold, (i) the cavity modes become damped (see for instance disappearance of mode A in Fig. 2(b), whose intensity has been magnified by a factor of 10 for clarity), and (ii) a new mode E appears which dominates in the EEL spectra. As can be inferred from Fig. 2(c), mode E is a CTP where electron tunneling leads to an opposite charging of the cubes.

To further explore the impact of the gap morphology on the SP energies, in Fig. 3 we investigate the scenario where two coupled spheres are deformed to two coupled cubes. Such morphing has been proven successful for a deeper insight to SP mode characteristics [15]. In our simulations we vary the rounding parameter r in Eq. (1) from 0.25 for the cubes to 1 for the spheres. The gap distance is set to 0.6 nm for all geometries, and we again consider tunneling within a distance region of 0.6–0.8 nm using a tunnel conductivity of 2.49×10^5 S/m representative for BDT. For the spheres with $r = 1$ we observe in the extinction spectra of Fig. 3(a) the CTP and bonding modes at energies of 1 eV and 3 eV, respectively. Upon morphing to two cubes, (i) the CTP mode shifts to higher energies and (ii) the bonding mode acquires a higher oscillator strength. For comparison, in Fig. 3(b) we show the extinction spectrum for a cuboid with a side length of twice the cube length, consisting of one major peak approximately at the energy position of the CTP mode for the coupled nanocubes. Similarly, it has been shown that the CTP peak for the coupled spheres has approximately the same energy as the dipole mode for two slightly coalescing spheres ("negative gap distance") [1,6].

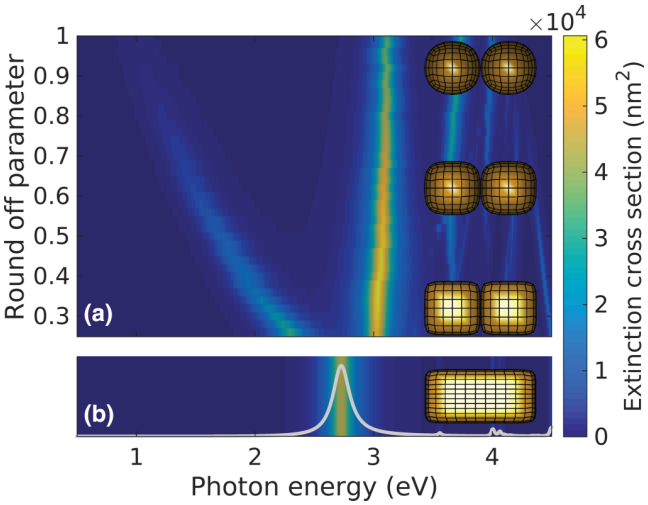

FIG. 3. (a) Morphing from two coupled spheres (rounding parameter $r = 1$) to two coupled cubes ($r = 0.25$). The density plot reports the extinction cross section for a gap separation of 0.6 nm, for a light polarization along the nanoparticle connections, and for a tunnel conductivity of 2.49×10^5 S/m representative for BDT. Similarly to Fig. 2, we consider tunneling within a distance region of 0.6–0.8 nm, as further discussed in the text. In the insets we report the geometries for three selected structures. (b) Extinction spectrum for a cuboid whose side length is twice the cube side length.

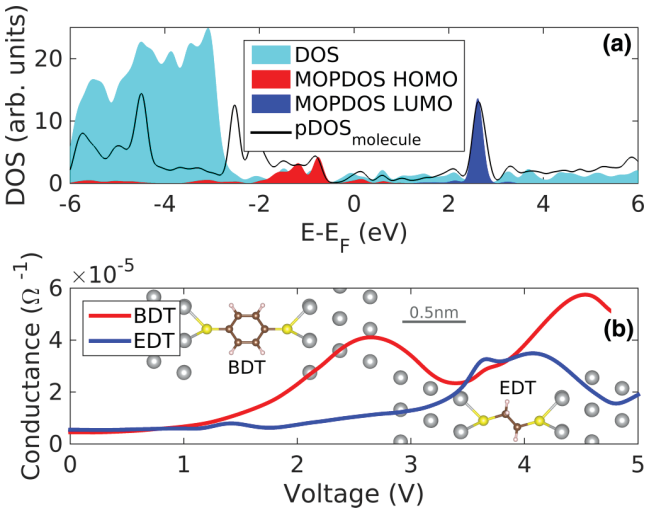

FIG. 4. Density functional theory (DFT) simulations for the conductance through the BDT and EDT molecules. (a) Density of states (DOS) for BDT junction as obtained from the VASP code [22,23]. We show the total and projected DOS (see text for details). (b) Conductance through molecular BDT and EDT junctions (see inset for simulated structures) as computed with the TRANSIESTA code [24,25].

We finally analyze the tunnel conductivities of the molecular junctions of Tan *et al.* [7] consisting of aromatic 1,4-benzenedithiolates (BDT) and saturated aliphatic 1,2-ethanedithiolates (EDT) molecules. The authors have estimated values of 2.49×10^5 S/m for BDT and 9.16×10^4 S/m for EDT. As a separate estimate for these values, we have calculated the ground state electronic structure and transport properties of the BDT and EDT junctions by *ab initio* density functional calculations. In a first step, we have relaxed the junction geometries and computed the ground state electronic structure by adopting a repeated slab approach using five silver layers on each side of the junction. For these calculations we have used the VASP code [22,23] employing projector augmented wave (PAW) potentials and have optimized the gap separation, the geometry of the two topmost Ag layers on each side of the junction, as well as all molecular coordinates. The resulting geometries for both types of molecules and the electronic structure for the BDT junction are depicted in panels (a) and (b) of Fig. 4, respectively. From the density of states projected onto the molecular orbital of the free molecules (MOP-DOS), we see that the LUMO of BDT, located 2.5 eV above the Fermi level, only weakly hybridizes with the silver surface, while the HOMO is spread between −2.0 and −0.5 eV below E_F indicating a stronger hybridization with the substrate. The overall DOS is dominated by Ag *d* states which appear at a binding energy of about −3.0 eV. In a second step, we have computed the ballistic electron transport through the molecular junctions by using the TRANSIESTA code [24,25] which is based on the Landauer-Büttiker formalism. Using a double zeta, polarized (DZP) basis set, which has been validated by comparing with our VASP DOS results, we have computed the conductance through BDT and EDT junctions as a function of the junction bias, as depicted in panel (b). At low voltages the conductance of EDT is slightly larger than that of BDT due to the smaller junction width of the latter. At bias voltages above 1 and 3 eV, the BDT junction clearly exhibits a larger conductance owing to the fact that the frontier HOMO and LUMO orbitals are located closer to E_F in BDT as compared to EDT. The low-voltage conductance relevant for the small electric fields of EELS excitations is about 0.5×10^{-5} S for both BDT and EDT, which corresponds to 0.0645 G_0 in units of the conductance quantum G_0. This value is somewhat smaller than the estimated 0.46 G_0 (BDT) and 0.20 G_0 (EDT) of Ref. [7], but is of the same order of magnitude, although one can expect that misalignment of molecules in the junction or finite temperatures will lead to even smaller values [26].

We are now in the position to critically examine the work of Tan *et al.* [7]. First, our results are in disagreement with their finite element method (FEM) simulations which showed in the extinction spectra an additional peak at photon energies below 1 eV that was interpreted as a CTP. In this paper we have motivated why such a low-energy peak should not appear in the spectra (we additionally performed finite difference time domain—FDTD—simulations with the Lumerical software, for rounded nanocubes with and without a conductivity layer in between the cubes, to confirm the absence of such a peak). Our most striking argument, in agreement with Esteban *et al.* [10], concerns the morphology of the gap: As can be clearly be seen in Fig. 3, the modification of the gap termination from round (spheres) to flat (cubes) comes along with a continuous blueshift of the CTP, whose energy finally falls together with that of the bonding mode. Additionally, for dimers with "negative gap distances," i.e., coalescing spheres or a cuboid with a side length of twice the cube side length, the SP energies of the dipole modes approximately agree with

those of the CTPs. As the cuboid has a dipole SP energy at about 2.7 eV, we exclude the possibility of a sub-eV CTP for two tunnel-coupled cubes.

After submission of our paper we became aware [27] that Tan *et al.* do not use a constant tunnel conductivity σ_0, but rather a frequency dependent expression $\sigma(\omega) = \sigma_0/(1 - i\omega\tau)$ that corresponds to a Drude-type permittivity

$$\varepsilon_{\text{Drude}}(\omega,\ell) = 1 - \frac{\tilde{\omega}_p^2}{\omega(\omega + i/\tau)}, \quad \tilde{\omega}_p = \sqrt{\frac{\sigma_0}{\varepsilon_0\tau}}, \qquad (2)$$

with τ being a collision time. The effective plasma frequency $\tilde{\omega}_p$ depends on the conductivity σ_0 which is computed from quantum mechanical tunneling theory [7,9]. Inserting the permittivity of Eq. (2) into our BEM simulations and using a collision time $\tau = 30$ fs, representative for silver, we indeed observed a low-energy peak in our EEL and extinction spectra. It should be noted first that the use of Eq. (2) was previously not mentioned [7] and that related work for molecular tunnel junctions used a constant σ_0 [8], in accordance to our approach.

So why does $\varepsilon_{\text{Drude}}$ give a low-energy peak in contrast to a frequency independent σ_0? We believe that the low-energy peak in the simulations is due to collective excitations $\text{Re}[\varepsilon_{\text{Drude}}(\omega \approx \tilde{\omega}_p)] = 0$ built into the Drude model. These resonances correspond to bulk plasmons of the (fictitious) charge carriers of the tunnel material. Setting for silver $\hbar\omega_p = 9$ eV and $\sigma_{\text{Ag}} = 6.3\times10^7$ S/m, we get for the BDT conductivity an effective plasmon energy $\hbar\tilde{\omega}_p = \hbar\omega_p\sqrt{\sigma_0/\sigma_{\text{Ag}}} \approx 0.6$ eV which is similar to the CTP energy found by Tan *et al.* [7]. To make things clear, this resonance has nothing to do with a CTP or any type of plasmonic enhancement, but is a genuine absorption peak of the tunnel material. Indeed, we found EEL and extinction peaks at precisely the same energy for tunnel-coupled spheres or planar layers.

We next argue why we consider a constant σ_0 to be a much more reasonable choice. First, the conductivity in the molecular tunnel junction is due to tunneling and not to free carriers subject to collisions. In the static case one can compute σ_0 from tunneling theory [1,6,9] or in the (related) Landauer-Büttiker formalism built into the TRANSIESTA code, as we do in our paper. In the time dependent case and for small frequencies, we can adopt the same reasoning as Esteban *et al.* [1,6] and assume that the modulation of the electric field is slow in comparison to the tunnel process, such that we can describe the system quasiadiabatically (coming back to the static case). In this approximation, which we assume to be valid in the sub-eV regime, the field is slowly changing and electrons tunnel in presence of the respective field. This approximation yields a constant σ_0. It is also unclear to us why one should describe tunneling using a collision time τ. How would one interpret these collisions? And which value should be chosen for τ? Finally, even if σ_0 has a frequency dependence, say even by a few orders of magnitude, Fig. 2 shows that this would not change dramatically our conclusions: Conductivity only triggers the appearance of the CTP peak but has otherwise no dramatic impact. For all these reasons we think that the interpretation of the low-energy peak in the EEL spectra of Tan *et al.* in terms of a CTP is not justified by the simulation results, thus calling for a reconsideration of the experimental findings. We hope that our work will trigger further research in this direction.

This work has been supported in part by the Austrian science fund FWF under the SFB F49 NextLite and P27299-N27, and NAWI Graz. We gratefully acknowledge Rudolf Bratschitsch for granting access to the FDTD software.

[1] R. Esteban, A. G. Borisov, P. Nordlander, and J. Aizpurua, Nat. Commun. **3**, 825 (2012).
[2] S. A. Maier, *Plasmonics: Fundamentals and Applications* (Springer, Berlin, 2007).
[3] K. J. Savage, M. M. Hawkeye, R. Esteband, A. G. Borisov, J. Aizpurua, and J. J. Baumberg, Nature (London) **491**, 574 (2012).
[4] H. Duan, A. I. Fernandez-Dominguez, M. Bosman, S. A. Maier, and J. K. W. Yang, Nano Lett. **12**, 1683 (2012).
[5] J. A. Scholl, A. Garcia-Etxarri, A. Leen Koh, and J. A. Dionne, Nano Lett. **13**, 564 (2013).
[6] R. Esteban, A. Zugarramurdi, P. Zhang, P. Nordlander, F. J. Garcia-Vidal, A. G. Borisov, and J. Aizpurua, Faraday Discuss. **178**, 151 (2015).
[7] S. F. Tan, L. Wu, J. K. W. Yang, P. Bai, M. Bosman, and C. A. Nijhuis, Science **343**, 1496 (2014).
[8] F. Benz, C. Tserkezis, L. O. Herrmann, B. de Nijs, A. Sanders, D. O. Sigle, L. Pukenas, S. D. Evans, J. Aizpurua, and J. J. Baumberg, Nano Lett. **15**, 669 (2015).
[9] L. Wu, H. Duan, P. Bai, M. Bosman, J. K. W. Wang, and E. Li, ACS Nano **7**, 707 (2013).
[10] R. Esteban, G. Aguirregabiria, A. G. Borisov, Y. M. Wang, P. Nordlander, G. W. Bryant, and J. Aizpurua, ACS Photon. **2**, 295 (2015).
[11] U. Hohenester and A. Trügler, Comput. Phys. Commun. **183**, 370 (2012).
[12] U. Hohenester, Comput. Phys. Commun. **185**, 1177 (2014).
[13] J. Waxenegger, A. Trügler, and U. Hohenester, Comput. Phys. Commun. **193**, 138 (2015).
[14] U. Hohenester, Phys. Rev. B **91**, 205436 (2015).
[15] F. Schmidt, H. Ditlbacher, F. Hofer, J. R. Krenn, and U. Hohenester, Nano Lett. **14**, 4810 (2014).
[16] P. B. Johnson and R. W. Christy, Phys. Rev. B **6**, 4370 (1972).
[17] L. J. Sherry, S.-H. Chang, G. C. Schatz, R. P. Van Duyne, B. J. Wiley, and Y. Xia, Nano Lett. **5**, 2034 (2005).
[18] O. Nicoletti, F. de la Pena, R. W. Leary, D. J. Holland, C. Ducati, and P. A. Midgley, Nature (London) **502**, 80 (2013).
[19] J. A. Bordley, N. Hooshmand, and M. A. El-Sayed, Nano Lett. **15**, 3391 (2015).
[20] U. Hohenester, H. Ditlbacher, and J. Krenn, Phys. Rev. Lett. **103**, 106801 (2009).
[21] D. Langbein, J. Phys. Math. Gen. **9**, 627 (1976).

[22] G. Kresse and J. Hafner, Phys. Rev. B **47**, 558 (1993).
[23] G. Kresse and D. Joubert, Phys. Rev. B **59**, 1758 (1999).
[24] J. Soler, E. Artacho, J. D. Gale, A. Garcia, J. Junquera, P. Ordejon, and D. Sanchez-Portal, J. Phys.: Condens. Matter **14**, 2745 (2002).
[25] M. Brandbyge, J.-L. Mozos, P. Ordejón, J. Taylor, and K. Stokbro, Phys. Rev. B **65**, 165401 (2002).
[26] Y. Kim, T. Prietsch, A. Erbe, W. Belzig, and E. Scheer, Nano Lett. **11**, 3734 (2011).
[27] C. Nijhuis (private communication).

9 Conclusion and outlook

In this thesis we tackled the problem of imaging surface plasmon resonances with true nanometer resolution by using electron energy loss spectroscopy.

In more detail, we brought the juxtaposition between simulation and theory to a new level by using the exact specimen geometry, which was measured with electron tomography, in the simulations. Further, we developed a tomography scheme for electron energy loss spectroscopy, which reconstructs the optical properties of plasmonic nanoparticles in three dimensions.

9.1 Imaging plasmons

Surface plasmon resonances of metallic nanoparticles enable the manipulation of light at length scales beyond the diffraction limit. For resonances, which couple to the far field, spectral properties are well measured by conventional optical microscopy. Such common optical microscopy techniques are blind to resonances with vanishing dipole moment (dark modes) and the spatial resolution is restricted by the diffraction limit.

9.1.1 EELS imaging of surface plasmons

It is crucial for a detailed spectral and spatial resolution of surface plasmon resonances at metallic nanoparticles to utilize microscopy techniques, which are capable of measuring with the desired spectral and spatial resolution. By using electrons as a probe, the spatial resolution is increased dramatically and in addition dark modes are visible in the loss spectra. Recently published works show detailed maps of various geometries, including cubes [31], disks [26] and nanorods [111]. Further, dark modes are shown for a nanodisk [26] and gold nanoparticle chains [112].

Studies of nanowires and conceptually similar nanorods [111, 113] showed detailed maps of Fabry-Perot type modes and compared the results with analytic models of infinite cylinders. In paper 2 [114], we study silver nanowires and make a detailed comparison between experiment and theory. For that reason, we carried out simulations with the MNPBEM toolbox [18], which simulates the electron energy loss based on a boundary element approach and uses the theory described in chapter 2, for an idealized nanowire with spherical caps and smooth cylindrical body. We find, both in experiment and simulations, typical Fabry-Perot modes with nanometer spatial resolution. The comparison of the spectra yields good agreement. The broader resonance widths of the experimental spectra are attributed to the finite spectral resolution in experiment. By convolution of the simulated spectra with a Lorentz function we gain even better agreement, showing that theory and experiment matches very well. Further, we explored

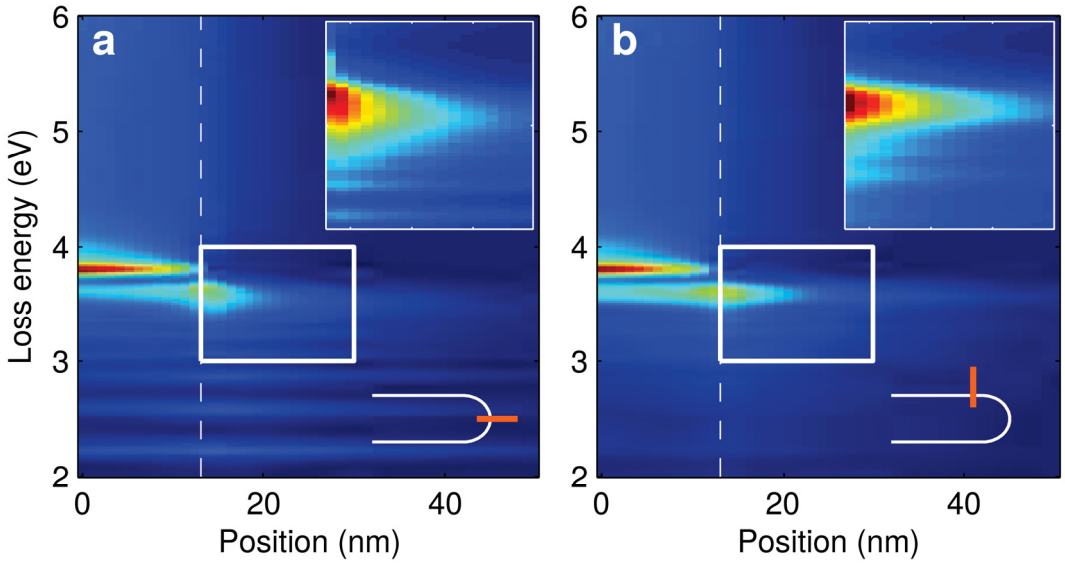

Figure 9.1: Simulation of silver nanowire. a) The electron beam position is varied at the longitudinal axis as can be seen in the insight. Fabry-Perot modes are visible in the spectrum and high order modes evolve into a continuum of modes at approximately 3.5 eV. A close up of the resonance at approximately 3.5 eV shows a stark variation of the resonance energy with respect to electron beam position. b) same as a), but for transverse positions. Here, multi-polar excitations show no decisive change with respect to electron beam position.

the detailed spatial energy dependence of multi-polar modes at energies approximately around 3.5 eV, when the electron beam is located in vicinity of the nanowire surface. We approach the nanowire surface either longitudinal or transversal from the longest wire axis, as can be seen in Fig. 9.1, and find, that due to the pseudo-spherical shape of the nanowire tip, the longitudinal path shows a stark variation of energy when approaching the surface. This effect occurs because higher order modes begin to contribute to the loss near the nanowire surface. For the transversal direction the effect is less pronounced, because of the cylindrical shape at the excitation path. Both findings are in agreement with analytical models of sphere and infinite cylinder and show that detailed inspections with nanometer resolution of surface plasmon resonances yield to new insights.

In paper 4 [82], we rectified the juxtaposition between experiment and simulation for two coupled silver nanorectangles, fabricated by means of electron beam lithography, by using the true three dimensional particle shapes in the simulations. The shape of the particles was found by tomographic reconstruction (described in chapter 3). As input for the tomographic reconstruction we used high angle annular dark-field images measured with an electron microscope. Using the true particle shape in the simulation with the MNPBEM toolbox yields even better agreement between theory and experiment as can

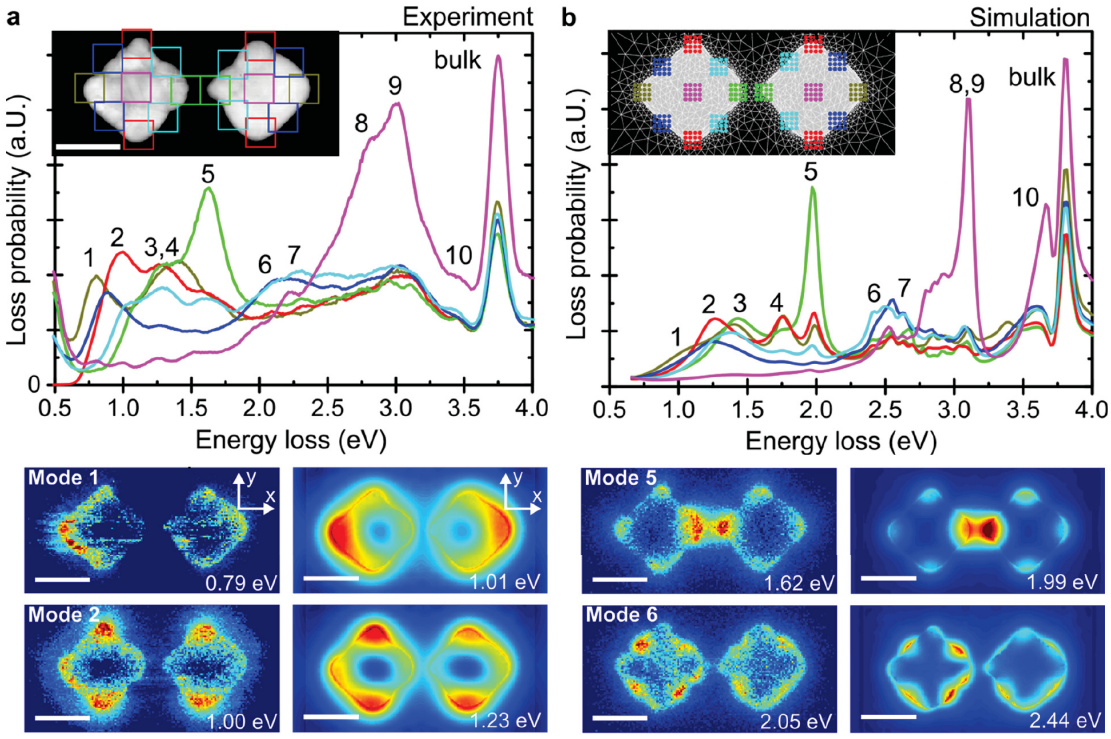

Figure 9.2: Juxtaposition between simulation and experiment for silver coupled rectangular particles. a) Cumulative spectrum of the electron energy loss for different areas depicted by colored squares. The numbered peaks in the spectra correspond to surface plasmon resonances. b) Same as a), but simulation results. A comparison between experiment and simulation for the spatial maps is shown for mode 1, 2, 5 and 6.

be seen in Fig. 9.2. Both spectral and spatial simulation data correlate almost perfect with experiment. Even details in the spatial distribution of resonances are reproduced by the simulations. Slight differences in the spectra are attributed to the fact, that in the simulation a dielectric function of silver from optical experiments is used, which is different from the experimental specimen, where grain effects and contamination of the sample change the dielectric function. This work paves the way for detailed investigations of realistic and complex plasmonic materials and overcomes the need of symmetry or geometrical assumptions of the specimen in the simulations.

9.1.2 Charge transfer plasmon

When metallic nanoparticles come close together, a tunneling current between the particles occurs, leading to new plasmon phenomena, namely charge transfer plasmons. These were observed in experiment with electron energy loss spectroscopy for two silver nanocubes and a molecular tunneling junction between the gap [59], in order to let

a tunneling current flow for experimental achievable gap distances. The experimental results were strengthened by finite element simulations for a quantum corrected model [61].

In paper 5 [64] we theoretically explore a similar geometry of coupled silver nanocubes and search for the plasmon resonances by using a boundary element approach [18], supplemented with a quantum corrected model for boundary element methods [62]. Within our approach we could not find the low energy peak attributed to a charge transfer plasmon, measured in [59]. Our findings show transverse cavity modes rising at low energies, when the gap size is diminished, in accordance with [63]. Further, we showed that the charge transfer mode shifts to higher energies, when the gap morphology is changed from spherical to flat gap surfaces. These findings lead to the assumption that a low energy charge transfer plasmon peak for the special geometry of the experiment in [59] should not be present within the quantum corrected model.

The contradicting simulation results in [59] are attributed to a frequency dependent gap conductivity leading to a drude type dielectric function, which shows a resonance at the plasma frequency and usually is used to account for free carriers subject to collisions. In contrast, our work uses a frequency independent dielectric function, which only accounts for the tunneling effect and not for additional free carrier collisions in the gap region as is in accordance with other studies for molecular tunneling junctions [115].

9.2 Tomography of plasmons using EELS

In electron energy loss spectroscopy the energy loss due to interaction with a plasmon resonance of metallic nanoparticles can be measured, leading to two dimensional projections of the loss signal at certain resonance frequencies.

To gain more insight, we introduced a tomography scheme for this type of plasmon measurement, which reconstructs from the measurement data physical quantities connected with the surface plasmon resonances. First we showed that this works in principle if a number of assumptions is used in paper 1 [107], especially the quasi-static approximation. Later on we extended the work of paper 1 in paper 3 [57] to the retarded regime and introduced a reconstruction scheme, which accounts for the vectorial character of the problem, and reconstructed the local density of states of plasmon resonances.

9.2.1 Quasi-static approximation

In paper 1 [107] we reformulated electron energy loss spectroscopy as a tomography problem, by using a quasi-static eigenmode expansion [43, 42] and a modal decomposition of the induced Green function [44] yielding to a modal representation of the EELS signal. Within this modal representation one can reconstruct from EELS data the eigenmode potential of a surface plasmon resonance with a simple inverse Radon transformation.

Although this approach works and has more or less simple reconstruction schemes (see. chapter 3), a lot of assumptions and restrictions need to be made: e.g. single mode approximation, quasi-static approximation, and unique sign of the eigenmode potential at a reconstruction plane.

Some of this assumptions can be lifted by solving an inverse problem and searching for the surface charges. In [108] this approach was used and extended to prevent spurious solutions of the surface charges.

9.2.2 Retarded regime

In the retarded regime the vectorial character of the electromagnetic fields has to be accounted for and the reconstruction gets quite complicated. To introduce a general scheme that links EELS with a meaningful physical quantity, we employed an eigenmode decomposition for the full Maxwell equations, as depicted in chapter 2, and used a similar, although now vectorial, decomposition of the dyadic Green function. A simple least square fit of the measurement data with the model did not lead to a solution, that is consistent with the optical properties of the specimen. Therefore a regularization term was introduced in the reconstruction process, accounting for the sparse character of the eigenmode basis used for the decomposition of the dyadic Green function. In other words, we applied compressed sensing optimization to the inverse problem and we found excellent agreement between the reconstructed and the simulated optical properties for different particle shapes, see paper 3 [57].

9.3 Connection between EELS and LDOS

Previous studies tried to link the energy loss of a swift electron with a meaningful physical quantity, the photonic local density of states, which shows how an oscillating dipole interacts at a certain position in space with the sample.

In [38], the authors showed, that EELS can be linked to a generalized local density of states, which is local in the impact parameter of the electron beam and local in the Fourier transform of the electron trajectory axis. A direct link is shown for special symmetric samples, e.g. planar structures.

A continuative study [65] argued, that a link between local density of states and EELS unfortunately is not as clear as wanted. For example, EELS can be blind to hot-spots with high local density of states for certain coupled plasmonic nanoparticles, see e.g. [66].

With paper 1 [107] and paper 3 [57] we showed, that indeed a link between the optical properties of plasmonic nanoparticles and the loss suffered by a swift electron in vicinity of the specimen is apparent, but one has to gain additional EELS data by tilting the sample.

9.4 Outlook

Electron energy loss spectroscopy has become in the last couple of years a versatile tool to image surface plasmons at the nanometer scale.

Although the comparison of simulation and experiment leads to very good accordance, it would be beneficial to have as an input for simulations not only the true geometry

of the particle, but also the true dielectric function. This would lead to even better agreement.

The reconstruction schemes for plasmon tomography, which are developed during this thesis could be improved at various corners, including especially a more general expansion of the dyadic Green tensor and therefore the inclusion of substrate effects and intrusion. Further, a study with experimental data for plasmon tomography would be nice which is already in progress. To obtain additional knowledge, especially of the phase information, electron holography could lead to progress in the field of plasmon tomography.

Future directions of the field of plasmon imaging are probably hard to detect, but maybe advances in spectral resolution lead to new applications. More general, exciting plasmons with swift electrons and measuring the optical response by cathodoluminescence, is an emerging field and promising, yet it is challenging to detect enough light in the measurements. Another promising microscopy technique called photon-induced near-field electron microscopy (PINEM) with nanometer resolution has shown to film the time evolution of surface plasmons and is heavily investigated at the moment, possibly leading to time resolved plasmon measurements.

Appendix

9.5 Eigenmodes and proof of the orthogonality of eigenmodes in the quasi-static regime

This result was first derived in [43]. We start with the equation for the potential in the quasi-static case in the ad hoc form, which reads [18, 78]

$$\phi = \oint_{\partial\Omega} \mathbf{G}(\mathbf{s},\mathbf{s}')\sigma(\mathbf{s}',\omega)ds' + \phi_{ext}(\mathbf{s},\omega) \tag{9.1}$$

and the boundary condition on the surface between two materials

$$\epsilon_1\phi_1'(\mathbf{s},\omega) = \epsilon_2\phi_2'(\mathbf{s},\omega), \tag{9.2}$$

where the prime indicates the derivative taken with respect to $\mathbf{n}$, the surface normal vector. By evaluating this derivative for Eq. (9.1), inserting into Eq. (9.2), and simple manipulations we get

$$(\epsilon_2+\epsilon_1)2\pi\sigma(\mathbf{s},\omega) + (\epsilon_2-\epsilon_1)\oint_{\partial\Omega}\mathbf{F}(\mathbf{s},\mathbf{s}')\sigma(\mathbf{s}',\omega) = -(\epsilon_2-)\epsilon_1)\phi_{ext}'(\mathbf{s},\omega), \tag{9.3}$$

where $\mathbf{F}(\mathbf{s},\mathbf{s}') = \partial\mathbf{G}(\mathbf{s},\mathbf{s}')/\partial n$ is the derivative with respect to the surface normal. By introducing a factor $\Lambda(\omega) = 2\pi(\epsilon_2+\epsilon_1)/(\epsilon_2-\epsilon_1)$, which is only dependent on the material parameters ϵ_1 and ϵ_2, we rewrite Eq. (9.3) as

$$\Lambda(\omega)\sigma(\mathbf{s},\omega) + \oint_{\partial\Omega}\mathbf{F}(\mathbf{s},\mathbf{s}')\sigma(\mathbf{s},\omega) = -\phi_{ext}(\mathbf{s},\omega). \tag{9.4}$$

This is an integral equation for the surface charges on the boundary between two adjacent materials. By discretizing the boundary one obtains a set of linear equations, which can be solved for σ.

Now we introduce an eigenmode expansion

$$\sigma(\mathbf{s},\omega) = \sum_i c_i(\omega)\sigma_i(\mathbf{s}) \tag{9.5}$$

where the modes are defined by the integral equation

$$\oint_{\partial\Omega}\mathbf{F}(\mathbf{s},\mathbf{s}')\sigma_i(\mathbf{s}') = \lambda_i\sigma_i(\mathbf{s}). \tag{9.6}$$

Here, λ_i are the eigenvalues of the operator $\mathbf{F}$.

9.6 Orthogonality of eigenmodes

the orthogonality of the eigenmodes [43, 42] in Eq. (9.6) is not straightforward and therefore we show the derivation.

The surface derivative on in- and outside of the eigenmode potential $\phi_i(\mathbf{s}) = \oint_{\partial\Omega} \mathbf{G}(\mathbf{s},\mathbf{s}')\sigma_i(\mathbf{s}')$ are given by

$$\phi'_{i1}(\mathbf{s}) = -2\pi\sigma_i(\mathbf{s}) + \oint_{\partial\Omega} ds'\mathbf{F}(\mathbf{s},\mathbf{s}')\sigma_i(\mathbf{s}') = (\lambda_i - 2\pi)\sigma_i(\mathbf{s}) \tag{9.7}$$

$$\phi'_{i2}(\mathbf{s}) = +2\pi\sigma_i(\mathbf{s}) + \oint_{\partial\Omega} ds'\mathbf{F}(\mathbf{s},\mathbf{s}')\sigma_i(\mathbf{s}') = (\lambda_i + 2\pi)\sigma_i(\mathbf{s}) \tag{9.8}$$

By subtracting and adding the above equations, respectively, and by using the continuity of the potential at the boundary, one obtains

$$\lambda_i(\phi'_{i2}(\mathbf{s}) - \phi'_{i1}(\mathbf{s})) = 2\pi(\phi'_{i2}(\mathbf{s}) - \phi'_{i1}(\mathbf{s})) \tag{9.9}$$

$$(2\pi - \lambda_i)\phi'_{i2}(\mathbf{s}) = -(2\pi + \lambda_i)\phi'_{i1}(\mathbf{s}). \tag{9.10}$$

Multiplying the above equation with the eigenmode potential ϕ_j and taking the integral over the boundary gives

$$(2\pi - \lambda_i)\oint_{\partial\Omega} \phi_j(\mathbf{s})\phi'_{i2}(\mathbf{s})da = -(2\pi + \lambda_i)\oint_{\partial\Omega} \phi_j(\mathbf{s})\phi'_{1i}(\mathbf{s})da. \tag{9.11}$$

By using Green's first identity and the fact, that $\nabla^2\phi_i = 0$ away from the boundary, we arrive at

$$(2\pi - \lambda_i)\int_{V2} \mathbf{E}_{2i}\cdot\mathbf{E}_{2j}dV = -(2\pi + \lambda_i)\int_{V1} \mathbf{E}_{1i}\cdot\mathbf{E}_{1j}dV. \tag{9.12}$$

By starting with the surface derivative of the eigenpotentials of mode j, we can also derive

$$(2\pi - \lambda_j)\int_{V_2} \mathbf{E}_{2i}\cdot\mathbf{E}_{2j}dV = -(2\pi + \lambda_j)\int_{V_1} \mathbf{E}_{1i}\cdot\mathbf{E}_{1j}dV. \tag{9.13}$$

By inspecting Eq. (9.12) and (9.13), we find that, if $\lambda_i \neq \lambda_j$, then

$$\int_{V_{1,2}} \mathbf{E}_i\cdot\mathbf{E}_j = 0. \tag{9.14}$$

If we use Green's identity in backward direction, we get

$$\int_V \mathbf{E}_i\cdot\mathbf{E}_j = \oint_{\partial\Omega} \phi_i(\mathbf{s})\phi'_j(\mathbf{s})da \tag{9.15}$$

and by using Eq. (9.8)

$$\oint_{\partial\Omega} \phi_i(\mathbf{s})(\lambda_j - 2\pi)\sigma_j(\mathbf{s})da = 0 \tag{9.16}$$

$$\oint_{\partial\Omega} \phi_i(\mathbf{s})(\lambda_j + 2\pi)\sigma_j(\mathbf{s}')da = 0 \tag{9.17}$$

at inside and outside, respectively. By adding the above equations we arrive at the final result:

$$\oint_{\partial\Omega} \sigma_i(\mathbf{s})\mathbf{G}(\mathbf{s},\mathbf{s}')\sigma_j(\mathbf{s}')dada' = 0 \tag{9.18}$$

for $i \neq j$.

9.7 Expansion of induced Green function in terms of eigenmodes

The induced Green function can be expanded in terms of eigenmodes [116]. First, we insert Eq. (9.5) into Eq. (9.4). Then we get by using Eq. (9.6)

$$\sum_j (\Lambda(\omega) + \lambda_j) C_j \sigma_j(\mathbf{s}) = -\phi'_{ext}(\mathbf{s}, \omega) \tag{9.19}$$

Using the orthogonality relation derived in the last section, we get

$$(\Lambda(\omega) + \lambda_i) C_i = -\oint_{\partial\Omega} \sigma_i(\mathbf{s}') \mathbf{G}(\mathbf{s}', \mathbf{s}) \phi'_{ext}(\mathbf{s}, \omega) ds' ds. \tag{9.20}$$

Expressing the last equation for the coefficients C_i the eigenmode potential reads within the eigenmode expansion as

$$\phi(\mathbf{r}) = -\sum_i (\Lambda(\omega) + \lambda_i)^{-1} \oint_{\partial\Omega} \mathbf{G}(\mathbf{r}, \mathbf{s}) \sigma_i(\mathbf{s}) ds \oint_{\partial\Omega} \sigma_i(\mathbf{s}') \mathbf{G}(\mathbf{s}', \mathbf{s}'') \phi'_{ext}(\mathbf{s}'', \omega) ds' ds''. \tag{9.21}$$

For the potential of a unit charge at position $\mathbf{r}'$ the last integrals become

$$\oint_{\partial\Omega} \sigma_i(\mathbf{s}') \mathbf{G}(\mathbf{s}', \mathbf{s}'') \mathbf{F}(\mathbf{s}'', \mathbf{r}') \frac{1}{\epsilon(\mathbf{r}')} ds' ds''. \tag{9.22}$$

From Green's theorem

$$\oint_{\partial\Omega} \mathbf{G} \partial\mathbf{G}/\partial n da = \oint_{\partial\Omega} \partial\mathbf{G}/\partial n \mathbf{G} da - \int_\Omega (\mathbf{G}\nabla^2\mathbf{G} - (\nabla^2\mathbf{G})\mathbf{G}) d\tau)$$

we find (second term vanishes for $\mathbf{r} \notin \Omega$)

$$\oint_{\partial\Omega} \mathbf{G}(\mathbf{r}, \mathbf{s}'') \mathbf{F}(\mathbf{s}'', \mathbf{r}') ds'' = \oint_{\partial\Omega} \mathbf{F}(\mathbf{r}, \mathbf{s}'') \mathbf{G}(\mathbf{s}'', \mathbf{r}') ds''. \tag{9.23}$$

Taking the limit $\mathbf{r} \to \mathbf{s}'$ we find

$$\lim_{\mathbf{r}\to\mathbf{s}'} \oint_{\partial\Omega} \mathbf{F}(\mathbf{r}, \mathbf{s}'') \mathbf{G}(\mathbf{s}'', \mathbf{r}') ds'' = \pm 2\pi \mathbf{G}(\mathbf{s}'', \mathbf{r}') + \oint_{\partial\Omega} \mathbf{F}(\mathbf{s}', \mathbf{s}'') \mathbf{G}(\mathbf{s}', \mathbf{r}') ds', \tag{9.24}$$

where the plus/minus sign depends on whether we approach the surface from out- or inside, respectively. Inserting the findings of Eq. (9.24) into Eq. (9.21) and using the integral equation Eq. (9.6) we arrive at

$$\phi(\mathbf{r}) = -\sum_i \frac{\lambda_i \pm 2\pi}{\Lambda(\omega) + \lambda_i} \phi_i(\mathbf{r}) \phi_i(\mathbf{r}') \frac{1}{\epsilon(\mathbf{r}')}, \tag{9.25}$$

and therefore as we derived the above equation for a unit charge located at $\mathbf{r}'$ we find the eigenmode decomposition of the induced Green function

$$\mathbf{G}(\mathbf{r}, \mathbf{r}') = -\sum_i \frac{\lambda_i \pm 2\pi}{\Lambda(\omega) + \lambda_i} \phi_i(\mathbf{r}) \phi_i(\mathbf{r}') \frac{1}{\epsilon(\mathbf{r}')}. \tag{9.26}$$

Bibliography

[1] H. A. Atwater, "The Promise of Plasmonics," *Scientific American*, vol. 296, no. 4, pp. 56–62, 2007.

[2] L. M. Liz-Marzán, "Tailoring surface plasmons through the morphology and assembly of metal nanoparticles," *Langmuir*, vol. 22, no. 1, pp. 32–41, 2006.

[3] P. Dombi, A. Hörl, P. Rácz, I. Márton, A. Trügler, J. R. Krenn, and U. Hohenester, "Ultrafast Strong-Field Photoemission from Plasmonic Nanoparticles," *Nano Letters*, vol. 13, no. 2, pp. 674–678, 2013. PMID: 23339740.

[4] R. W. Wood, "On a remarkable case of uneven distribution of light in a diffraction grating spectrum," *The London, Edinburgh, and Dublin Philosophical Magazine and Journal of Science*, vol. 4, no. 21, pp. 396–402, 1902.

[5] L. Rayleigh, "On the dynamical theory of gratings," *Proceedings of the Royal Society of London. Series A, Containing Papers of a Mathematical and Physical Character*, vol. 79, no. 532, pp. 399–416, 1907.

[6] G. Mie, "Beiträge zur Optik trüber Medien, speziell kolloidaler Metallösungen," *Annalen der Physik*, vol. 330, no. 3, pp. 377–445, 1908.

[7] R. Ritchie, "Plasma losses by fast electrons in thin films," *Physical Review*, vol. 106, no. 5, p. 874, 1957.

[8] C. Powell and J. Swan, "Origin of the characteristic electron energy losses in aluminum," *Physical Review*, vol. 115, no. 4, p. 869, 1959.

[9] E. Kretschmann and H. Raether, "Radiative decay of non radiative surface plasmons excited by light," *Zeitschrift für Naturforschung A*, vol. 23, no. 12, pp. 2135–2136, 1968.

[10] A. Otto, "Excitation of nonradiative surface plasma waves in silver by the method of frustrated total reflection," *Zeitschrift für Physik*, vol. 216, no. 4, pp. 398–410, 1968.

[11] M. E. Stewart, C. R. Anderton, L. B. Thompson, J. Maria, S. K. Gray, J. A. Rogers, and R. G. Nuzzo, "Nanostructured plasmonic sensors," *Chemical Reviews*, vol. 108, no. 2, pp. 494–521, 2008.

[12] V. Leitgeb, A. Trügler, S. Kostler, M. K. Krug, U. Hohenester, A. Hohenau, A. Leitner, and J. R. Krenn, "Three dimensional sensitivity characterization of plasmonic nanorods for refractometric biosensors," *Nanoscale*, vol. 8, pp. 2974–2981, 2016.

[13] X. Huang and M. A. El-Sayed, "Plasmonic photo-thermal therapy (PPTT)," *Alexandria Journal of Medicine*, vol. 47, no. 1, pp. 1–9, 2011.

[14] D. K. Gramotnev and S. I. Bozhevolnyi, "Plasmonics beyond the diffraction limit," *Nature Photonics*, vol. 4, no. 2, pp. 83–91, 2010.

[15] L. Novotny and B. Hecht, *Principles of Nano-Optics*. Cambridge University Press, 2006. Cambridge Books Online.

[16] P. B. Johnson and R. W. Christy, "Optical Constants of the Noble Metals," *Physical Review B*, vol. 6, pp. 4370–4379, Dec 1972.

[17] F.-P. Schmidt, H. Ditlbacher, U. Hohenester, A. Hohenau, F. Hofer, and J. R. Krenn, "Universal dispersion of surface plasmons in flat nanostructures," *Nature Communications*, vol. 5, 2014.

[18] U. Hohenester and A. Trügler, "MNPBEM – A Matlab toolbox for the simulation of plasmonic nanoparticles," *Computer Physics Communications*, vol. 183, no. 2, pp. 370 – 381, 2012.

[19] U. Hohenester and J. Krenn, "Surface plasmon resonances of single and coupled metallic nanoparticles: A boundary integral method approach," *Physical Review B*, vol. 72, no. 19, p. 195429, 2005.

[20] U. Dürig, D. W. Pohl, and F. Rohner, "Near–field optical–scanning microscopy," *Journal of Applied Physics*, vol. 59, no. 10, pp. 3318–3327, 1986.

[21] M. Bosman, V. J. Keast, M. Watanabe, A. I. Maaroof, and M. B. Cortie, "Mapping surface plasmons at the nanometre scale with an electron beam," *Nanotechnology*, vol. 18, no. 16, p. 165505, 2007.

[22] J. Nelayah, M. Kociak, O. Stephan, F. J. Garcia de Abajo, M. Tence, L. Henrard, D. Taverna, I. Pastoriza-Santos, L. M. Liz-Marzan, and C. Colliex, "Mapping surface plasmons on a single metallic nanoparticle," *Nature Physics*, vol. 3, pp. 348–353, May 2007.

[23] F. J. García de Abajo, "Optical excitations in electron microscopy," *Reviews of Modern Physics*, vol. 82, pp. 209–275, Feb 2010.

[24] J. Hillier and R. Baker, "Microanalysis by means of electrons," *Journal of Applied Physics*, vol. 15, no. 9, pp. 663–675, 1944.

[25] C. Cherqui, N. Thakkar, G. Li, J. P. Camden, and D. J. Masiello, "Characterizing Localized Surface Plasmons Using Electron Energy-Loss Spectroscopy," *Annual Review of Physical Chemistry*, vol. 67, no. 1, 2016.

[26] F.-P. Schmidt, H. Ditlbacher, U. Hohenester, A. Hohenau, F. Hofer, and J. R. Krenn, "Dark plasmonic breathing modes in silver nanodisks," *Nano Letters*, vol. 12, no. 11, pp. 5780–5783, 2012.

[27] J. A. Scholl, A. L. Koh, and J. A. Dionne, "Quantum plasmon resonances of individual metallic nanoparticles," *Nature*, vol. 483, no. 7390, pp. 421–427, 2012.

[28] J. A. Scholl, A. García-Etxarri, A. L. Koh, and J. A. Dionne, "Observation of Quantum Tunneling between Two Plasmonic Nanoparticles," *Nano Letters*, vol. 13, no. 2, pp. 564–569, 2013. PMID: 23245286.

[29] R. Egerton, "Electron energy-loss spectroscopy in the TEM," *Reports on Progress in Physics*, vol. 72, no. 1, p. 016502, 2008.

[30] B. Schaffer, W. Grogger, G. Kothleitner, and F. Hofer, "Comparison of EFTEM and STEM EELS plasmon imaging of gold nanoparticles in a monochromated TEM," *Ultramicroscopy*, vol. 110, no. 8, pp. 1087–1093, 2010.

[31] O. Nicoletti, F. de La Peña, R. K. Leary, D. J. Holland, C. Ducati, and P. A. Midgley, "Three-dimensional imaging of localized surface plasmon resonances of metal nanoparticles," *Nature*, vol. 502, no. 7469, pp. 80–84, 2013.

[32] M. Kociak and O. Stephan, "Mapping plasmons at the nanometer scale in an electron microscope," *Chemical Society Reviews*, vol. 43, pp. 3865–3883, 2014.

[33] J. Jackson, *Classical Electrodynamics*. Wiley, 1975.

[34] C. Tai, *Dyadic Green Functions in Electromagnetic Theory*. IEEE Press Series on Electromagnetic Waves, IEEE Press, 1994.

[35] R. E. Coilin, "Dyadic Green's Function Expansions in Spherical Coordinates," *Electromagnetics*, vol. 6, no. 3, pp. 183–207, 1986.

[36] L.-W. Li, P.-S. Kooi, M.-S. Leong, and T.-S. Yee, "Electromagnetic dyadic Green's function in spherically multilayered media," *Microwave Theory and Techniques, IEEE Transactions on*, vol. 42, pp. 2302–2310, Dec 1994.

[37] L.-W. Li, M.-S. Leong, T.-S. Yeo, and P.-S. Kooi, "Electromagnetic Dyadic Green's Functions in Spectral Domain for Multilayered Cylinders," *Journal of Electromagnetic Waves and Applications*, vol. 14, no. 7, pp. 961–985, 2000.

[38] F. J. García de Abajo and M. Kociak, "Probing the Photonic Local Density of States with Electron Energy Loss Spectroscopy," *Physical Review Letters*, vol. 100, p. 106804, Mar 2008.

[39] F. J. García de Abajo, "Relativistic energy loss and induced photon emission in the interaction of a dielectric sphere with an external electron beam," *Physical Review B*, vol. 59, pp. 3095–3107, Jan 1999.

[40] N. Zabala, A. Rivacoba, and P. Echenique, "Energy loss of electrons travelling through cylindrical holes," *Surface Science*, vol. 209, no. 3, pp. 465 – 480, 1989.

[41] F. J. García de Abajo and J. Aizpurua, "Numerical simulation of electron energy loss near inhomogeneous dielectrics," *Physical Review B*, vol. 56, pp. 15873–15884, Dec 1997.

[42] I. D. Mayergoyz, D. R. Fredkin, and Z. Zhang, "Electrostatic (plasmon) resonances in nanoparticles," *Physical Review B*, vol. 72, p. 155412, Oct 2005.

[43] F. Ouyang and M. Isaacson, "Surface plasmon excitation of objects with arbitrary shape and dielectric constant," *Philosophical Magazine B*, vol. 60, no. 4, pp. 481–492, 1989.

[44] G. Boudarham and M. Kociak, "Modal decompositions of the local electromagnetic density of states and spatially resolved electron energy loss probability in terms of geometric modes," *Physical Review B*, vol. 85, p. 245447, Jun 2012.

[45] P. T. Leung, S. Y. Liu, and K. Young, "Completeness and orthogonality of quasinormal modes in leaky optical cavities," *Physical Review A*, vol. 49, pp. 3057–3067, Apr 1994.

[46] H. E. Türeci, A. D. Stone, and B. Collier, "Self-consistent multimode lasing theory for complex or random lasing media," *Physical Review A*, vol. 74, p. 043822, Oct 2006.

[47] J. Mäkitalo, M. Kauranen, and S. Suuriniemi, "Modes and resonances of plasmonic scatterers," *Physical Review B*, vol. 89, p. 165429, Apr 2014.

[48] P. T. Kristensen and S. Hughes, "Modes and mode volumes of leaky optical cavities and plasmonic nanoresonators," *ACS Photonics*, vol. 1, no. 1, pp. 2–10, 2014.

[49] C. Sauvan, J. P. Hugonin, I. S. Maksymov, and P. Lalanne, "Theory of the Spontaneous Optical Emission of Nanosize Photonic and Plasmon Resonators," *Physical Review Letters*, vol. 110, p. 237401, Jun 2013.

[50] P. T. Kristensen, R.-C. Ge, and S. Hughes, "Normalization of quasinormal modes in leaky optical cavities and plasmonic resonators," *Physical Review A*, vol. 92, p. 053810, Nov 2015.

[51] Q. Bai, M. Perrin, C. Sauvan, J.-P. Hugonin, and P. Lalanne, "Efficient and intuitive method for the analysis of light scattering by a resonant nanostructure," *Optics Express*, vol. 21, pp. 27371–27382, Nov 2013.

[52] F. Alpeggiani, S. D'Agostino, D. Sanvitto, and D. Gerace, "Single-plasmon blockade from nanostructured metallic dimers," *ArXiv e-prints*, Aug. 2015.

[53] D. A. Powell, "Resonant dynamics of arbitrarily shaped meta-atoms," *Physical Review B*, vol. 90, p. 075108, Aug 2014.

[54] C. Sauvan, J. P. Hugonin, R. Carminati, and P. Lalanne, "Modal representation of spatial coherence in dissipative and resonant photonic systems," *Physical Review A*, vol. 89, p. 043825, Apr 2014.

[55] R.-C. Ge and S. Hughes, "Quasinormal mode theory and modelling of electron energy loss spectroscopy," *ArXiv e-prints*, Oct. 2015.

[56] J. Yang, H. Giessen, and P. Lalanne, "Simple Analytical Expression for the Peak-Frequency Shifts of Plasmonic Resonances for Sensing," *Nano Letters*, vol. 15, no. 5, pp. 3439–3444, 2015. PMID: 25844813.

[57] A. Hörl, A. Trügler, and U. Hohenester, "Full Three-Dimensonal Reconstruction of the Dyadic Green Tensor from Electron Energy Loss Spectroscopy of Plasmonic Nanoparticles," *ACS Photonics*, vol. 2, no. 10, pp. 1429–1435, 2015.

[58] M. S. Tame, K. McEnery, Ş. Özdemir, J. Lee, S. Maier, and M. Kim, "Quantum plasmonics," *Nature Physics*, vol. 9, no. 6, pp. 329–340, 2013.

[59] S. F. Tan, L. Wu, J. K. Yang, P. Bai, M. Bosman, and C. A. Nijhuis, "Quantum plasmon resonances controlled by molecular tunnel junctions," *Science*, vol. 343, no. 6178, pp. 1496–1499, 2014.

[60] M. Barbry, P. Koval, F. Marchesin, R. Esteban, A. G. Borisov, J. Aizpurua, and D. Sánchez-Portal, "Atomistic Near-Field Nanoplasmonics: Reaching Atomic-Scale Resolution in Nanooptics," *Nano Letters*, vol. 15, no. 5, pp. 3410–3419, 2015. PMID: 25915173.

[61] R. Esteban, A. G. Borisov, P. Nordlander, and J. Aizpurua, "Bridging quantum and classical plasmonics with a quantum-corrected model," *Nature Communications*, vol. 3, p. 825, 2012.

[62] U. Hohenester, "Quantum corrected model for plasmonic nanoparticles: A boundary element method implementation," *Physical Review B*, vol. 91, no. 20, p. 205436, 2015.

[63] R. Esteban, A. Zugarramurdi, P. Zhang, P. Nordlander, F. J. García-Vidal, A. G. Borisov, and J. Aizpurua, "A classical treatment of optical tunneling in plasmonic gaps: extending the quantum corrected model to practical situations," *Faraday Discussions*, vol. 178, pp. 151–183, 2015.

[64] D. Knebl, A. Hörl, A. Trügler, J. Kern, J. R. Krenn, P. Puschnig, and U. Hohenester, "Gap plasmonics of silver nanocube dimers," *ArXiv e-prints*, Jan. 2016.

[65] U. Hohenester, H. Ditlbacher, and J. R. Krenn, "Electron-Energy-Loss Spectra of Plasmonic Nanoparticles," *Physical Review Letters*, vol. 103, p. 106801, Aug 2009.

[66] F. von Cube, J. Niegemann, S. Irsen, D. C. Bell, and S. Linden, "Angular-resolved electron energy loss spectroscopy on a split-ring resonator," *Physical Review B*, vol. 89, p. 115434, Mar 2014.

[67] C. HAFNER and R. BALLISTI, "THE MULTIPLE MULTIPOLE METHOD (MMP)," *COMPEL - The international journal for computation and mathematics in electrical and electronic engineering*, vol. 2, no. 1, pp. 1–7, 1983.

[68] E. Moreno, D. Erni, C. Hafner, and R. Vahldieck, "Multiple multipole method with automatic multipole setting applied to the simulation of surface plasmons in metallic nanostructures," *Journal of the Optical Society of America A*, vol. 19, pp. 101–111, Jan 2002.

[69] L. Kiewidt, M. Karamehmedović, C. Matyssek, W. Hergert, L. Mädler, and T. Wriedt, "Numerical simulation of Electron Energy Loss Spectroscopy using a Generalized Multipole Technique," *Ultramicroscopy*, vol. 133, pp. 101 – 108, 2013.

[70] S. Thomas, C. Matyssek, W. Hergert, M. Arnold, L. Kiewidt, M. Karamehmedovic, and T. Wriedt, "Application of Generalized Mie Theory to EELS Calculations as a Tool for Optimization of Plasmonic Structures," *Plasmonics*, 2015.

[71] B. T. Draine, "The discrete-dipole approximation and its application to interstellar graphite grains," *The Astrophysical Journal*, vol. 333, pp. 848–872, 1988.

[72] B. T. Draine and P. J. Flatau, "Discrete-dipole approximation for scattering calculations," *The Journal of the Optical Society of America A*, vol. 11, no. 4, pp. 1491–1499, 1994.

[73] N. Geuquet and L. Henrard, "EELS and optical response of a noble metal nanoparticle in the frame of a discrete dipole approximation ," *Ultramicroscopy*, vol. 110, no. 8, pp. 1075 – 1080, 2010.

[74] N. W. Bigelow, A. Vaschillo, V. Iberi, J. P. Camden, and D. J. Masiello, "Characterization of the Electron- and Photon-Driven Plasmonic Excitations of Metal Nanorods," *ACS Nano*, vol. 6, no. 8, pp. 7497–7504, 2012. PMID: 22849410.

[75] K. Yee, "Numerical Solution of Initial Boundary Value Problem Involving Maxwell's Equations in Isotropic Media," *Antennas and Propagation, IEEE Transactions on*, vol. 14, pp. 302–307, May 1966.

[76] Y. Cao, A. Manjavacas, N. Large, and P. Nordlander, "Electron Energy-Loss Spectroscopy Calculation in Finite-Difference Time-Domain Package," *ACS Photonics*, vol. 2, no. 3, pp. 369–375, 2015.

[77] J. Stratton and L. Chu, "Diffraction theory of electromagnetic waves," *Physical Review*, vol. 56, no. 1, p. 99, 1939.

[78] F. J. García de Abajo and A. Howie, "Retarded field calculation of electron energy loss in inhomogeneous dielectrics," *Physical Review B*, vol. 65, p. 115418, Mar 2002.

[79] W. Śmigaj, T. Betcke, S. Arridge, J. Phillips, and M. Schweiger, "Solving Boundary Integral Problems with BEM++," *ACM Transactions on Mathematical Software*, vol. 41, pp. 6:1–6:40, Feb. 2015.

[80] J. Waxenegger, A. Trügler, and U. Hohenester, "Plasmonics simulations with the MNPBEM toolbox: Consideration of substrates and layer structures ," *Computer Physics Communications*, vol. 193, pp. 138 – 150, 2015.

[81] U. Hohenester, "Simulating electron energy loss spectroscopy with the MNPBEM toolbox," *Computer Physics Communications*, vol. 185, no. 3, pp. 1177 – 1187, 2014.

[82] G. Haberfehlner, A. Trügler, F. P. Schmidt, A. Hörl, F. Hofer, U. Hohenester, and G. Kothleitner, "Correlated 3D Nanoscale Mapping and Simulation of Coupled Plasmonic Nanoparticles," *Nano Letters*, vol. 15, no. 11, pp. 7726–7730, 2015. PMID: 26495933.

[83] J. Radon, "Über die Bestimmung von Funktionen durch ihre Integralwerte längs gewisser Mannigfaltigkeiten," *Akademie der Wissenschaften Leipzig*, vol. 69, pp. 262–277, 1917.

[84] L. A. Shepp and B. F. Logan, "The Fourier reconstruction of a head section," *Nuclear Science, IEEE Transactions on*, vol. 21, no. 3, pp. 21–43, 1974.

[85] P. Kuchment, "Generalized transforms of Radon type and their applications," in *PROCEEDINGS OF SYMPOSIA IN APPLIED MATHEMATICS*, vol. 63, p. 67, 2006.

[86] E. L. Dove, "Physics of Medical Imaging–An Introduction," 2003.

[87] A. C. Kak and M. Slaney, *Principles of computerized tomographic imaging*. Society for Industrial and Applied Mathematics, 2001.

[88] S. W. Smith, *The Scientist and Engineer's Guide to Digital Signal Processing*. California Technical Publishing, 1997. Available at www.dspguide.com.

[89] R. Gordon, R. Bender, and G. T. Herman, "Algebraic Reconstruction Techniques (ART) for three-dimensional electron microscopy and X-ray photography," *Journal of Theoretical Biology*, vol. 29, no. 3, pp. 471 – 481, 1970.

[90] J. R. Shewchuk, "An introduction to the conjugate gradient method without the agonizing pain," 1994.

[91] D. P. Bertsekas, "Nonlinear programming," 1999.

[92] E. J. Candes, J. K. Romberg, and T. Tao, "Stable signal recovery from incomplete and inaccurate measurements," *Communications on pure and applied mathematics*, vol. 59, no. 8, pp. 1207–1223, 2006.

[93] M. Lustig, D. Donoho, and J. M. Pauly, "Sparse MRI: The application of compressed sensing for rapid MR imaging," *Magnetic Resonance in Medicine*, vol. 58, no. 6, pp. 1182–1195, 2007.

[94] Y. Wang, J. Cao, and C. Yang, "Recovery of seismic wavefields based on compressive sensing by an l1-norm constrained trust region method and the piecewise random subsampling," *Geophysical Journal International*, vol. 187, no. 1, pp. 199–213, 2011.

[95] M. F. Duarte, M. A. Davenport, D. Takhar, J. N. Laska, T. Sun, K. E. Kelly, R. G. Baraniuk, *et al.*, "Single-pixel imaging via compressive sampling,"

[96] D. Gross, Y.-K. Liu, S. T. Flammia, S. Becker, and J. Eisert, "Quantum State Tomography via Compressed Sensing," *Physical Review Letters*, vol. 105, p. 150401, Oct 2010.

[97] Z. Saghi, D. J. Holland, R. Leary, A. Falqui, G. Bertoni, A. J. Sederman, L. F. Gladden, and P. A. Midgley, "Three-Dimensional Morphology of Iron Oxide Nanoparticles with Reactive Concave Surfaces. A Compressed Sensing-Electron Tomography (CS-ET) Approach," *Nano Letters*, vol. 11, no. 11, pp. 4666–4673, 2011. PMID: 21950497.

[98] E. J. Candè and M. B. Wakin, "An introduction to compressive sampling," *Signal Processing Magazine, IEEE*, vol. 25, no. 2, pp. 21–30, 2008.

[99] D. L. Donoho, "Compressed sensing," *Information Theory, IEEE Transactions on*, vol. 52, no. 4, pp. 1289–1306, 2006.

[100] D. Taubman and M. Marcellin, *JPEG2000 Image Compression Fundamentals, Standards and Practice: Image Compression Fundamentals, Standards and Practice*, vol. 642. Springer Science & Business Media, 2012.

[101] T. Tao, *Topics in random matrix theory*, vol. 132. American Mathematical Soc., 2012.

[102] F. Santosa and W. W. Symes, "Linear inversion of band-limited reflection seismograms," *SIAM Journal on Scientific and Statistical Computing*, vol. 7, no. 4, pp. 1307–1330, 1986.

[103] Y. Zhang, "User's Guide for YALL1: Your ALgorithms for L1 Optimization," *Technique report*, pp. 09–17, 2009.

[104] P. S. Carney, V. A. Markel, and J. C. Schotland, "Near-field tomography without phase retrieval," *Physical Review Letters*, vol. 86, no. 26, p. 5874, 2001.

[105] P. S. Carney and J. C. Schotland, "Near-field tomography," *Inside out: inverse problems and applications, Math. Sci. Res. Inst. Publ*, vol. 47, pp. 133–168, 2003.

[106] A. C. Atre, B. J. Brenny, T. Coenen, A. García-Etxarri, A. Polman, and J. A. Dionne, "Nanoscale optical tomography with cathodoluminescence spectroscopy," *Nature Nanotechnology*, 2015.

[107] A. Hörl, A. Trügler, and U. Hohenester, "Tomography of particle plasmon fields from electron energy loss spectroscopy," *Physical Review Letters*, vol. 111, no. 7, p. 076801, 2013.

[108] S. M. Collins, E. Ringe, M. Duchamp, Z. Saghi, R. E. Dunin-Borkowski, and P. A. Midgley, "Eigenmode Tomography of Surface Charge Oscillations of Plasmonic Nanoparticles by Electron Energy Loss Spectroscopy," *ACS Photonics*, vol. 2, no. 11, pp. 1628–1635, 2015.

[109] P. Müller, M. Schürmann, and J. Guck, "The Theory of Diffraction Tomography," *arXiv preprint arXiv:1507.00466*, 2015.

[110] B. Schaffer, U. Hohenester, A. Trügler, and F. Hofer, "High-resolution surface plasmon imaging of gold nanoparticles by energy-filtered transmission electron microscopy," *Physical Review B*, vol. 79, p. 041401, Jan 2009.

[111] O. Nicoletti, M. Wubs, N. A. Mortensen, W. Sigle, P. A. Van Aken, and P. A. Midgley, "Surface plasmon modes of a single silver nanorod: an electron energy loss study," *Optics Express*, vol. 19, no. 16, pp. 15371–15379, 2011.

[112] S. J. Barrow, D. Rossouw, A. M. Funston, G. A. Botton, and P. Mulvaney, "Mapping bright and dark modes in gold nanoparticle chains using electron energy loss spectroscopy.," *Nano Letters*, vol. 14, no. 7, pp. 3799–3808, 2014.

[113] D. Rossouw, M. Couillard, J. Vickery, E. Kumacheva, and G. Botton, "Multipolar plasmonic resonances in silver nanowire antennas imaged with a subnanometer electron probe," *Nano Letters*, vol. 11, no. 4, pp. 1499–1504, 2011.

[114] X. Zhou, A. Hörl, A. Trügler, U. Hohenester, T. B. Norris, and A. A. Herzing, "Effect of multipole excitations in electron energy-loss spectroscopy of surface plasmon modes in silver nanowires," *Journal of Applied Physics*, vol. 116, no. 22, p. 223101, 2014.

[115] F. Benz, C. Tserkezis, L. O. Herrmann, B. de Nijs, A. Sanders, D. O. Sigle, L. Pukenas, S. D. Evans, J. Aizpurua, and J. J. Baumberg, "Nanooptics of molecular-shunted plasmonic nanojunctions," *Nano Letters*, vol. 15, no. 1, pp. 669–674, 2015. PMID: 25494169.

[116] G. Boudarham, *Nanooptique avec des électrons rapides: métamatériaux, formulation modale de la EMLDOS pour des systèmes plasmoniques*. PhD thesis, Université Pierre et Marie Curie-Paris VI, 2011.

Acknowledgements

First of all I want to thank my advisor Ulrich Hohenester for guiding me through the process of creating this thesis. He had always good advice and an open door for me. I could learn a lot from him through the last years. Special thanks also goes to the other doctorial candidates and postdocs at the instute of physics, with whom I had helpful discussions and a lot of enjoyable time. I want to thank the nano-optics group of Joachim Krenn and especially the research group of Gerald Kothleitner at the FELMI Graz for exciting collaborations. Further I want to acknowledge the theoretical physics group of Stefan Rotter for a short research stay in Vienna. In addition I want to thank the group of Ted Norris for a collaboration within this thesis. On a more personal basis I want to thank Iri for her support and love.